Mixed quantum-classical modelling of non-linear optical spectra

van der Vegte, Cornelis

Mixed Quantum-Classical Modelling of Non-Linear Optical Spectra

Zernike Institute PhD series 2015-05
ISSN: 1570-1530

ISBN: 978-90-367-7706-3 (printed version)
ISBN: 978-90-367-7705-6 (electronic version)

The work described in this thesis was performed at the Zernike Institute for Advanced Materials and the Center for Theoretical Physics of the Rijksuniversiteit Groningen.

Printed by Grafimedia, University of Groningen

university of groningen

Mixed Quantum-Classical Modelling of Non-Linear Optical Spectra

Proefschrift

ter verkrijging van de graad van doctor aan de
Rijksuniversiteit Groningen
op gezag van de
Rector Magnificus prof. dr. E. Sterken
en volgens besluit van het College voor Promoties.

De openbare verdediging zal plaatsvinden op

vrijdag 17 april 2015 om 12.45 uur

door

Cornelis Petrus van der Vegte

geboren op 31 maart 1987
te Olst

Promotor
Prof. dr. J. Knoester

Copromotor
Dr. T.L.C. Jansen

Beoordelingscommissie
Prof. dr. S.J. Marrink
Prof. dr. S. Woutersen
Prof. dr. J. Köhler

Contents

Chapter 1

Introduction

1.1 Ultrafast dynamics

Dynamical processes in complex molecular systems like structural changes and energy transport through them are often challenging to resolve. Consider for example the forming and breaking of hydrogen bonds in a solvent, the electron transfer through a conjugated polymer solar cell, or the transport of an exciton in a photosynthetic system. Such processes occur on timescales as short as femtoseconds, which makes them difficult to address. A good example of intense current interest is the energy flow in pigment protein complexes of the photosystems of natural light harvesting complexes, like the Fenna-Matthews-Olson (FMO) complex [1, 2] and Light Harvesting System 2 (LH2) [3, 4]. The latter, LH2, is part of the photosystem of purple bacteria and its sole purpose is the absorption of sunlight and transferring the resulting Frenkel excitons (strongly coupled electron-hole pairs) to the reaction center, where the charge separation takes place. This initial step of photosynthesis is schematically depicted in Fig. 1.1.1. The internal quantum yield of the energy transport to the reaction center, measured in terms of ingoing and outgoing excitation quanta, is nearly 100% [5], which is rather remarkable considering the complex nature of the system. The energy transfer in LH2 is mediated by the electrostatic interactions between pigment molecules. The conformation of pigments, and the interaction between them and their local environment is optimised in such a way that energy transport is fast, so that loss processes, like fluorescence or non-radiative channels, are minimised. A better understanding of such energy transport on a molecular length scale in natural photosystems, may lead to the development of more

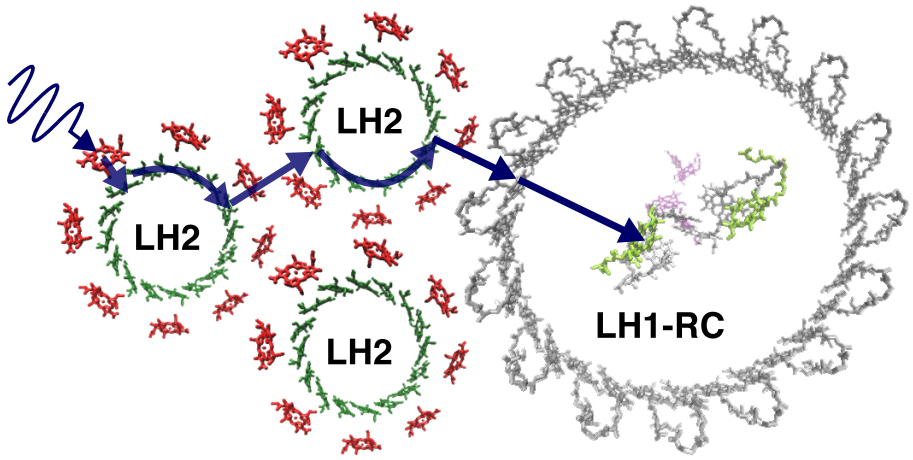

Figure 1.1.1: Schematic overview of the photosystem of purple bacteria. A photon is absorbed by a pigment in a LH2 complex. The resulting exciton is transferred through the photosystem until it reaches the Light Harvesting 1-Reaction Center complex, where the charge separation takes place.

efficient artificial energy transport systems and light harvesting complexes.

1.2 Two-dimensional spectroscopy

Through the development of ultrashort laser pulses, recent spectroscopic techniques have opened up the possibility of time resolving ultrafast dynamics down to a femtosecond timescale. By applying sequences of laser pulses, the nonlinear optical response of complex molecular systems can be obtained, which is sensitive to both structural dynamics as well as excitation dynamics that occurs during the time delays between pulses. A method that probes the third order response, where three laser pulses interact with the system, is two-dimensional spectroscopy, which has been successfully applied to studying vibrational excitations using infrared laser pulses (2DIR) [6,7] and electronic excitations using visible light (2DES) [2,8]. In Fig. 1.2.1 a schematic illustration of a two-dimensional spectroscopy setup and a two-dimensional (2D) spectrum are depicted. In the

frequency domain such an experiment comes down to pumping the system with a narrowband pulse and probing it, after a certain waiting time, with a narrowband probe pulse. By scanning over all probe frequencies for each pump frequency a 2D-spectrum for a fixed waiting time t_2 can be measured. This is achieved in a time resolved fashion by varying the times t_1 and t_3 between the laser pulses as indicated in Fig. 1.2.1, followed by a Fourier Transform. By measuring the 2D-spectra for different waiting times, detailed information on dynamical processes with a femtosecond timescale resolution is obtained.

The 2D-spectra, for instance, are determined by the dynamics of the local environment surrounding the chromophores [9–12], through their transition energies. Nuclear motions of the charged atoms in the surroundings, change the electric fields at the pigments, causing the transition frequencies and transition dipoles to fluctuate due to the Stark effect [13]. When nuclear motions occur during the waiting time, the energy of the initially excited state will change and, therefore, the probe-frequency. Consequently, the peaks in the 2D-spectra will

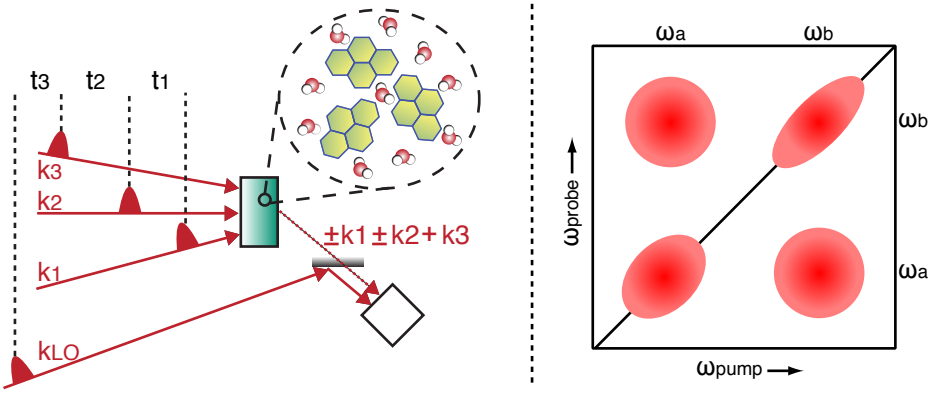

Figure 1.2.1: Left: Schematic overview of experimental setup used to measure 2D-spectra. Three laser pulses interact with the sample with time delays t_1 and t_2, after which the optical response is measured after a time delay t_3 . Right: 2D-spectra illustration for a certain waiting time t_2, with the pump frequency on the x-axis and the probe frequency on the y-axis obtained by Fourier transforming the optical response over t_1 and t_3, respectively. The presence of off-diagonal peaks indicates couplings between the energy levels ω_a and ω_b.

get a more and more circular shape, when the waiting time is increased, which is called spectral diffusion [9,14]. By studying the ellipticity of the diagonal peaks as a function of the waiting time, information on the timescales of the dynamics of the surroundings is obtained. In a similar way the 2D-spectra are sensitive to chemical exchange processes. In the case of hydrogen bond dynamics, for instance, a hydrogen bonded OH-stretch has a lower transition energy than a OH-stretching mode which is non-bonded. If during the waiting time between the pump and the probe pulse a hydrogen bond is broken or formed, a cross-peak will appear in the spectra [15]. By varying the waiting time such chemical exchange processes can be followed with a tremendous time resolution [16–18]. Moreover, the 2D-spectra are sensitive to the couplings and energy transfer between energy levels. When two states are coupled with frequencies ω_a and ω_b as illustrated in Fig. 1.2.1, for example, energy transfer between them will occur. This results in the growth of an off-diagonal cross peak in the 2D-spectra when the waiting time is increased, which allows for time resolving the energy transfer between states [2, 19–25]. This direct inferring of the couplings, furthermore, provides transient structural information, since the coupling strengths are determined by the distances between, and the relative orientations of, the optically active groups [26].

Although the 2D-spectra comprise extremely detailed information on the dynamics in complex molecular systems, they are difficult interpret. The spectra are ensemble averaged and the peaks of different states can overlap, resulting in a broad band in the 2D-spectrum, concealing the dense nature of the states. Furthermore, it is difficult to distinguish between dynamical processes like energy transport and dynamics of the environment during the waiting time, since they occur on similar timescales and both processes change the probe frequencies. In the 2D-spectra of FMO and LH2, for instance, long lived oscillations have been observed as a function of the waiting time, leading to the idea that coherent energy transport between eigenstates may be responsible for the efficient energy transport in the complex [23, 27]. Although the oscillations in the 2D-spectra may indeed result from coherent transport, it has also been proposed that they arise from underdamped vibrations in the environment [28–30]. To distinguish between such effects and reveal the nature of states, theoretical models and simulations allowing for a general description of the pigments and environment are crucially needed.

1.3 Modelling of two-dimensional spectra

The modelling of 2D-spectra of molecular systems is complicated since they usually depend on many degrees of freedom and there is a complex interplay between different interactions, which are summarised in Fig. 1.3.1. The chromophores can absorb light and are coupled to each other allowing for the excitation to transfer throughout the complex. Furthermore, the pigments are surrounded by a complex dynamical environment which cause the transition frequencies, transition dipoles and couplings to fluctuate. Such dynamical disorder influences the energy transport properties of the complex. Moreover, the pigments can be in an excited state during the waiting time between the pump and the probe pulse, which may cause a reorganisation of the environmental molecules to the local minimum of the excited state potential. Such a reorganisation can result in a Stokes shift of the transition frequencies of the chromophores. In order to interpret the 2D-spectra and understand the dynamics on ultrafast timescales it is important that theoretical models and simulations allow a general description of the complex including these interactions.

A full quantum description of all degrees of freedom is not feasible for complex molecular systems. Even in the case of a single LH2 complex, for example, the environment surrounding the pigments consists of hundreds of thousands of atoms forming the lipid bilayer, protein scaffold and solvent. Therefore, several approximative approaches, like Redfield theory [31, 32], stochastic Liouville equations [33], Pauli master equation [34] and the stochastic NISE method [30],

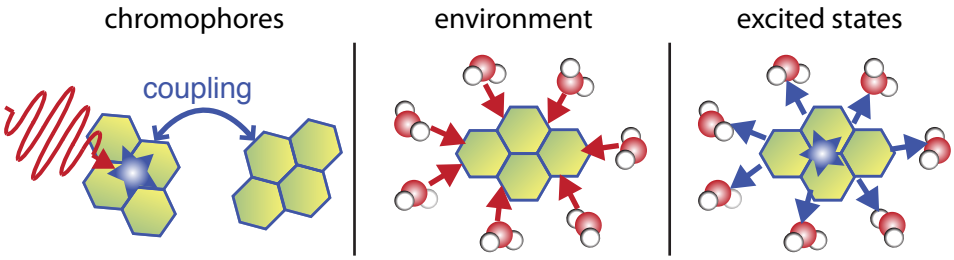

Figure 1.3.1: Schematic overview of the complex interplay of interactions determining the 2D-spectra.

have been applied for the modelling of excited state dynamics and 2D-spectra. These methods have in common that although they explicitly treat the primary degrees of freedom strongly interacting with the applied laser pulses and responsible for the energy transport, they treat the other (bath) degrees of freedom, interacting with the primary degrees of freedom, in a statistical way. These bath degrees of freedom are often described by the so called spectral density, which contains information about what frequency modes are present in the bath and how strongly they couple to the primary degrees of freedom. Phenomenological models are often used for the spectral density. A popular approach is to assume Gaussian dynamics corresponding to a harmonic bath. Although this assumption allows for an exact method, through the Hierarchical Equations of Motion approach (HEoM) [35], to calculate dynamics and 2D-spectra of an open quantum system, for a wide range of systems Gaussian distributions of the transition frequency fluctuations have been shown not to apply [36–39]. Furthermore, such a statistical description of the bath gives very limited insights concerning which atoms in the environment couple strongly to the pigments and are important for the energy transport properties in the complex. In order to describe the observed long lived oscillations in the 2D-spectra of light harvesting complexes, for example, correlations between the site energies of neighbouring pigments have been assumed [40]. Although the pigments are spatially close and thus share an environment (which determines their transition frequencies) it is unclear whether such correlations are really present. Only by a more explicit treatment of the bath degrees of freedom the presence of such correlations can be studied.

A popular approach for a more explicit treatment is to describe the environment in a fully atomistic way using classical molecular dynamics simulations. The transition frequencies, transition dipoles and couplings can then be calculated for each snapshot of the environment using Density Functional Theory [10] (DFT), semi-empirical methods [36, 41–44], or mappings that are based on the former methods [10–12]. The time-dependent Hamiltonian as a function of the classical trajectory of the atoms can then be used to calculate the 2D-spectra and excitation dynamics, which has quite successfully been applied to vibrational and electronic systems using the Numerical Integration of the Schrödinger Equation (NISE) method [45–47]. However, in this method, the influence of the quantum state on the classical degrees of freedom is neglected, so that the system and the bath are inconsistently coupled, not conserving the total energy. This infinite temperature approximation is only valid, when the energy differences between

states in the quantum system are smaller than, or comparable to, the thermal energy. The NISE method, therefore, fails to properly describe energy transport in electronic systems, where the energy differences between states are usually much larger than $k_{\mathrm{B}}T$. Not including the influence of the quantum state on the bath, furthermore, neglects effects like the Stokes shift and no information is obtained about how energy is dissipated from the quantum subsystem to the degrees of freedom surrounding the pigments.

In this thesis we develop novel mixed quantum-classical simulation methods for excited state dynamics and 2D-spectra, which are similar to the NISE method, but differ from it by including the influence of the quantum state on the classical degrees of freedom. Through this self-consistent coupling of the classical and quantum subsystems, the total energy is conserved, overcoming the infinite temperature approximation made in NISE and including effects like the Stokes shift. The environment surrounding the pigments can be described using classical molecular dynamics simulations, allowing for the application to a wide range of problems including non-Gaussian dynamics, non-Condon effects [48] (fluctuating transition dipoles) and underdamped vibrations. This explicit treatment of the bath degrees of freedom, furthermore, provides detailed information on how the energy is dissipated and which degrees of freedom couple strongly to the quantum system.

1.4 Outline

In chapter 2, we describe two novel simulation methods of 2D-spectra. These methods include the influence of the quantum state on the classical degrees of freedom based on a mean field theory (Ehrenfest method) [49,50] and the fewest switching surface hopping method [51,52], which previously have been used for mixed quantum-classical simulations of excited state dynamics for pigments in a complex environment, but so far have not been applied to 2D-spectra. We apply the methods to model systems, where the bath degrees of freedom are described by a collective mode also known as the Brownian oscillator model [53]. We assume harmonic potentials so that we can benchmark the NISE method and two novel methods including the feedback with the exact result provided by the HEoM approach. We show that the surface hopping method reproduces the exact result best, since it leads to a correct thermalisation of the quantum subsystem, which is reflected in the energy transfer between states, directly observed in the

cross-peak growth in the 2D-spectra.

In chapter 3 we combine the surface hopping method with fully atomistic molecular dynamics simulations to calculate 2D-spectra of OH-stretching vibrations in synthetic quasi one-dimensional hydrogen bonded chains and compare with experiments. We show that the stereochemistry of the synthetic chains determine their hydrogen bond dynamics, which is reflected in slopes of the peaks in the 2D-spectra. Furthermore, we show that the hydrogen bonding structure determines whether an initial excitation remains in that state or rapidly distributes over the network, which explains the observed pump-frequency dependence of the vibrational lifetime for the compounds with different stereo-chemistry.

In chapter 4 we study energy transport in LH2 and show that the nature of the states determining the spectra, allows for a fast downhill energy transport. We describe the environment surrounding the pigments using fully atomistic molecular dynamics simulations including the protein scaffold, lipid membrane and solvent and show how they influence the transition frequencies of the pigments. Furthermore, we show that correlations between the transition frequencies of neighbouring pigments are negligible for LH2, and cannot be used to explain the observed oscillations in the 2D-spectra.

Chapter 2

Quantum-classical simulations of two-dimensional spectra

In this chapter we present two novel mixed quantum-classical simulation approaches to calculate two-dimensional spectra of coupled two-level electronic model systems. We include the change in potential energy of the classical system due to transitions in the quantum system using the Ehrenfest method and surface hopping method, respectively. We study how this feedback of the quantum system on the classical system influences the shape of two-dimensional spectra. We show that the feedback leads to the expected Stokes shift of the energy levels in the quantum system. This subsequently leads to changes in the population transfer between quantum sites, which in turn influence the intensities of the peaks in two-dimensional spectra. The obtained spectra are compared with spectra calculated using the Hierarchical Equations of Motion method which is exact. For the Ehrenfest method the spectra match perfectly for short waiting times, but clear differences are found for longer waiting times, which is attributed to a violation of detailed balance between the quantum states in this method. The Surface Hopping method, on the contrary, accounts for a correct thermal equilibration of the quantum populations and the spectra are found to agree nicely with the exact result for short and long waiting times.

This chapter is based on C. P. van der Vegte, A. G. Dijkstra, J. Knoester, T. L. C. Jansen J. Phys. Chem. A, **117**, 5970 (2013) and R. Tempelaar, C. P. van der Vegte, J. Knoester and T. L. C. Jansen J. Chem. Phys. **138**, 164106 (2013)

2.1 Introduction

Two-dimensional spectroscopy has proven to be a powerful tool for investigating and characterizing chemical and physical processes in molecular systems down to the femtosecond timescale [2,6,7,46,54]. It has been applied successfully to processes like proton transfer [55–57] and hydrogen bond breaking [37,58]. The cross peaks in two-dimensional spectra are determined by the couplings in the molecular system and are sensitive to population transfer between different eigenstates. This allows one to follow vibrational [19–22] and electronic [2,23–25] population transfer in complex molecular systems. Measured two-dimensional spectra are, however, difficult to interpret. Therefore, theoretical models and simulations are crucial for a better understanding of the measured spectra. For example, in the first electronic two-dimensional spectra measured for light harvesting complexes [2] oscillations were observed. This led to the idea that coherent transport may play a role in biological systems. The observed oscillations may indeed arise from coherent population transfer, but underdamped vibrations in the environment and the coherent nature of the excitations may lead to oscillations as well. Theoretical models and simulations are needed to disentangle these effects. Here we will propose two new simulation methods that allows a general treatment of most of the physical phenomena that determine the spectral shapes.

Two-dimensional spectroscopy is typically performed in solution. The chromophores are influenced by fluctuations of the solvent environment and vice versa. A full quantum description of such systems is not feasible because of the large number of degrees of freedom involved. Therefore, several approximate schemes have been applied. If the temperature is sufficiently high, a completely classical treatment may be valid [59]; However, at room temperature this neither applies to vibrational nor to electronic spectroscopy. Alternatively, one can treat the environment classically using molecular dynamics simulations and use a quantum description of the chromophores. For this to be valid the thermal energy (k_BT) should be high compared to the energy difference between states of the degrees of freedom treated classically. This approach has been applied quite successfully in the so-called Numerical Integration of the Schrödinger equation (NISE) implementation [45,47,60]. When a chromophore is excited, the charge density of the molecule changes. This subsequently changes the potential the environmental molecules feel. This feedback of the chromophores which are treated quantum mechanically on the classical environment is not included in the NISE-

method, since it assumes a ground-state classical path approximation. Giving up an explicit description of the bath degrees of freedom for a stochastic description, one can apply Redfield theory [31] to calculate the two-dimensional spectra [32]. While this is a perturbative approximation it is valid at low temperatures. Similarly the Pauli Master equation can be used [34]. As both these methods rely on perturbation theory they may fail if the quantum levels are degenerate or close to degenerate. Furthermore, these perturbative approaches treat the environment as a stochastic bath and they assume Gaussian dynamics. This approximation has been found not to apply for a light harvesting system at room temperature [36], and is known to affect the two-dimensional spectral lineshapes [37–39]. Likewise, nonperturbative Stochastic Liouville Equation type approaches rely on a correlation function based description of the bath as well [33]. A quite general mixed quantum-classical Liouville approach has been implemented for single chromophores [61–64]. Finally, the hierarchical equations of motion (HEoM) provide a way to calculate the exact two-dimensional spectra, but so far this method only has been implemented for an environment with Gaussian motion [65–67]. Furthermore this method is rather expensive computationally. The method does, however, provide an important benchmark for other methods.

Other ways exist to treat the dynamics of coupled chromophores in complex environments. These have thus far not been applied to simulate two-dimensional spectra. Among such methods are the Lindblad equations [68], the scaled coupling method [69], the fewest-switches surface hopping method [51], and Ehrenfest dynamics [49,50]. In this chapter we will develop the machinery to calculate two-dimensional spectra using the latter two methods. These methods for simulating two-dimensional spectra are very similar to the NISE method but differ from it by including the feedback of the quantum system on the classical environment, in their own respective ways. Like NISE, these approaches should be applicable to a wide range of situations including problems with underdamped vibrations in the environment, non-Gaussian dynamics [36,38], and non-Condon effects [48], but, in contrast to NISE, include the Stokes shift.

We will study the influence of the quantum force on the environment resulting from transitions in the quantum system on the shape of two-dimensional spectra, using the Ehrenfest method and surface hopping method mentioned above. The methods for calculating two-dimensional electronic spectra including the feedback of the quantum system will be explained in Section 2.2. If the feedback term is neglected, these methods reduce to the NISE method [45, 47].

In Section 2.3 the simulated two-dimensional spectra excluding and including the feedback using the Ehrenfest method and surface hopping method will be compared. As a benchmark we compare the obtained spectra with spectra calculated using the HEoM. This restricts us to using Gaussian motion, which can be described with the HEoM. For a single two-level system the Ehrenfest method and surface hopping method are identical and we show that the feedback results in a Stokes shift of the chromophore's transition energy. The methods give excellent correspondence to the HEoM method for the single chromophore. For two coupled two-level systems we show that including the feedback alters the peak positions and the growth of the cross peaks when the time between the pump- and probe pulse, also denoted the waiting time, is increased. The energy difference between the one-quantum eigenstates is chosen larger than the thermal energy leading to very different two-dimensional spectra for the three mixed quantum-classical methods (NISE, Ehrenfest, surface hopping). We show that the spectra differ because the populations of the eigenstates in equilibrium for the three mixed quantum-classical method are very different, which is directly related to the growth of the cross-peaks. The NISE method is an infinite temperature approximation leading to equal probabilities for the occupation of each state in equilibrium, which is invalid for the dimer considered since the energy differences are much larger than the thermal energy. The Ehrenfest method shows improved behavior compared to NISE, but also does not lead to a Boltzmann distribution within the quantum system due to the mean field approach for including the quantum feedback [70]. We show that the surface hopping method does result in a Boltzmann distribution of the quantum system and, therefore, is able to reproduce the HEoM result well for the dimer for short and long waiting times. Finally, we will present our conclusions in Section 2.4.

2.2 Method

2.2.1 Mixed quantum-classical equations of motion

We treat the part of the sample that directly interacts with the applied laser fields quantum mechanically (the electronic quantum system) and the part of the sample not interacting with the light, but strongly interacting with the quantum system classically (the classical system). All other degrees of freedom are treated as a weakly interacting stochastic bath. The total Hamiltonian of the system

can then be written as

$$H(t) = H_Q(t) + H_C(t) + H_{Q-C}(t) + H_{\text{light}}(t), \tag{2.2.1}$$

where H_Q and H_C denote the Hamiltonians of the quantum- and classical system, respectively, H_{Q-C} describes the interaction between the two subsystems, and H_{light} describes the interaction between the quantum subsystem and the applied laser fields. The Frenkel exciton Hamiltonian will be used to describe the electronic excitations in the quantum system

$$H_Q(t) = hc \left(\sum_i \omega_{0i} B_i^\dagger B_i + \sum_{i \neq j} J_{ij} B_i^\dagger B_j) \right). \tag{2.2.2}$$

Here, $B_i^\dagger$ and B_i are the bosonic creation and annihilation operators, respectively, for the excitation of site i with central frequency ω_{0i}. J_{ij} denotes the coupling strength between the quantum sites i and j. The formalism presented here can be directly applied to vibrational systems by including a third level on each chromophore (site) and an anharmonicity term [6]. Note that the Frenkel exciton Hamiltonian allows for population transfer within excitation manifolds, but neglects relaxation between them. The interaction of the applied laser field $E(t)$ with the quantum sites, which have transition dipoles μ_i, is given by

$$H_{\text{light}} = hc \sum_i \vec{\mu}_i \cdot \vec{E}(t)(B_i^\dagger + B_i). \tag{2.2.3}$$

For simplicity we assume throughout this chapter that all transition dipole vectors are equal, and parallel to the external electric field. Furthermore, we assume that the laser pulses have an infinitely short (delta peak) duration.

The environment surrounding the quantum system is treated in a classical way using the Brownian oscillator model [53]. A classical treatment of the bath is valid when the thermal energy is large compared to the energy difference between the states of the degrees of freedom treated classically and for an overdamped mode the inverse correlation time needs to be small compared to the thermal energy. If important modes are present with higher frequencies they should be included directly in the quantum system. In this model collective bath coordinates are used to describe local vibrations of the environment molecules. A single Brownian oscillator with mass M_i and coordinate x_i is coupled to quantum

site i to describe local fluctuations of the environment. We assume that each environmental mode feels a harmonic potential so that the Hamiltonian for the classical system is given by

$$H_C(t) = \sum_i \frac{1}{2} k_i x_i^2(t) + \sum_i \frac{1}{2} M_i \dot{x}_i^2(t), \tag{2.2.4}$$

where the summations are over all Brownian oscillators. Anharmonic terms can be included without significant additional computational cost. We do not include anharmonic terms within this chapter, however, because we will compare the calculated spectra with the HEoM method, which is limited to harmonic modes (Gaussian motion).

The vibrations of the environment molecules influence the quantum system and, vice versa, the potential of the environment depends on the state of the quantum system. The coupling strength J_{ij} and the transition dipole moments μ_i are assumed to be independent of the environment, and will be treated as constants. The quantum-classical interaction Hamiltonian is defined as

$$H_{Q-C}(t) = \sum_i hcD_i x_i(t) B_i^\dagger B_i, \tag{2.2.5}$$

where D_i denotes the strength of the coupling. From Eq. 2.2.5 it follows that the frequency of the quantum excitations ω_i depends linearly on the classical coordinate coupled to the excitation

$$\omega_i = \omega_{i0} + D_i x_i. \tag{2.2.6}$$

This is not a fundamental limitation of the Ehrenfest nor surface hopping method but a limitation of the HEoM. A nonlinear classical coordinate dependence will be straightforward to implement. The Brownian oscillators are coupled to a stochastic heat bath with temperature T and the strength of the coupling is determined by the friction constant γ. The quantum system, classical system, the heat bath and all the interactions are schematically shown in Fig. 2.2.1.

The time evolution of the quantum system is described by the time dependent Schrödinger equation

$$i\hbar \frac{d\Phi(t)}{dt} = (H_Q + H_{Q-C}(t))\Phi(t), \tag{2.2.7}$$

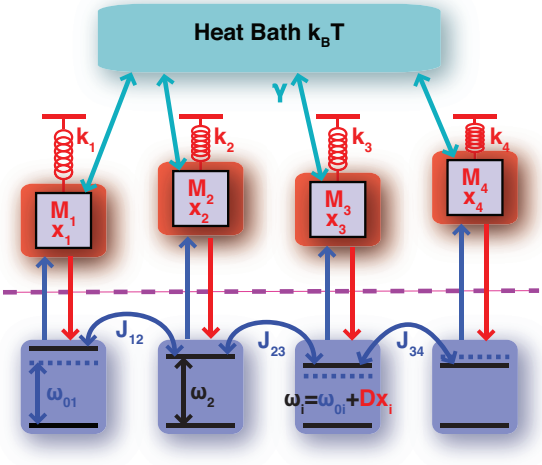

Figure 2.2.1: Schematic illustration of the model system. Each quantum site i (blue boxes) is coupled to a single Brownian oscillator (red boxes) with mass M_i and coordinate x_i which is driven by a heat bath with temperature T. The transition energies at the quantum sites are linearly dependent on the classical coordinates.

where $\Psi(t)$ is the wave function describing the quantum state. The equation of motion for the Brownian oscillator i in contact with the heat bath is given by the Langevin equation

$$M_i\ddot{x}_i(t) \quad = \quad -k_i x_i(t) - F_i^q(t,\Phi) - \gamma M_i \dot{x}_i(t) + F_{\text{fluc}}(t). \tag{2.2.8}$$

Here the first term follows from the classical system Hamiltonian. The second term denotes the force of the quantum system on the Brownian oscillator, to which we come back later in this section. The third term and fourth term describe the interaction of the Brownian oscillator to the heat bath. The third term describes the friction and F_{fluc} is a Gaussian stochastic random fluctuating force which is related to the friction constant and temperature in the following way [53]

$$< F_{\text{fluc}}(t) F_{\text{fluc}}(0) >= \begin{cases} \frac{2M\gamma k_B T}{\Delta t} & \text{for } t = 0 \\ 0 & \text{for } t \neq 0 \end{cases} \tag{2.2.9}$$

Here Δt denotes the time interval used for the numerical integration of Eq. 2.2.8.

2.2.2 Quantum feedback

When the quantum system is excited, the potential of the environment surrounding the chromophores will be different from that of the ground state. Therefore, the equation of motion for the classical atoms (Eq. 2.2.8) depends on the quantum state Ψ. The difficulty that arises here, is that one is dealing with quantum operators in a classical equation of motion. The quantum state can be in a superposition of multiple states which all have a different contribution to the potential energy surface of the classical degrees of freedom.

One way of dealing with this problem is the Ehrenfest method, where the force is replaced by its expectation value [71]

$$F_i^q = -\langle \Phi | \nabla_{x_i} H_{\text{Q-C}}(t) | \Phi \rangle, \tag{2.2.10}$$

where Φ denotes the wavefunction of the quantum system described by Eq. 2.2.7. For the quantum-classical interaction in Eq. 2.2.5 the quantum feedback force on the classical brownian oscillator i within the Ehrenfest approximation reduces to

$$F_i^q = -hcD_i d_i(t)^* d_i(t), \tag{2.2.11}$$

and thus linearly depends on the probability that the quantum site i ($d_i^*(t)d_i(t)$) is excited. This method conserves the energy of the total quantum-classical system during propagation. It does, however, not lead to the correct thermalization in the quantum subsystem, because the energy levels in the quantum system are no longer quantized due to the mean field theory [70].

A method that can overcome this deficiency is the surface hopping method [52, 72]. In this method the quantum system is described by two wavefunctions: The "normal" primary wavefunction Φ, which describes the state of the quantum system and which is propagated by Eq. 2.2.7, and the auxiliary wavefunction Ψ, which describes the state of the quantum system the environmental molecules feel. In the surface hopping method the auxiliary wavefunction can in principle be chosen as any basis vector of an orthogonal basis of the quantum Hamiltonian. In our case we choose the adiabatic basis so that the auxiliary wavefunction corresponds to an instantaneous eigenstate Ψ_k of the Hamiltonian

$(H_Q + H_{Q-C})$. The quantum force a classical degree of freedom i feels, when the auxiliary wavefunction at a certain time is in an eigenstate k, is then given by

$$F_i^q = -\langle \Psi_k | \nabla_{x_i} H_{\text{Q-C}}(t) | \Psi_k \rangle. \tag{2.2.12}$$

Using this expression for the quantum feedback in Eq. 2.2.8, the quantum-classical system are coupled in a self-consistent way and upon propagation the total energy is conserved (with the quantum subsystem residing in the eigenstate Ψ_k). In the surface hopping method the auxiliary wavefunction can make a stochastic "hop" to a different eigenstate of the Hamiltonian at every timestep along the trajectory. For the Hamiltonian in Eq. 2.2.2 hopping is only allowed between eigenstates within the same excitation manifold since there is no coupling between states in different excitation manifolds. When a hop takes place from an initial state k to a final state l the total energy of the quantum-classical system should be conserved. The energy difference between the eigenstates, therefore, is either dumped into or withdrawn from the kinetic energy of the classical degrees of freedom. In the remainder of this subsection the stochastic process for determining whether a hop takes place and the velocity adjustment of the classical degrees of freedom is described.

The primary wavefunction can be written as a linear combination of eigenvectors of the Hamiltonian

$$\Phi(t) = \sum_k c_k(t) \Psi_k(t). \tag{2.2.13}$$

The coefficients and eigenvectors are both time-dependent since the quantum Hamiltonian changes over time. Plugging in this expansion in Eq. 2.2.7 and rewriting leads to the following equation for the coefficients

$$\frac{dc_k(t)}{dt} = -\frac{i}{\hbar} \epsilon_k c_k(t) - \sum_l c_l \dot{\vec{x}} \cdot \vec{d}_{kl}, \tag{2.2.14}$$

where ϵ_k is the energy of the eigenstate k, $\dot{\vec{x}} = (\dot{x_1}, \dot{x_2}, ...)$ is a vector representing the velocities of the classical degrees of freedom and $\vec{d}_{kl}$ is the nonadiabatic coupling vector

$$\mathbf{d}_{kl} = \langle \Psi_k | \nabla_{\vec{x}} | \Psi_l \rangle. \tag{2.2.15}$$

According to Tully's fewest switches surface hopping algorithm [52] the probability for the auxiliary wavefunction to hop from the present eigenstate k to another eigenstate l during a timestep is given by

$$P_{k\to l} = -2\dot{\vec{x}} \cdot \vec{d}_{lk} \mathrm{Re}\left(\frac{c_l}{c_k}\right) \Delta t. \tag{2.2.16}$$

At every timestep, the probabilities for hopping to the different eigenstates are calculated and a random number σ is generated between 0 and 1. A hop is made from the eigenstate k to l if the following condition is satisfied

$$\sum_{l'\leq l-1} P_{k\to l'} < \sigma < \sum_{l'\leq l} P_{k\to l'}. \tag{2.2.17}$$

In this way only a single random number has to be generated each timestep. Most of the time the auxiliary wavefunction will remain in its state, since the probabilities for hopping are often much smaller than unity. When a hop takes place from an initial state k to a final state l the total energy of the quantum-classical system should be conserved. When the final state is lower in energy, the energy difference will be deposited as kinetic energy in the classical subsystem. Vice versa, when the final state is higher in energy the energy difference is withdrawn from the kinetic energy of the classical system. The adjustments of the velocities of the classical degrees of freedom are done in the direction of the non-adiabatic coupling vector

$$\dot{\vec{x}}_i^{\mathrm{new}} = \dot{\vec{x}}_i^{\mathrm{old}} - \gamma_{lk}\vec{d}_{lk}/m_i, \tag{2.2.18}$$

where γ_{lk} is a constant that makes sure the total energy of the quantum-classical system is conserved when the hop takes place. The classical degrees of freedom that couple stronger to the quantum subsystem (stronger non-adiabatic coupling) get bigger shifts in their velocity. A hop to an eigenstate higher in energy is not executed, when there is not enough kinetic energy available (along the direction of the non-adiabatic coupling vector), to maintain energy conservation.

2.2.3 (Non-)linear optical response

The time-dependent Schrödinger equation (Eq. 2.2.7) and the equation of motion for the classical system (Eq. 2.2.8) form a set of coupled equations. The

time-dependent Schrödinger equation cannot be solved directly for the time-dependent Hamiltonian in Eq. 2.2.7. We therefore assume that the Hamiltonian $H_{Q-C}(t)$ is constant during a short time interval Δt, so that the time evolution operator during this time interval is given by the solution of the time-independent Schrödinger equation

$$\mathbf{U}(t+\Delta t, t) = e^{-\frac{i}{\hbar}(H_Q + H_{Q-C}(t))\Delta t}. \tag{2.2.19}$$

The new quantum state of the system $\Phi(t+\Delta t)$ can then be obtained by multiplying the wave function $\Phi(t)$ with the time evolution operator. The new coordinates of the Brownian oscillator $x_i(t+\Delta t)$ and $\dot{x}_i(t+\Delta t)$ are calculated by numerical integration with a modified Verlet method of Eq. 2.2.8

$$\begin{aligned}
\dot{x}_i\left(t+\frac{\Delta t}{2}\right) &= \dot{x}_i(t) + \frac{1}{2}\ddot{x}_i(t)\Delta t \\
x_i(t+\Delta t) &= x_i(t) + \dot{x}_i\left(t+\frac{\Delta t}{2}\right)\Delta t \\
\ddot{x}_i(t+\Delta t) &= -\frac{k_i}{M_i}x_i(t+\Delta t) - hcD_i c_i^*(t)c_i(t) - \gamma\dot{x}_i\left(t+\frac{\Delta t}{2}\right) + \frac{F_{fluc}(t)}{M_i} \\
\dot{x}_i(t+\Delta t) &= \dot{x}_i\left(t+\frac{\Delta t}{2}\right) + \frac{1}{2}\ddot{x}_i(t+\Delta t)\Delta t.
\end{aligned} \tag{2.2.20}$$

From the new coordinates the Hamiltonian $H_{Q-C}(t+\Delta t)$ is known and the propagation for the next time step is performed resulting in an iterative procedure. The time evolution operator for longer time differences $\mathbf{U}(\tau_i, \tau_j)$ is thus obtained by the time ordered products of the time evolution operators for short intervals Δt. This is identical to the way this is solved in the NISE-method [45, 46]. In the NISE-method the propagation of the classical system however does not depend on the state of the quantum system, and can therefore be done prior to propagating the quantum system. The coupled propagation of the quantum and classical systems is schematically depicted in Fig. 2.2.2. When the coupling to the heat bath is switched off ($\gamma = 0$), the total energy of the system (quantum plus classical) for calculations including the feedback using this scheme is conserved. For the parameters used in Table 2.3.2 (with $\gamma = 0$), however, the energy increases by 1.2 % after a trajectory of 100 ps. This is due to the accumulation of numerical errors during the numerical integration where a finite time step is used. All spectral calculations required less than 15 ps of continuous propagation, implying that this numerical error does not affect the spectra presented

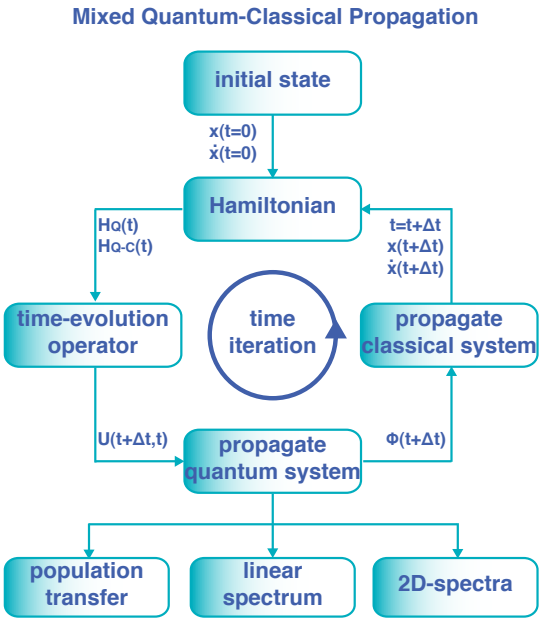

Figure 2.2.2: Schematic diagram for the propagation of the state of the quantum system and coordinates of the classical system for the Ehrenfest and surface hopping method from which the population transfer, linear spectrum, and 2D-spectra can be calculated. Each calculation starts with initial conditions for the classical coordinates $x(t=0)$, $\dot{x}(t=0)$, which are extracted from a trajectory, in which the quantum system is in the ground state, separated by multiple correlation times.

here. Using the scheme in Fig. 2.2.2 the population transfer, linear spectrum and two-dimensional spectra can be calculated as will be explained below.

The population transfer between an initial eigenstate i and a final eigenstate f is calculated by

$$P_{fi}(t) = \langle |\langle \Psi_f(t)|\mathbf{U}(t,0)|\Psi_i(0)\rangle|^2 \rangle_E. \tag{2.2.21}$$

Here $\langle ... \rangle_E$ denotes the ensemble average, which is calculated by summing results from N_{samples} different initial starting points for the classical system which are extracted from a trajectory during which the quantum-system is in the ground

state (no feedback) separated by 100 ps. The inner brackets denote the usual Dirac notation for quantum mechanics. The population transfer between the two eigenstates for the surface hopping method is defined as the probability that the auxiliary wavefunction is in the state Ψ_f as a function of propagation time, upon initial excitation of the primary and auxiliary wavefunction equal to Ψ_i.

For the linear absorption spectrum the system is excited by interacting with a laser pulse at a time τ_1, after which a signal is emitted by the system at a time τ_2. The absorption spectrum is calculated by taking the imaginary part of the Fourier transform, over the time between the laser pulse and the signal $t_1 = \tau_2 - \tau_1$, of the two-point correlation function of the transition dipoles

$$S_A(\omega) = \mathrm{Im}\left[\int_0^\infty \frac{i}{\hbar}\langle \mu^{01}(\tau_2)\mathbf{U}^{11}(\tau_2,\tau_1)\mu^{10}(\tau_1)\rangle_E e^{-i\omega t_1} dt_1\right]. \qquad (2.2.22)$$

Here μ^{10} denotes the transition dipole moment between the initial ground state (denoted 0) and the final excited state (denoted 1). The superscript in the propagator (11) denotes the propagation when there is a single excitation in the quantum system (single excited state). A lifetime T_1 of the excited state can be included in an *ad hoc* way by multiplying the response function by

$$\Gamma_{LA} = e^{-\frac{t_1}{2T_1}}. \qquad (2.2.23)$$

Our main focus is to simulate two-dimensional electronic spectra described by the third-order response function. In this experiment, three laser pulses are applied at times τ_1, τ_2, and τ_3 and the signal is measured at a time τ_4 [2,7,46,53]. Using impulsive pulses and applying the Rotating Wave Approximation [7] the signal for the third-order response function has six contributions. These can be represented by the double-sided Feynman diagrams depicted in Fig. 2.2.3 [53]. The six contributions are the rephasing and non-rephasing parts of the ground state bleach (GB), the stimulated emission (SE) and the excited state absorption (EA). The first laser pulse brings the quantum system in a coherence between a single excited state and the ground state (01 (rephasing) or 10 (non-rephasing)) for all diagrams. For the GB-diagram the interaction with the second laser pulse brings the system back in the ground state. The interaction with the third laser pulse brings the system in a coherence between the single excited state and the ground state (10). At a time τ_4 the system relaxes back to the ground state by emitting the signal. The SE-diagram differs from the GB-diagram only during the waiting time t_2, where the system is in a single excited state or a coherence

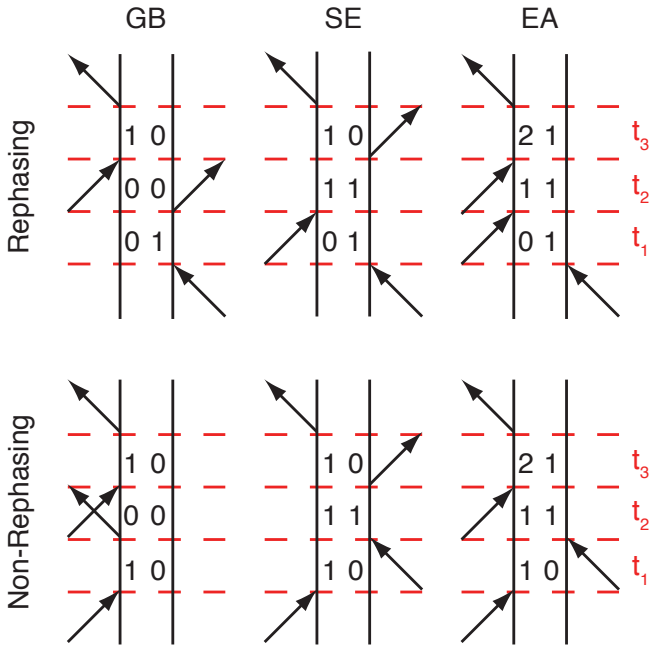

Figure 2.2.3: Double-sided Feynmann diagrams that contribute to the third-order response. Three laser fields are applied with time delays $t_1 = \tau_2 - \tau_1$ and $t_2 = \tau_3 - \tau_2$. The signal is emitted by the system a time $t_3 = \tau_4 - \tau_3$ after the third laser pulse. The numbers 0, 1, and 2 denote the ground state, single excited states, and double excited states, respectively.

between two single-excited states instead of the ground state. The excited state absorption diagrams are the same as the stimulated emission diagrams until the third laser pulse. The third laser pulse brings the system in a coherence between a double excited state (a state where two sites are excited) and a single excited state (21). The responses of all six diagrams can be obtained by calculating the

following ensemble averages

$$\begin{aligned}
S^R_{GB}(t_1,t_2,t_3) &= -\left(\frac{i}{\hbar}\right)^3 \langle\langle 0|\mu^{01}(\tau_1)\mathbf{U}^{11}(\tau_1,\tau_2)\mu^{10}(\tau_2) \\
&\qquad \mu^{01}(\tau_4)\mathbf{U}^{11}(\tau_4,\tau_3)\mu^{10}(\tau_3)|0\rangle\rangle_E \\
S^R_{SE}(t_1,t_2,t_3) &= -\left(\frac{i}{\hbar}\right)^3 \langle\langle 0|\mu^{01}(\tau_1)\mathbf{U}^{11}(\tau_1,\tau_3)\mu^{10}(\tau_3) \\
&\qquad \mu^{01}(\tau_4)\mathbf{U}^{11}(\tau_4,\tau_2)\mu^{10}(\tau_2)|0\rangle\rangle_E \\
S^R_{EA}(t_1,t_2,t_3) &= \left(\frac{i}{\hbar}\right)^3 \langle\langle 0|\mu^{01}(\tau_1)\mathbf{U}^{11}(\tau_1,\tau_4)\mu^{12}(\tau_4)\mathbf{U}^{22}(\tau_4,\tau_3) \\
&\qquad \mu^{21}(\tau_3)\mathbf{U}^{11}(\tau_3,\tau_2)\mu^{10}(\tau_2)|0\rangle\rangle_E \\
S^{NR}_{GB}(t_1,t_2,t_3) &= -\left(\frac{i}{\hbar}\right)^3 \langle\langle 0|\mu^{01}(\tau_4)\mathbf{U}^{11}(\tau_4,\tau_3)\mu^{10}(\tau_3) \\
&\qquad \mu^{01}(\tau_2)\mathbf{U}^{11}(\tau_2,\tau_1)\mu^{10}(\tau_1)|0\rangle\rangle_E \\
S^{NR}_{SE}(t_1,t_2,t_3) &= -\left(\frac{i}{\hbar}\right)^3 \langle\langle 0|\mu^{01}(\tau_2)\mathbf{U}^{11}(\tau_2,\tau_3)\mu^{10}(\tau_3) \\
&\qquad \mu^{01}(\tau_4)\mathbf{U}^{11}(\tau_4,\tau_1)\mu^{10}(\tau_1)|0\rangle\rangle_E \\
S^{NR}_{EA}(t_1,t_2,t_3) &= \left(\frac{i}{\hbar}\right)^3 \langle\langle 0|\mu^{01}(\tau_2)\mathbf{U}^{11}(\tau_2,\tau_4)\mu^{12}(\tau_4)\mathbf{U}^{22}(\tau_4,\tau_3) \\
&\qquad \mu^{21}(\tau_3)\mathbf{U}^{11}(\tau_3,\tau_1)\mu^{10}(\tau_1)|0\rangle\rangle_E.
\end{aligned} \tag{2.2.24}$$

Here the time evolution operators have superscript indices denoting the propagation of a single excited state (11) or a double excited state (22). The propagator of the ground state is given by unity and is omitted in the expressions above. The coupled time evolution of the quantum and classical systems is calculated following the scheme depicted in Fig. 2.2.2. The trajectory of the classical degrees of freedom depends on the state of the quantum system and, therefore, will be different for the separate Feynman diagrams.

For the Ehrenfest method the quantum force on the Brownian oscillator i depends on the probability that the quantum site i is excited (Eq. 2.2.8). When the system is in a coherence between two states, the feedback of the quantum system on the classical system is taken into account separately for the ket- and bra-side which are described by different wave functions $\Phi^K(t)$ and

$\Phi^B(t)$ respectively. The Langevin equation for the Brownian oscillator i then reads

$$\begin{aligned} M_i\ddot{x}_i(t) &= -kx_i(t) - \frac{hcD_i}{2}\left(d^*_{Ki}(t)d_{Ki}(t) + d^*_{Bi}(t)d_{Bi}(t)\right) \\ &\quad -\gamma M_i\dot{x}_i(t) + F_{fluc}(t), \end{aligned} \tag{2.2.25}$$

thus assuming a mean classical path approximation for coherences.

For the surface hopping method the quantum feedback on the classical degrees of freedom is determined by the auxiliary wavefunction. The auxiliary wavefunction in our case is always in an eigenstate of the quantum Hamiltonian and the quantum feedback is only defined for a quantum population. During the times t_1 and t_3 the quantum system is in a coherence between excitation manifolds, however, and it is unclear how to calculate the quantum feedback using the surface hopping method. Recently a surface hopping approach was developed for the propagation of such quantum coherences and applied for the calculation of linear spectra [73]. We decide, however, to neglect the quantum feedback during the coherence times t_1 and t_3, because according to our findings the effects of the feedback on the 2D-spectra during these times are small. During the waiting time t_2 of the ground state bleach diagrams the quantum system is in the ground state and there is no quantum feedback force on the classical trajectory. For the stimulated emission and excited state absorption the quantum system is either in a population of a single excited state, or in a coherence between two single excited states during the waiting time. The response functions of these diagrams are split up in N +1 different parts, where N is the number of eigenstates in the first excitation manifold. For the part of the response functions where the quantum system is in a population of an eigenstate during t_2, the population dynamics is described by the auxiliary wavefunction, and the quantum feedback is included using the surface hopping method as described in Sec. 2.2.2. This leads to N contributions, which all have different classical trajectories due to the quantum feedback. The quantum feedback is neglected for the part of the response function where the quantum system is in a coherence between two single excited states during the waiting time. The different possible coherences can be propagated at the same time, since they are calculated with the same classical trajectory.

In the absence of relaxation between the excitation manifolds in the present Hamiltonian, the lifetime T_1 of the excited states can be taken in to account in an *ad hoc* way by multiplying the response functions in Eq. 2.2.24 by the

following factor

$$\Gamma(t_3, t_2, t_1) = e^{-(t_1+2t_2+t_3)/2T_1}. \tag{2.2.26}$$

The signals in the frequency domain (for a fixed waiting time t_2) resulting from the rephasing and non-rephasing diagrams are obtained by Fourier transforming over the times t_1 and t_3

$$\begin{aligned} S^R(\omega_1, t_2, \omega_3) &= \int_0^{t_1^{max}} \int_0^{t_3^{max}} (S^R_{GB}(t_1, t_2, t_3) + S^R_{SE}(t_1, t_2, t_3) \\ &\quad + S^R_{EA}(t_1, t_2, t_3)) e^{-i(\omega_1 t_1 - \omega_3 t_3)} dt_1 dt_3 \\ S^{NR}(\omega_1, t_2, \omega_3) &= \int_0^{t_1^{max}} \int_0^{t_3^{max}} (S^{NR}_{GB}(t_1, t_2, t_3) + S^{NR}_{SE}(t_1, t_2, t_3) \\ &\quad + S^{NR}_{EA}(t_1, t_2, t_3)) e^{-i(\omega_1 t_1 - \omega_3 t_3)} dt_1 dt_3. \end{aligned} \tag{2.2.27}$$

In general the response function should be integrated over times t_1 and t_3 from zero to infinity. The response function, however, vanishes at finite t_1 and t_3 times, either due to dephasing or the finite lifetime of the excitation, and therefore, in practice finite times t_1^{max} and t_3^{max} can be used. The absorptive spectrum is obtained by adding the imaginary parts of the responses resulting from the rephasing and non-rephasing diagrams [74].

2.2.4 Hierarchical Equations of Motion

The HEoM implementation is an exact method to calculate the dynamics of an open quantum system and observables such as the two-dimensional spectrum [35]. A derivation and extensive explanation of the method can be found in Refs. [35, 67, 75]. Here we only give a brief explanation of the method and an overview of the approximations we make.

The Hamiltonian we use for the HEoM is very similar to Eq. 2.2.1 [75]. The quantum system consisting of coupled chromophores is again described by the Frenkel exciton Hamiltonian. A single Brownian oscillator (phonon mode) is coupled to each chromophore which in contrary to the previous section is described quantum mechanically as well. The time evolution of the density matrix in the HEoM approach is described by a set of infinitely many coupled differential equations. The first of these differential equations describes the time evolution

of the reduced density operator $\sigma^{(0,0)}(t)$ which is the trace of the total density matrix over all environmental degrees of freedom. The reduced density operator contains all the information of the quantum system. The number of superscript indices is equal to the number of chromophores in the quantum system so that in this case we treat a dimer. The time evolution of the reduced density operator depends on auxiliary operators, for which one or all of these indices are larger than zero, which account for the state of the environment as well as correlations between the system and the environment. The reduced density operator only couples to auxiliary operators for which one of the indices is increased by one ($\sigma^{(1,0)}(t)$ and $\sigma^{(0,1)}(t)$). The time evolution of these auxiliary operators is again described by a differential equation which depends on other operators for which one of the indices is either increased or lowered by one, but cannot become negative. The time evolution of these higher order auxiliary operators are again described by a differential equation which has a very similar form and depends on higher order auxiliary operators (the hierarchy) [35].

The HEoM approach is exact if infinitely many auxiliary operators are taken into account. In practice however the number of auxiliary operators is truncated by defining a depth of the hierarchy N_{depth}. The auxiliary operators for which the sum of the indices is larger than the depth are not included. We use a fourth order Runga-Kutta method to numerical integrate the set of differential equations and calculate the (two-dimensional) spectra [67]. When the quantum system is in the ground state there is no coupling between the chromophores and environment. The equilibrium state for the phonon modes in this case is when all auxiliary operators are equal to zero. When the system is excited at $t = 0$ by a laser pulse this is no longer the equilibrium state due to the coupling between the quantum system and the environment. It is assumed that the laser pulse only excites the quantum system and does not interact with the phonon modes. After the quantum system is excited there will be an exchange of energy with the environment until the new equilibrium state is reached, eventually resulting in non-zero constant values of the auxiliary operators.

We assume that the spectral density, which quantifies the coupling to the phonon modes and their spectral density, is of Debye type. This corresponds to the overdamped Brownian oscillator model with a harmonic potential. We do not include the Matsubara frequencies; This results in a high temperature approximation and is valid when $k/(M\gamma k_B Tc) << 1$.

2.3 Results and discussion

2.3.1 Stokes shift for a single two-level quantum site

In this subsection we consider a single two-level quantum site which is coupled to a single Brownian oscillator that is driven by a heat bath. When the quantum site is in the ground state the minimum of the potential of the Brownian oscillator is located at $x_0 = 0$. When the quantum site is in the excited state the minimum of the potential is shifted to $x_0 = -\frac{hcD}{k}$ due to the feedback of the quantum site. This subsequently leads to a shift in the central frequency, the so called Stokes shift, of the quantum site

$$\Delta\omega_{Stokes} = \Delta x_0 D = -\frac{hcD^2}{k}. \tag{2.3.1}$$

It takes time, however, before the position of the Brownian oscillator is adjusted to the new potential. In the strongly overdamped limit $\gamma >> 2\sqrt{\frac{k}{M}}$ the correlation function for the coordinate of the Brownian oscillator is given by [53]

$$< x(t)x(0) >= \frac{k_B T}{k} e^{-\frac{t}{t_c}}, \tag{2.3.2}$$

where $t_c = \frac{M\gamma}{k}$ is the correlation time. The prefactor $\sqrt{\frac{k_B T}{k}}$ determines the amplitude of the oscillations of the Brownian oscillator. The factor is directly related to the width of the peaks in the spectra resulting from the quantum site, because of the linear dependence of the transition energy on the position of the Brownian oscillator. In the overdamped limit the Brownian oscillator model thus reduces to two parameters, the correlation time t_c and the size of the fluctuations of the transition frequency $\lambda = D\sqrt{\frac{k_B T}{k}}$.

In Fig. 2.3.1 the simulated two-dimensional spectra are shown for the single quantum site for waiting times $t_2 = 0$ ps and $t_2 = 5$ ps calculated using the different methods for the parameters specified in Table 2.3.1. The quantum feedback during the waiting time is identical for the Ehrenfest (Ehr)- and surface hopping (SH) method since there is only a single eigenstate in the first excitation manifold. Furthermore, the feedback during the t_1 and t_3 does not affect the spectra since these times are much shorter than the correlation time of the Brownian oscillator. The spectra calculated using the Ehrenfest method and surface hopping method are, therefore, identical for the single quantum site

Δt	0.001 ps	t_c	2.5 ps	T	300 K
$t_1^{\max}$	0.5 ps	γ	50 ps^{-1}	N_{samples}	50000
$t_3^{\max}$	0.5 ps	λ	195 cm^{-1}	N_{depth}	80
T_1	1 ps	ω_0	12000 cm^{-1}		

Table 2.3.1: The parameters for the single quantum site simulations.

and depicted only once in Fig. 2.3.1. We tested that the employed time step of 1 fs was sufficiently small to eliminate observable numerical errors due to the propagation method. The spectra are the sum of the groundstate bleach

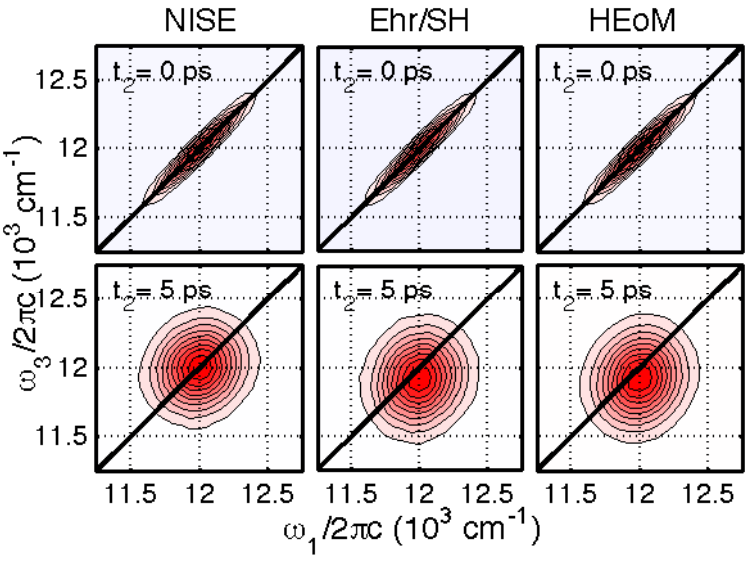

Figure 2.3.1: Simulated two-dimensional spectra for a single quantum-site for $t_2 = 0$ ps and $t_2 = 5$ ps using the NISE-, Ehrenfest/surface hopping- and HEoM method (left to right). The contour levels are plotted at every 10 % of the maximum absolute peak value in the spectra. The red color indicates negative valued peaks and the white color denotes zero intensity.

and stimulated emission diagrams in Fig. 2.2.3. The excited state absorption diagrams do not contribute to these spectra, since we are considering a single two-level quantum site. When the waiting time is 0, the spectra for the three calculations are essentially identical, showing a diagonally elongated peak with central position at $\omega_3 = \omega_0 = 12000$ cm^{-1}. The peak is diagonally elongated because the dephasing time of the response function ($(\lambda c)^{-1} = 0.17$ ps) and the waiting time both are short compared to the correlation time ($t_c = 2.5$ ps) of the Brownian oscillator. Therefore, there is no time for the Brownian oscillator to change coordinate, so that the pump and probe frequency are equal. For the same reason the NISE-method, which does not include the feedback, gives the same result as the Ehrenfest/surface hopping method, since there is no time for the Brownian oscillator to adjust to the new potential. When $t_2 = 5$ ps, elliptical peaks are obtained for all three calculations due to spectral diffusion, caused by the fact that the fluctuations in the oscillator's displacement cause fluctuations in the transition frequency of the quantum site. When there is no feedback, the central peak position along ω_3 is still $\omega_3 = 12000$ cm^{-1}, because the average coordinate of the Brownian oscillator remains $x_0 = 0$. But for the calculations including the feedback (Ehrenfest/surface hopping and HEoM) the central peak position along ω_3 is shifted to a lower value due to the Stokes shift, since there is enough time for the Brownian oscillator to adjust to the shift in the potential. Energy has transferred from the quantum system to the environment. The Ehrenfest/surface hopping and HEoM methods show identical behavior.

During the waiting time the quantum system is in the groundstate for the groundstate bleach diagrams and in the excited state for the stimulated emission diagrams. Consequently only the stimulated emission diagrams include the Stokes shift during the waiting time for the calculations including the feedback. The total spectra for $t_2 = 5$ ps show a single peak which is the sum of a GB contribution with central peak position along ω_3 at the central frequency ω_0 and a SE contribution with a central peak position located at a lower probe frequency due to the Stokes shift. Only a single peak is observed since the linewidths of the two contributions are larger than the Stokes shift. In Fig. 2.3.2 the central peak position along ω_3 for the SE diagrams as a function of the waiting time is shown for the three calculations. If there is no feedback the frequency stays approximately constant around the central frequency of the quantum site. For the calculations including the feedback the central frequency decreases as the waiting time is increased until the new equilibrium is reached. According to

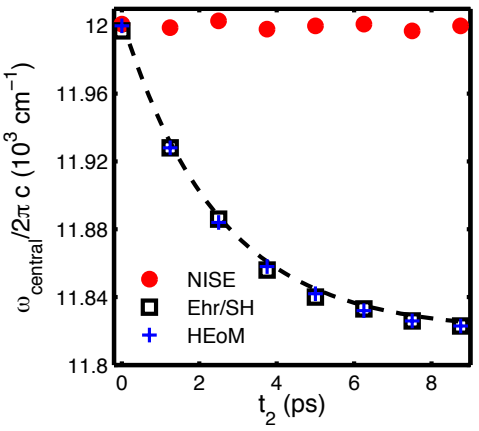

Figure 2.3.2: Central peak position along the ω_3 axis of the two-dimensional spectra resulting from the stimulated emission diagrams for the single quantum site as a function of the waiting time t_2, for spectra calculated using the NISE- (red circles), Ehrenfest/surface hopping- (squares) and HEoM method (blue crosses). The dashed line is the result of an exponential fit $\overline{\omega}_3(t) = \overline{\omega}_3(\infty) - \Delta\omega_{\text{stokes}} e^{-t/\tau_{\text{stokes}}}$.

Eq. 2.3.1, it is expected for the parameters used that the frequency is shifted by $\Delta\omega_{\text{stokes}} = 183$ cm^{-1}, which corresponds nicely with shifts observed for the Ehrenfest/surface hopping- and HEoM method. The exponential fit for the peak position as a function of the waiting time for the Ehrenfest method (black dashed line) gives a relaxation constant $\tau_{\text{stokes}} = 2.6$ ps, which is essentially equal to the correlation time of the bath ($t_c = 2.5$ ps), as is expected.

The present method relies on (non-equilibrium) trajectories to calculate the response and not on the correlation function. The Stokes shift here thus arises from the inclusion of the feedback force, where correlation function based methods usually account for this physical phenomena through the imaginary part of the quantum correlation function [53].

2.3.2 Two-dimensional spectra for a coupled dimer

In this subsection we consider two coupled quantum sites with different central excitation frequencies, and compare the two-dimensional spectra obtained using the four different methods. We assume that the parameters describing the Brownian oscillators and coupling to the heat bath are equal for both quantum sites. We use the parameters given in Table 2.3.2.

We verified that the employed time step given in the table was sufficiently small to eliminate observable numerical errors due to the propagation method. In Fig. 2.3.3 the linear absorption spectra are shown for calculations using the NISE/surface hopping-, Ehrenfest and HEoM method. For linear spectra calculations, the NISE and surface hopping method are identical since they both neglect the feedback during the coherence time t_1. The linear spectra obtained essentially show no differences. This results from the fact that the dephasing time is shorter than the correlation time of the environment, so that the difference in dynamics of the environment has no time to affect the spectrum.

In Fig. 2.3.4 the two-dimensional spectra for the coupled dimer are shown for the four different methods for waiting times $t_2 = 0$ ps and $t_2 = 12$ ps. For the parameters chosen the correlation time of the environment is short compared to the population transfer time. In this way we can distinguish between effects in the spectra resulting directly from dynamics of the environment (such as spectral diffusion and the Stokes shift) which happen on a short time scale and the population transfer taking place at longer times. When the waiting time is 0 ps all four calculated spectra are identical. There is a positive cross peak (blue color) which results from the excited state absorption diagrams. When the waiting time is 12 ps the lineshapes are broader due to spectral diffusion. There

Δt	0.005 ps	γ	50 ps^{-1}	T	300 K
$t_1^{\max}$	0.5 ps	λ	198 cm^{-1}	N_{samples}	60000
$t_3^{\max}$	0.5 ps	J	100 cm^{-1}	N_{depth}	20
T_1	1 ps	ω_{01}	11500 cm^{-1}		
t_c	0.22 ps	ω_{01}	12000 cm^{-1}		

Table 2.3.2: Parameters used for simulations of the dimer coupled to the classical system and heat bath.

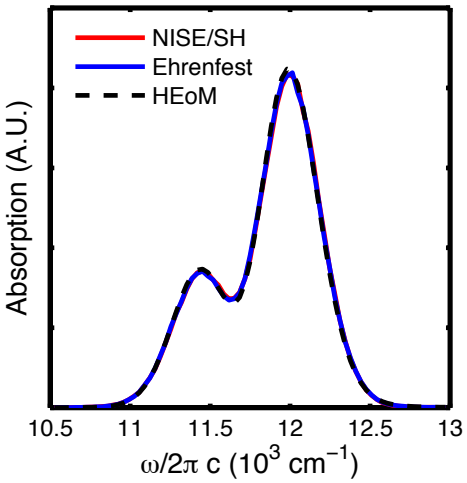

Figure 2.3.3: Linear spectrum for the coupled dimer calculated using the NISE/surface hopping- (red line), Ehrenfest- (blue line), and HEoM (black dashed line) method.

are clear differences in the spectra for the four methods. Especially the cross-peaks show different intensities when the waiting time is increased. In Fig. 2.3.5 the intensities of the upper ($\omega_1 = 11488$ cm^{-1}) and lower ($\omega_1 = 12012$ cm^{-1}) cross peaks are shown as a function of the waiting time for the four methods. The growth of the lower cross peak is determined by the population transfer from the high energy eigenstate (which is initially excited by the pump pulse) to the low energy eigenstate. This growth of the lower cross peak is smallest for the NISE method and largest for the HEoM method. The surface hopping method shows a much larger growth of the cross-peak than the NISE method and reproduces the HEoM result quite well. The Ehrenfest approach is somewhere in between the NISE and surface hopping result. The growth of the upper cross peak is determined by population transfer from the low energy eigenstate to the high energy eigenstate during the waiting time. The NISE method gives rise to a large (negative) growth of this cross peak indicating strong uphill energy transfer. For the HEoM method the intensity of the cross peak does not change much. The surface hopping method again provides the result closest to the HEoM.

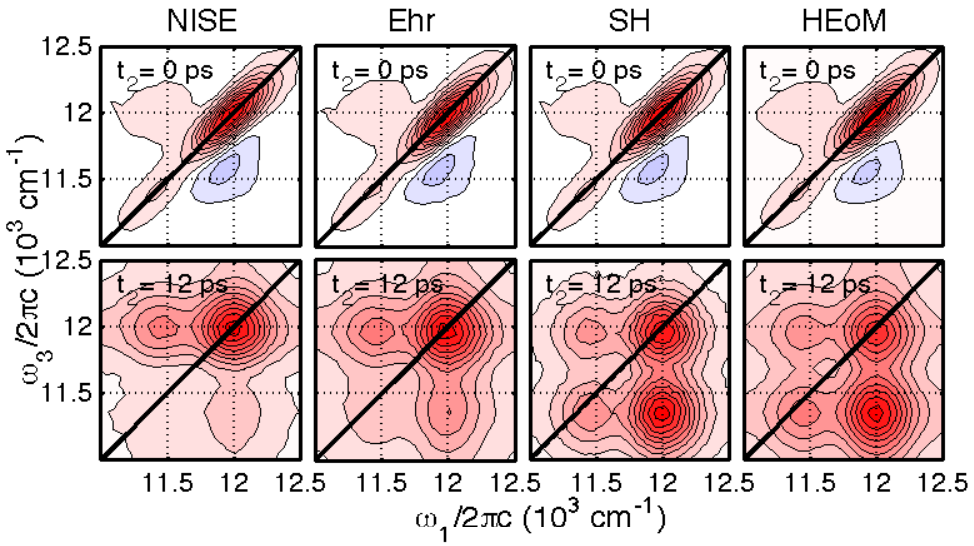

Figure 2.3.4: Simulated two-dimensional spectra using the NISE-, Ehrenfest-, surface hopping- and HEoM methods for the coupled dimer for waiting times $t_2 = 0$ ps and $t_2 = 12$ ps. The red colors indicate negative valued peaks and the blue colors indicate positive valued peaks. The contour levels are plotted at intervals of 10% of the absolute maximum of the spectrum starting at 95%.

The growth of the cross peaks are determined by the population transfer between the instantaneous eigenstates. For the HEoM method it is not possible to calculate the population transfer between the instantaneous eigenstates because the site energies as a function of time are not explicitly known. This is because the HEoM is an ensemble average method and thus does not allow the extraction of information of the Hamiltonian of individual trajectories from the reduced density matrix at all times. In Fig. 2.3.6 the population transfer between the instantaneous eigenstates is plotted as a function of time for the NISE-, Ehrenfest- and surface hopping method upon initial excitation of the low and high energy eigenstate. For the NISE method the equilibrium situation is reached for both situations, when both the low and high energy eigenstates have equal occupation probabilities, which is a direct consequence of the infinite tem-

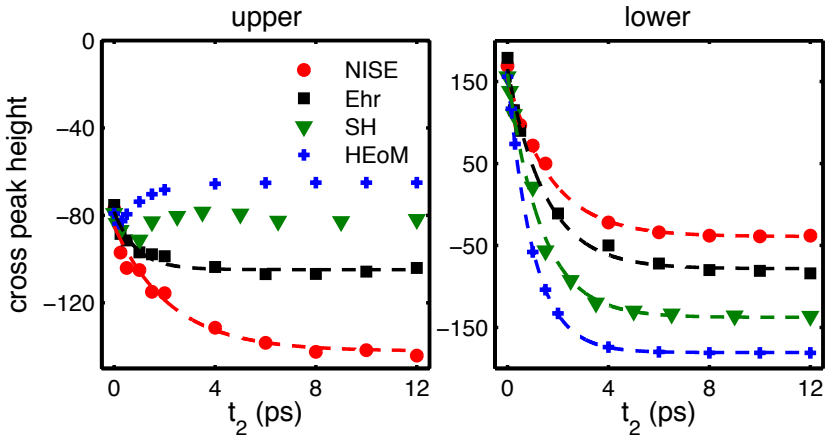

Figure 2.3.5: Peak height of the upper cross peak located at $\omega_1 \approx 11488$ cm^{-1} (right graph) and lower cross peak located at $\omega_1 \approx 12012$ cm^{-1} (left graph) as a function of the waiting time for the NISE- (red circles), Ehrenfest- (squares), surface hopping (triangles) and HEoM (plusses) method. The symbols represent data points taken from the calculated two-dimensional spectra and the dashed lines are results of exponential fits ($I(t) = I_0(\infty) + \Delta_{\text{grow}} e^{-\Gamma_d t}$).

perature approximation [46]. This is only valid when the thermal energy is large compared to the energy difference between the states, which is not the case for the parameters chosen. In contrary to NISE, it is more likely for the Ehrenfest method to end up in the low energy eigenstate than in the high energy eigenstate when the energy difference is larger than or comparable to the thermal energy. For the situation where the high energy eigenstate is initially excited by the pump pulse, the Stokes shift will lower the energy and the energy difference between the eigenstates is decreased. This increases the population transfer from the high energy eigenstate to the low energy eigenstate resulting in a larger growth of the lower cross-peak, as compared to NISE. For the upper cross peak the exact opposite is observed since the Stokes shift increases the energy difference between the eigenstates, resulting in less population transfer. Due to the mean field approach, the Ehrenfest method does not result in a Boltzmann distribution in the quantum system, however, as previously discussed in detail by Tully *et*

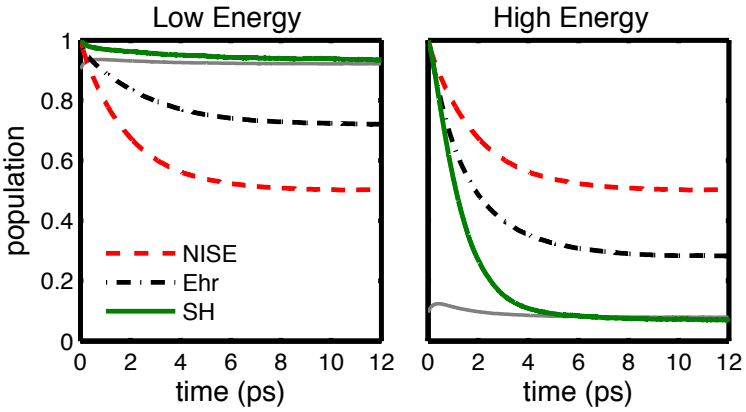

Figure 2.3.6: Ensemble average of the populations of the instantaneous eigenstates as a function of time for a coupled dimer using the NISE- (dashed), Ehrenfest- (dashed-dot) and surface hopping method (solid). In the left graph the low energy eigenstate is initially excited and in the right one the high energy eigenstate. The solid grey line denotes the expected equilibrium populations of the instantaneous eigenstates if a Boltzmann distribution within the quantum system is obeyed (calculated for the Ehrenfest trajectory).

al. [70]. This explains the difference with the HEoM result, which shows an even larger growth of the lower cross peak. The surface hopping method shows the largest energy transfer to the low energy eigenstate upon initial excitation of the high energy eigenstate and smallest transfer to the high energy state upon initial excitation of the low energy eigenstate, as compared to NISE and Ehrenfest. The surface hopping method, in equilibrium, leads to a Boltzmann distribution in the quantum system. This is intrinsic in the method, since a hop to a state higher in energy can only be made if there is sufficient energy in the classical system which is coupled to the heat bath (temperature dependent). The energy transfer from the low to high energy eigenstate is, therefore, unlikely since most of the time there is not sufficient energy in the classical system to make the transition. The surface hopping method clearly gives the result closest to the HEoM method although it does not reproduce the method exactly. In the HEoM approach the bath and the dimer both are described quantum mechanically. The equilibrium

for the HEoM, therefore, is a Boltzmann distribution of the total system, whereas for the surface hopping method there is only a Boltzmann distribution within the degrees of freedom considered quantum mechanically.

Since the correlation time of the bath is short, the growth of the cross peaks after several correlation times solely depends on the population transfer. The decay time Γ_d of the cross peak height should, therefore, be identical to the decay rate of the population transfer in Fig. 2.3.6. The results for an exponential fit of the cross peak height and population transfer are summarized in Table 2.3.3.

From this Table it is clear that the fit parameters for the population transfer from the low energy eigenstate to the high energy one of Fig. 2.3.6 and the corresponding growth of the upper cross peak in Fig. 2.3.5 do not coincide. The changes in peak height happen on a short timescale where spectral diffusion still takes place. Therefore, the parameters do not match very well. For the lower cross peak, where the changes in peak height occur at longer waiting times, the fit parameters coincide with the parameters obtained for the population transfer from the high energy eigenstate to low energy one.

The energy difference chosen here is quite large compared to the thermal energy so that we could study the cross peak growth independently of the diagonal peaks. The surface hopping method is able to reproduce the exact result quite

	cross-peak Γ_d (ps^{-1})	pop trans. Γ_d (ps^{-1})
NISE upper	0.45	0.52
Ehr upper	1.14	0.40
SH upper	..	0.29
NISE lower	0.59	0.56
Ehr lower	0.67	0.62
SH lower	0.75	0.79
HEoM lower	0.99	..

Table 2.3.3: Results of the exponential fits $I(t) = I_0(\infty) + \Delta_{\mathrm{grow}} e^{-\Gamma_d t}$ of the curves in Fig. 2.3.6 and 2.3.5 for the upper and lower cross peaks. The .. indicates that a fit parameter is missing. For the SH upper cross peak growth the data is unsuitable for an exponential fit because the changes occur on short timescales where spectral diffusion still takes place, whereas for the HEoM approach calculations of population transfer between eigenstates are impossible.

well. The Ehrenfest method will give results closer to the HEoM method when the energy difference is smaller. In the extreme situation where the sites have the same transition energies, the NISE- and Ehrenfest methods both result in a Boltzmann distribution. When there is a Stokes shift, the energy difference between the eigenstates will increase however. This will decrease the population transfer if the Stokes shift is large compared to the coupling, an effect that influences the shape of the two-dimensional spectra. Such a trapping effect is included in the Ehrenfest, surface hopping and HEoM methods, but is neglected in the NISE method.

In general the correlation time of the environment is not necessary small compared to the transfer time. In this case the transfer time cannot be obtained simply by measuring the height of the cross peaks. Simulations are, therefore, needed for interpreting the experimental spectra. Furthermore, in real systems the correlation functions may not be in the overdamped limit and the population transfer may show coherent oscillations resulting in very complex spectra. Such effects can be included in the Ehrenfest- and surface hopping method. We have chosen for harmonic potentials resulting in Gaussian dynamics to be able to compare the methods with the exact result provided by HEoM. When different forms for the potentials are used, the signature of the environment can become much more pronounced [62]. For such potentials HEoM is no longer exact.

2.3.3 Thermalization Ehrenfest method

From Fig. 2.3.6, the probability for finding the coupled dimer in the low energy eigenstate in equilibrium (long waiting time) for the Ehrenfest method is $P_L = 0.72$. If a Boltzmann distribution is obeyed the probability to occupy the low energy instantaneous eigenstate in equilibrium for the parameters used is $P_L = 0.9$. For the Ehrenfest method the quantum system solely does not obey a Boltzmann distribution. When the Brownian oscillators are not coupled to the heat bath the energy within the quantum plus classical system is conserved which is clear from the Hamiltonian in Eq. 2.2.1. Therefore, when there is a coupling to the heat bath the total quantum classical system is expected to give a Boltzmann distribution of energy. When a Boltzmann distribution is obeyed the probability for the system to have a certain energy is given by

$$D(T, E) = \frac{g(E)e^{-\beta E}}{Z(T)}, \tag{2.3.3}$$

where g(E) denotes the degeneracy, i.e. the number of available states of that energy, Z(T) denotes the partition function, and $\beta = 1/k_B T$. In the left graph of Fig. 2.3.7 the probability that the system of Sec. 2.3.2 has a specific energy is plotted for different temperatures. This figure was created by counting the number of times the quantum-classical system has a specific energy, with the quantum system in a single excited state, over a trajectory of 10^8 time steps. When the temperature is increased, higher energy states become more probable as is expected. The quotient of two distributions of energy for different temperatures of a certain system is independent of the degeneracy

$$\frac{D(T_1, E)}{D(T_2, E)} = \frac{Z(T_2)}{Z(T_1)} e^{(\beta_2 - \beta_1)E}. \tag{2.3.4}$$

In the right graph of Fig. 2.3.7, the quotient between distributions with different temperatures is plotted. The black dashed lines show the results expected

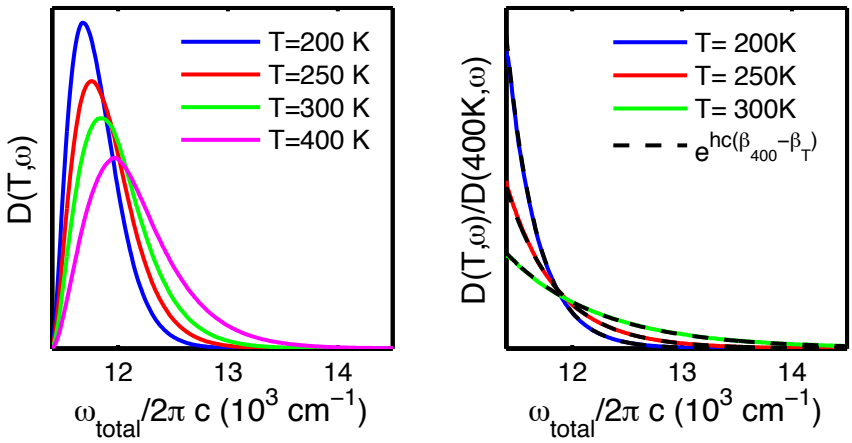

Figure 2.3.7: Left Distribution of the total energy of the quantum-classical system for the coupled dimer of Sec. 2.3.2 in a single excited state, for temperatures $T = 200$ K, $T = 250$ K, $T = 300$ K, and $T = 400$ K. right: Quotient of the distributions for $T = 200$ K, $T = 250$ K and $T = 300$ K in the top graph and the distribution for $T = 400$ K. The black dashed lines show the same quotients expected if the distributions of energy obey Boltzmann statistics.

if the distributions obey Boltzmann statistics Eq. 2.3.4. The quotient between distributions for different temperatures match the black dashed lines perfectly. We, thus conclude that when using the Ehrenfest method a Boltzmann distribution within the quantum system is not obtained, however, the total energy of the quantum and classical systems does obey a Boltzmann distribution as is expected.

2.4 Conclusions

In this chapter we presented two novel approaches to perform mixed quantum-classical simulations of two-dimensional spectra. The methods couple the quantum and classical system in a self-consistent way by including the change in potential the classical system feels when transitions occur in the quantum mechanical system using the Ehrenfest method and surface hopping method, respectively. We studied how this interaction influences the shape of two-dimensional spectra by comparing the two different methods, to the NISE method where this feedback is neglected. As a benchmark we compared the spectra with the HEoM method.

We showed for a single quantum site that the feedback of the quantum system leads to a Stokes shift when the dephasing-time of the response function is comparable to (or longer than) the correlation time of the classical system. The waiting time dependence of the magnitude of the Stokes shift is identical to the correlation time of the environment. For a single quantum site the Ehrenfest and surface hopping method are identical and the obtained results match the HEoM method perfectly in contrast to the NISE method, where the Stokes shift is absent.

For two coupled quantum sites that have different central excitation frequencies we showed that the four methods result in identical spectra when the waiting time is zero. For non-zero waiting times the growth of the cross peaks are substantially different for the three mixed quantum-classical methods (NISE, Ehrenfest and surface hopping). We showed that the difference in the growth of the cross peaks for the NISE-, Ehrenfest and surface hopping method are directly related to the differences in population transfer for the three methods. First of all, the Stokes shift resulting from the quantum feedback of the quantum system influences the population transfer between the eigenstates. When the low energy eigenstate is excited, the Stokes shift increases the energy difference between the

eigenstates which decreases the rate of population transfer to the high energy eigenstate. Vice versa, when the high energy eigenstate is initially excited, the energy difference between the eigenstates is reduced by the Stokes shift and the rate of population transfer is increased. The Ehrenfest method and surface hopping method both include these effects but their respective ways of dealing with the quantum feedback is fundamentally different leading to different two-dimensional spectra. The NISE method neglects the quantum feedback and does not include such effects. Furthermore, NISE is a infinite temperature approximation and, therefore, does not lead to the correct thermal equilibrium of the quantum system when the energy differences between states are larger than the thermal energy. The Ehrenfest method gives an improved behavior but also does not obey Boltzmann statistics in the quantum system in equilibrium, because the use of a mean field theory. The surface hopping method method does lead to a Boltzmann distribution in the quantum system in equilibrium and, therefore, is able to reproduce the HEoM result. l In conclusion, including the feedback using the surface hopping method and Ehrenfest method is a significant improvement compared to the NISE method, as it allows for a description of the Stokes shift. The surface hopping method is the better way to include the feedback, since it leads to a Boltzmann distribution in the quantum system in equilibrium. The presented approach allows one to account for non-Condon and non-Gaussian effects as well as a general classical environment that may be described with a MD simulation as long as the bath degrees of freedom can be considered classical. If important degrees of freedom with frequencies larger than or comparable to k_BT are present these need to be included in the quantum system. The presented method does not reproduce the Hierarchical Equations of Motion exactly, but it presents a leap in the right direction. The computational cost for treating larger systems is expected to be significantly lower for the surface hopping method [60] compared to HEoM even though considerable efforts have been made developing time efficient and highly parallel HEoM codes [66, 76, 77].

Chapter 3

OH-stretching in synthetic hydrogen bonded chains

We study hydrogen bond dynamics in stereoselectively synthesized polyalcohols by combining linear and two-dimensional (2D) infrared spectroscopy experiments with simulations. We consider two variants of the polyalcohols: The all-*syn* and all-*anti* tetrol, which because of their different stereochemistry of the hydroxyl groups, form a linear hydrogen bonded chain that is stable for tens of picoseconds, or a system where hydrogen bonds are formed and broken on a picosecond timescale, respectively. The differences in structure and hydrogen bond dynamics gives rise to significant differences in the linear spectra for the two compounds. Furthermore, we show that the stronger hydrogen bonding for the all-*syn* variant leads to faster fluctuations of the site frequencies than for the all-*anti* one, which is reflected in the higher degree of homogeneous broadening in the 2D-spectra. Because of the different stereochemistry the coupling in the all-*syn* molecule is stronger than for the all-*anti* one, which leads to a faster delocalization of a local excitation. This explains the previously observed pump-frequency independent vibrational lifetime for the all-*syn* variant, since the excitation loses the memory of the pump-frequency before relaxation. For the all-*anti* form the coupling is weak and the excitation remains in the initially excited state, maintaining the memory of the pump-frequency.

This chapter is based on C. P. van der Vegte, S. Knop, P. Vöhringer, J. Knoester, T. L. C. Jansen J. Phys. Chem. B, **118**, 6256 (2014)

3.1 Introduction

Hydrogen-bonding is a key element in the structure and dynamics of chemical and bio-molecular structures. The bonding primarily results from a strong dipole-dipole attraction and the strength can range from being as weak as van der Waals forces to as strong as covalent bonds [78]. Intramolecular hydrogen-bonds are responsible for the secondary and tertiary structure of proteins which determines their function [79]. In associated liquids like liquid water, hydrogen-bonded networks form semi-rigid systems that are important for many unusual properties such as the high efficiency of proton transfer [56, 80–82], the density change as a function of temperature and the high boiling temperature. Furthermore, hydrogen bonded chains play an important role in the function of for example water transporting proteins [83, 84], anti-biotic peptides [85, 86], and artificial fuel-cells [87]. The breaking and forming of hydrogen bonds in such systems is, however, highly stochastic in space and time, which makes it hard to obtain information on the local dynamics of the networks. In this chapter we study the hydrogen bond structure and dynamics in synthetic hydrogen-bonded chains by combining experiments with simulations.

Two-dimensional infrared spectroscopy (2DIR) has proven to be successful in studying hydrogen-bond dynamics down to a femtosecond timescale [6, 15–17, 37, 88–98]. In such non-linear spectroscopy experiments an OH-stretching mode is excited by a pump pulse. After a waiting time, that can be anywhere in the range from femtoseconds to tens of picoseconds, the system is probed by a probe pulse. During this waiting time the excitation can transfer, relaxation can take place, and structural changes like the breaking of a hydrogen-bond can occur. The transition frequencies of the stretching modes of the OH-groups strongly depend on their local environment [99]. The stronger the hydroxyl group is hydrogen bonded the lower its transition frequency. When a hydrogen bond is broken or formed during the waiting time, a cross-peak in the 2DIR spectrum will appear [15]. Furthermore, the off-diagonal width of the diagonal peaks, as a function of the waiting time, gives information on the timescales of the fluctuations of the local environment surrounding the reporter groups [9]. Extensive studies of the dynamics and hydrogen bond structure have been performed on bulk water [100, 101] and isotope labeled mixtures like HOD-D_2O [37, 92, 102]. The 2DIR-spectra are, however, averaged over an ensemble, which makes it hard to extract direct information on the local hydrogen bond dynamics

for liquids. Therefore, theoretical studies have been crucial for interpreting the spectra [48, 93, 94, 96, 103–105].

To study hydrogen-bonding in a more systematic and controlled way, stereoselectively synthesized polyalcohols have been introduced as low-dimensional model systems [89, 106, 107]. The hydroxyl groups of the polyalcohols can form a hydrogen bonded network and the number of hydroxyl groups along the quasi one-dimensional chain can be varied. In this chapter we will focus on the tetrol. We study two variants of the tetrols: the all-*syn* and all-*anti* form, which have a different stereochemistry, and are schematically shown in Fig. 3.1.1. For the all-*syn* molecule hydrogen bonding is favored, while for the all-*anti* molecule the hydrogen bonding is hindered by the orientation of methyl groups. The two molecules show remarkably different linear absorption spectra, 2D-spectra, and waiting time dynamics [106, 107].

Previously Geva and coworkers calculated the linear absorption spectra, linear emission spectra, and the lifetime of the vibrationally excited state for the all-*syn* and all-*anti* molecules [108] using a mixed quantum-classical Liouville approach for a single chromophore [61–64]. In this chapter we combine experiments with an all-atomistic self-consistent mixed quantum-classical simulation

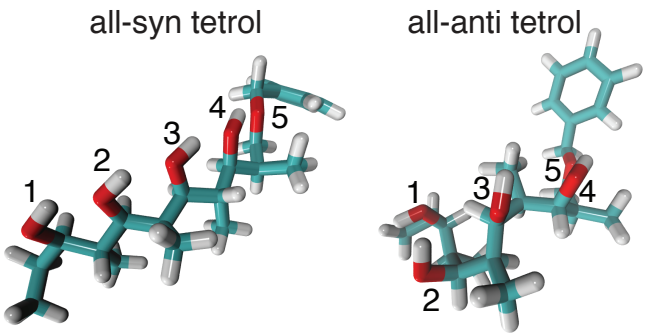

Figure 3.1.1: Picture of the all-*syn* tetrol (left) and all-*anti* tetrol (right) molecules. The hydroxyl sites are labeled from 1-4 and the oxygen of the backbone structure to which site 4 can be hydrogen bonded is labeled by number 5 for both molecules. Because of the stereochemical orientation of the methyl groups, intramolecular hydrogen bonds are strong for the all-*syn* compound and unfavorable for the all-*anti* compound.

method to further address the differences between the all-*syn* and all-*anti* tetrol compounds. We simulate the linear absorption spectra and 2DIR spectra in the OH-stretching spectral region for both molecules and compare to the experimental data. We treat all hydroxyl stretches quantum-mechanically, which allows us to include the coupling between hydroxyl stretches in a rigorous way. We show that the differences in hydrogen-bond dynamics in the two molecules gives rise to differences in the absorption crossections, transition frequencies of the hydroxyl stretches, population transfer within the molecules, and line-broadening mechanisms.

The remainder of this chapter is outlined as follows: In section 3.2.1 we briefly explain the experimental setup and how the molecules where synthesized. In section 3.2.2 we describe the all-atomistic mixed quantum-classical method that is used to calculate the linear and 2DIR spectra. We use the surface hopping method to self-consistently couple the quantum subsystem to the classical subsystem. In section 3.3.1 we show results for the linear spectrum. We explain the observed differences in absorption cross sections, peak intensities, peak shapes, and peak positions for the both compounds. Furthermore, the nature of the eigenstates for both molecules is discussed. In section 3.3.2 we focus on the 2DIR spectra. We relate the differences in the broadening of the diagonal peaks to the correlation times of the site-frequencies. Furthermore, we calculate the population transfer of an excitation in the molecules as a function of the waiting time. This together gives an explanation for the experimentally observed differences in the pump-frequency dependence of the lifetime of the hydroxyl stretch. Finally in section 3.4 we draw our conclusions.

3.2 Method

3.2.1 Experiment

The polyalcohols, (2R, 3S, 4S, 5S, 6R, 7S, 8R, 9R)-1-Benzyloxy-2,4,6,8-tetramethylundecane-3,5,7,9-tetrol(all-*syn* tetrol) and (2R, 3R, 4S, 5S, 6R, 7R, 8R, 9R)-1-Benzyloxy-2,4,6,8-tetramethylundecane-3,5,7,9-tetrol (all-*anti* tetrol) where synthesized diastereo selectively using the iterative Boron-assisted aldol condensation developed by Scott and Paterson [109]. Solutions of these compounds in deuterated chloroform ($CDCl_3$, Euriso-Top, $\geq$99.8%, dried over a 4 Å molecular sieve for several days) were prepared with a concentration of 6 mM or

less to ascertain that the formation of dimers and higher oligomers is negligible. Such solutions give rise to an absorbance in the OH-stretching region of 0.25 at an optical path length of 2 mm. Stationary (i.e. linear) Fourier transform infrared (FTIR) absorption spectra were recorded with a spectral resolution of 2 cm^{-1} using a commercial spectrometer (Thermo Scientific, Nicolet 5700). Two-dimensional infrared spectroscopy (2DIR) was conducted in the dynamic hole burning setup of Hamm and Hochstrasser [6] using a laser system that was described earlier [106, 107]. Briefly, a femtosecond Ti:sapphire front-end (Clark-MXR, CPA 2001) was used to synchronously pump two optical parametric amplifiers (OPA), each of which equipped with a type-I AgGaS2 difference frequency module (DFM) for generating mid-IR pulses in the OH-stretching region. One of the OPA/DFM devices served as the ultrafast pump source while the other provided ultrafast probe light. An etalon was used to shape the pump pulses into a Lorentzian spectral profile with a half width of 24 cm^{-1}. Pump and probe pulses were focused into the 2-mm thick sample using a 45° off axis parabolic Au mirror (OAP) with an effective focal length of 100 mm. An identical OAP was used to recollimate the beams behind the sample and to direct the probe pulses onto the entrance slit of a 0.2-m monochromator whose exit slit was replaced by a 2x32 element HgCdTe array detector (Infrared Associates) for probe frequency-resolved referenced detection. Spectra were recorded with the relative pump-probe polarization set to the magic angle.

3.2.2 Theory

We use fullly atomistic mixed quantum-classical simulations to calculate the optical response of the polyalcohols. The quantum and classical subsystem are coupled to each other in a self consistent way using the surface hopping algorithm [52, 72]. Here we only give a brief description of the method. More details are provided in the appendices.

A simulation box contains a single polyalcohol molecule (either *all*-syn or *all*-anti tetrol) and 500 chloroform molecules. A single polyalcohol molecule is sufficient because the concentrations used in the experiments are low, so that intermolecular bonds are negligible [106]. We are interested in the OH-stretching region of the spectrum and, therefore, treat the stretching modes of the hydroxyl groups quantum mechanically and all other degrees of freedom classically. The OH-stretching modes are considered as coupled three level systems and are described by the Frenkel exciton Hamiltonian. The transition frequencies and

transition dipoles from the groundstate to the first excited state of the hydroxyl sites are determined from the electric field along the hydroxyl stretch using the mapping of Skinner and coworkers [12]. This mapping was originally developed for OH-stretching modes in liquid water. The electric fields along each stretch is calculated at the point of the hydrogen atom by summing over the contributions of all the charged particles in the simulation box except for the hydrogen and oxygen atom that form the stretch. To determine the coupling between two sites, the transition dipole coupling approximation is used. The anharmonicity of the third level is assumed to have a constant value of 147.5 cm^{-1}, corresponding to the vacuum value of OH-stretching modes in liquid water [12]. The transition dipole to the third level (1-2 transition) is assumed to be $\vec{\mu}_i^{12} = \sqrt{2}\vec{\mu}_i^{01}$, which holds for harmonic oscillators. The quantum state is propagated by numerical integration of the Schrödinger equation assuming the Hamiltonian is constant for a short time step Δt [46].

The state of the classical system is determined by the positions $\mathbf{R}$ and velocities $\dot{\mathbf{R}}$ of all atoms in the simulation box. The potential energy of an atom depends on the position of all other particles in the simulation box with respect to its own, as well as on the state of the quantum system. The forces between the classical atoms are determined by the force field and computed using the GROMACS 4.5.5 distribution [110]. The OPLS force field is used for the bonded and Lennard-Jones forces [111, 112]. The charges of the atoms of the polyalcohols and chloroform solvent molecules are given in the SI and are derived from similar groups of the OPLS force field [112]. The three chloride atoms of each chloroform molecule have an independent Drude particle associated with them to account for polarization effects, giving an effective isotropic polarizability of 2.84333 $Å^3$ for each, to match the experimental value of 8.53 $Å^3$ [113]. The MKTOP program was used to generate the topology files for the polyalcohol molecules [114]. The bond distances are fixed using the LINCS algorithm [115] and the electrostatic potential is calculated using the Particle Mesh Ewald method with a cutoff radius of the real-space part of 1.5 nm.

The surface hopping algorithm [52, 72] is used to include the forces on the classical degrees of freedom due to excitations of the quantum system as was described in Sec. 2.2.2. The equations of motion for the classical and quantum system form a set of coupled differential equations which is propagated numerically with a time step of 1 fs. The linear and non-linear response functions are calculated by summing over the different Liouville pathways as was explained in

Sec. 2.2.3. Further details are provided in the appendices.

3.3 Results

3.3.1 Linear Spectra

The linear absorption spectra of the OH-stretching region for the all-*syn* tetrol and all-*anti* tetrol in liquid deuterated chloroform is shown in Fig. 3.3.1. The dashed grey lines show the measured spectrum and the black solid lines are obtained with the atomistic simulations. The simulated spectra are sampled over 1500 different starting configurations of the simulation box. For the all-*syn* tetrol the measured spectrum is very well reproduced by the simulation considering the approximations made. There is a broadband peak centered around 3390 cm^{-1} and a low intensity peak at 3615 cm^{-1}. The broadband peak corresponds to the OH-stretching of the hydroxyl groups that are hydrogen bonded. This peak is symmetric and has a nearly Gaussian shape. The small peak corresponds to the OH-stretching of free hydroxyl groups but has a weak intensity indicating that most of the time the hydroxyl stretches are hydrogen bonded.

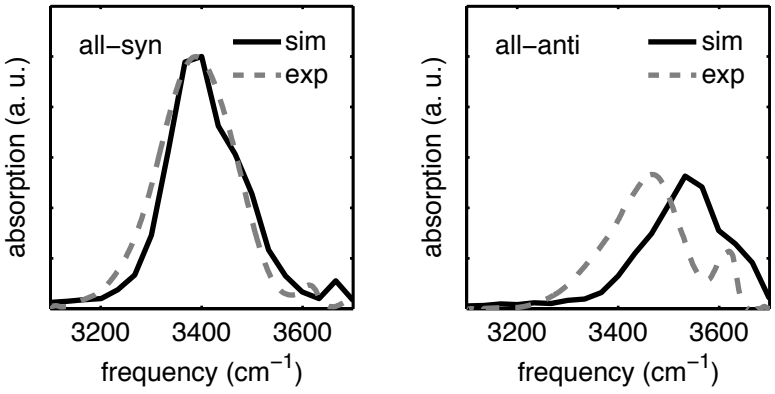

Figure 3.3.1: Linear spectra for the all-*syn* tetrol (left) and all-*anti* tetrol (right). The solid lines represent the simulated spectra and the dashed lines the experimental spectrum. The experimental spectra are plotted on the same scale.

The absorption spectrum of the all-*anti* tetrol is very different from the all-*syn* tetrol. First of all the total absorption cross section is smaller for the all-*anti* tetrol demonstrating a larger non-Condon effect [116]. There is a broadband peak at 3470 cm^{-1} and a narrow peak at 3620 cm^{-1} that again correspond to the stretching of hydrogen bonded and non-hydrogen bonded hydroxyl groups respectively. The broadband peak is, however, centered at a higher frequency compared to the all-*syn* tetrol and is no longer symmetric showing a long tail towards low frequencies. The narrow peak has gained intensity compared to the all-*syn* tetrol. The simulated spectrum for the all-*anti* tetrol reproduces the general spectral features of the measured spectrum but is shifted to the blue by 80 cm^{-1}. This deficiency might be due to the force field used or the mapping, which was created for liquid water [12], where the hydrogen bonding is stronger than for the all-*anti* tetrol.

The differences between the absorption spectra of the two molecules can be explained by their differences in hydrogen bond dynamics. In Fig. 3.3.2 the hydrogen bond lengths (H-O distances) of the all-*syn* tetrol and all-*anti* tetrol are plotted for a short trajectory of 20 ps where the quantum system was in the ground state. The bond-lengths for the all-*syn* tetrol are about 0.2 nm and remain stable over the simulation. The configuration of the molecule is most of the time very similar to the one shown in Fig. 3.1.1 although small fluctuations of the bond lengths and the angles between hydroxyl stretches occur. For the all-*anti* tetrol hydrogen bonds are still formed between neighboring hydroxyl groups despite its unfavorable stereochemistry. The hydrogen bonds are, however, weaker compared to the all-*syn* compound and are broken and formed multiple times within the short trajectory due to the thermal fluctuations. This is in agreement with previous Langevin dynamics simulations [107].

For the *syn*-tetrol the hydroxyl groups are oriented almost parallel (similar to Fig. 3.1.1) and the hydrogen bond lengths are shorter compared to the all-*anti* tetrol. This gives rise to stronger electric fields along the hydroxyl stretches, leading to stronger transition dipole moments and, therefore, a stronger absorption cross section. Since the hydrogen bonds are weaker for the all-*anti* tetrol, the broadband peak is shifted towards higher frequencies compared to the all-*syn* tetrol. The peak at high frequencies for the all-*syn* tetrol (3620 cm^{-1}) has a smaller intensity than the peak for the all-*anti* tetrol (3615 cm^{-1}) since the hydrogen bonds for the latter are more easily broken.

The site energy and nearest neighbor coupling distributions for the two

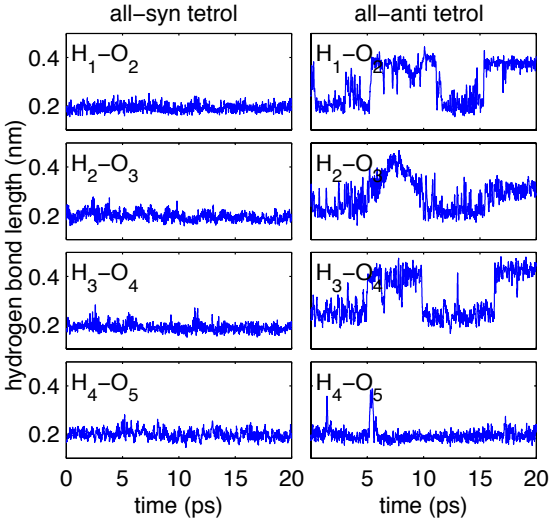

Figure 3.3.2: The hydrogen bond lengths between neighboring hydroxyl groups as a function of time for all-*syn* tetrol (left) and all-*anti* tetrol (right) for a trajectory of 20 ps.

molecules are plotted in Fig. 3.3.3. The site energy distributions for the all-*syn* tetrol are very symmetric and have a Gaussian form, which gives rise to the symmetric broadband peak in the spectrum. The site energy distributions for the all-*anti* tetrol are non-symmetric and show two peaks for each site corresponding to the hydrogen bonded and free cases. Strong hydrogen bonding is possible but is clearly hindered by the presence of the methyl groups. The distributions show long tails towards low frequencies (especially for site 2) giving rise to the asymmetric peak in the spectrum. The couplings for the all-*syn* tetrol are stronger (more negative) than for the all-*anti*. For the all-*syn* molecule the transition dipole moments of the hydroxyl stretches are almost parallel (Fig. 3.1.1) giving rise to a strong dipole-dipole coupling. For the all-*anti* tetrol the hydrogen bonds are weaker and, therefore, the transition dipoles are oriented more randomly leading to smaller couplings. Especially the coupling between sites 3 and 4 is very weak because of the bending of the molecule (Fig. 3.1.1).

The nature of the eigenstates is different for the two molecules due to their

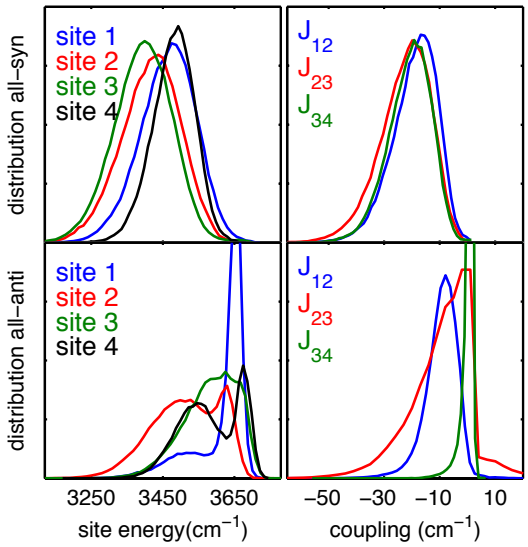

Figure 3.3.3: Distribution of the site energies (left) and nearest neighbor couplings (right) for the all-*syn* tetrol (top) and all-*anti* tetrol (bottom). The different site numbers correspond to the different hydroxyl groups as displayed in Fig. 3.1.1. The distributions where calculated from a trajectory of 200 ps.

differences in coupling strengths. The elements of the density matrix for the four eigenstates in the first excitation manifold are shown in Fig. 3.3.4, ensemble averaged over a trajectory of 200 ps. For the all-*syn* molecule the lowest energy eigenstate (eigenstate 1) corresponds to a collective in phase stretching mode of the hydroxyl groups, similar to the superradiant exciton state in linear J-aggregates [117]. This state is mainly localized on sites 2 and 3. The highest energy eigenstate (eigenstate 4) is most of the time localized at sites 1 and 4 and is a collective motion of the hydroxyl stretches where nearest neighbors are out of phase. Eigenstates 2 and 3 show combinations of in phase and out of phase motion. The off-diagonal elements for the all-*anti* compound are in most cases zero indicating there is no collective motion of the hydroxyl stretches. The states are mostly vibrations of individual hydroxyl stretches. All hydroxyl stretching sites, however, contribute to the high energy as well as the low energy eigenstates corresponding to the case where the hydroxyl stretch is either free or hydrogen

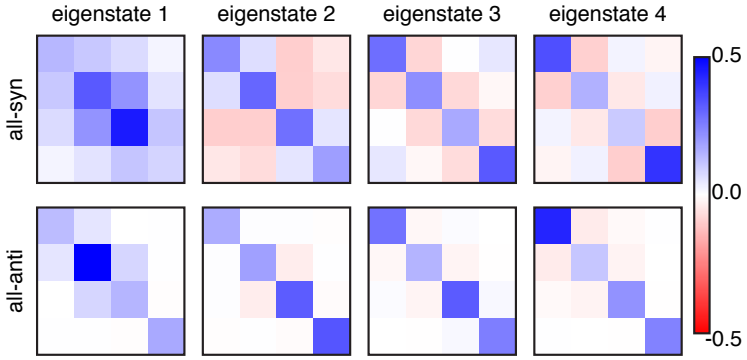

Figure 3.3.4: Density matrix elements of the instantaneous eigenstates in the first excitation manifold (1 is the lowest energy eigenstate and 4 the highest energy eigenstate) for the all-syn tetrol (top) and the all-anti tetrol (bottom) averaged over a trajectory of 200 ps.

bonded respectively [106]. As a measure for the delocalization of the eigenstate the inverse participation ratio [118] is shown in table 3.3.1 for the all-*syn* and all-*anti* compounds. The ratios for the eigenstates of the all-*anti* tetrol are very close to unity indeed, showing that the eigenstates are mainly localized on a single hydroxyl site. The ratios for the all-*syn* molecule are larger, indicating a delocalization over multiple hydroxyl stretches, as a "vibrational aggregate" [22].

eigenstate	all-*syn*	all-*anti*
1	1.49	1.13
2	1.67	1.17
3	1.48	1.14
4	1.21	1.07

Table 3.3.1: Inverse participation ratio of the different eigenstates in the first excitation manifold (1 is the lowest energy eigenstate and 4 the highest energy eigenstate) for the all-*syn* tetrol and all-*anti* tetrol averaged over a trajectory of 200 ps.

3.3.2 Two-dimensional spectra and population transfer

The experimental and simulated two-dimensional infrared spectra for the all-*syn* tetrol and all-*anti* tetrol are shown in Fig. 3.3.5. The simulated spectra are sampled over 1500 initial configurations of the quantum-classical system. In addition, an artificial lifetime of 1 ps was used during the times t_1 and t_3 mainly to smoothen the spectra [46]. The 2D-spectra show a diagonal peak (red) resulting from the ground state bleach and stimulated emission and a blue peak that results from the double excited state absorption which has a lower probe frequency due to the anharmonicity. These anharmonic peaks show different off-diagonal widths for the simulations and experiments for both compounds. In the simulations the anharmonicity was chosen as a constant and, therefore, independent of the electric fields along the hydroxyl stretches which results in too narrow peaks. In the experiment, besides, the anharmonic peak is perturbed by the linear absorption of the $\nu_1 + \nu_4$ combination band of the solvent which is not

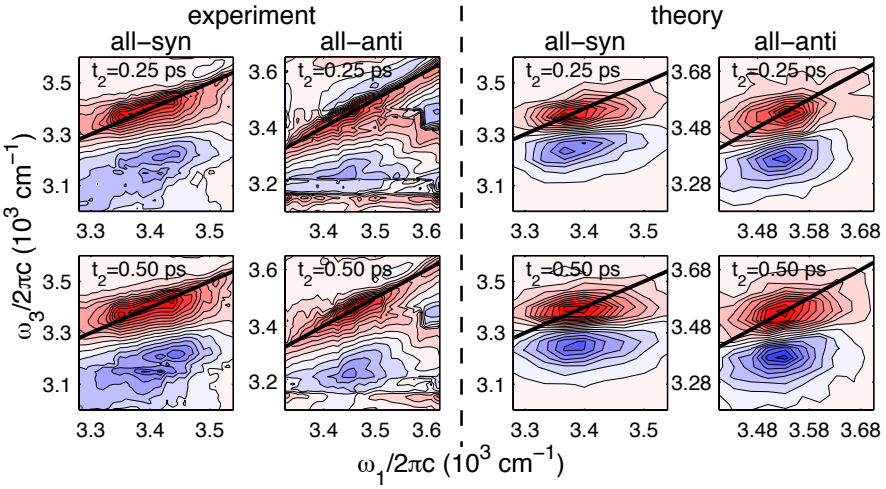

Figure 3.3.5: Experimental and simulated two-dimensional spectra for the all-*syn* and all-*anti* compounds for a waiting time of 0.25 ps (top) and 0.50 ps (bottom). Contour lines are displayed in increments of 10 % from -95 % till 95 % of the signal maximum. The experiments and simulations both show a faster spectral diffusion for the *all*-syn molecule than for the *all*-anti compound.

included in the simulation. We will, however, focus on the bleaching/emission spectral region for now.

The slope of the bleach/emission peak for the all-*syn* tetrol configuration at a waiting time of 0.25 ps is less steep than the almost diagonal all-*anti* peak. When the waiting time is increased to 0.5 ps, the slope of the peaks becomes smaller due to spectral diffusion for both compounds. The timescales for this homogeneous broadening are different, however, for the all-*syn* and all-*anti* tetrol. For both molecules, the calculated dynamics in the simulations is faster than in the experiment. The spectral diffusion timescale is very sensitive to the mapping and the point charges of the atoms (force field) used in the simulations, which where not specifically optimised for the studied compounds. The difference in timescale of the spectral diffusion between the *all*-syn molecule and the *all*-anti is, however, reproduced quite well by the simulations. Since the two molecules have different structures, the differences in homogeneous broadening might arise from the different timescales of the fluctuations of the site energies. In Fig. 3.3.6 the correlation functions of the site energies are plotted for the all-*syn* and all-*anti* tetrol molecule. The correlation time of the site energies of the all-*syn* is

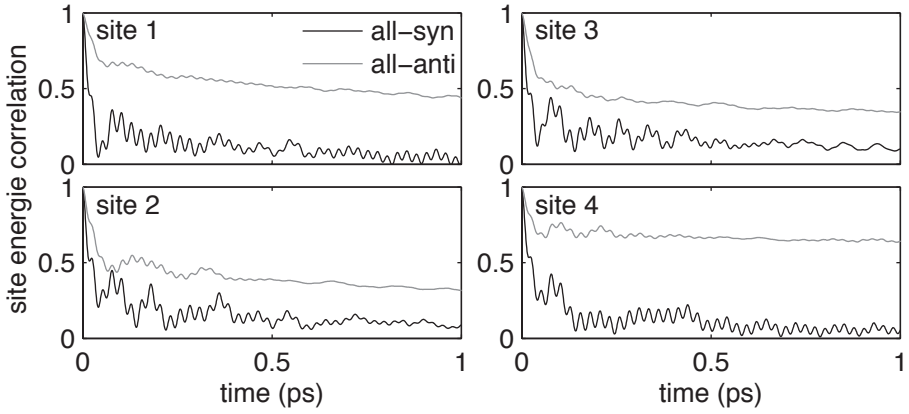

Figure 3.3.6: The normalized correlation functions of the site energies of the hydroxyl stretches for the all-*syn* (black lines) and all-*anti* (grey lines) tetrol molecule numbered as in Fig 3.1.1.

much shorter than for the all-*anti*. The hydroxyl groups for the all-*syn* molecule are strongly bonded, and the short timescale fluctuations in their bond length cause large site energy fluctuations. For the all-*anti* tetrol the correlation functions have a quickly decaying component corresponding to small fluctuations of the solvent and bond-lengths and a slow decaying component, which is caused by the intermittent breaking and making of hydrogen bonds along the trajectory as shown in Fig. 3.3.2. The different timescales for the homogeneous broadening for the all-*syn* and all-*anti* tetrols can thus be attributed to the differences in the correlation times of the site energies due to a stronger hydrogen bonding for the all-*syn* configuration. Furthermore, the correlation functions show oscillations (especially for the all-*syn* molecule) consisting with a low frequency and high frequency mode. The low frequency mode of these oscillations most probably corresponds to the librations of the hydroxyl groups and the high frequency mode to the bending of the COH-angle. For the all-*anti* molecule such modes are present as well, but have less influence on the site frequencies since the distances between sites are longer.

For longer waiting times (not shown here) the excited state absorption peak in the 2D-spectra will decay because of the relaxation of the excited state during the waiting time. It was shown in Refs. [107,108] that the excess in energy during this relaxation can cause the hydrogen bonds to break for the all-*syn* molecule causing the growth of a peak at higher frequencies. Our simulations only allows hopping within an excitation manifold and relaxation is not included. Therefore our model cannot completely reproduce the spectra for longer waiting times. The Hellmann-Feynmann forces resulting from the excitation in the system, as well as the energy dump, when a hop takes place do not show significant changes in the molecular structure like the breaking of a hydrogen bond in our simulations.

In Ref. [106] it was shown that the OH-stretching relaxation time for the all-*syn* compound is about 0.9 ps and is almost independent of the pump frequency. The relaxation time of the all-*anti* molecule has a strong dependence on the pump frequency ranging from 0.5 ps when the pump frequency 3360 cm^{-1} till 6 ps, when the pump frequency 3650 cm^{-1}. The relaxation time is determined by the energy gap between the excited mode and the accepting mode. It was argued that for the all-*syn* tetrol the narrow pump pulse excites a sub ensemble of the hydroxyl stretches. Due to the strong coupling this excitation would quickly delocalise over the molecule before the excitation relaxes and, therefore, lose the memory of the initially excited state. For the all-*anti* tetrol on the other hand,

it was argued that the excitation will reside on the hydroxyl stretch that was initially excited due to the weak coupling.

In Fig. 3.3.7 the population transfer is plotted for the all-*syn* and all-*anti* molecules. Initially one of the four sites is excited and the population is followed as a function of time. Here we used the Numerical Integration of Schrödinger Equation method (NISE) [46], where the quantum feedback is neglected, to calculate the population transfer. The surface hopping method as formulated in the previous chapter allows one to calculate the population transfer between eigenstates. However, for the case at hand this does not give a clear insight of the dynamics of the state initially excited since the nature of the eigenstates are different for different starting configurations over which is sampled. Therefore, we plotted the population transfer in the site basis here. For the all-*syn* compound the excitation can indeed quickly delocalise over the molecule due to the strong coupling. Besides the fast population transfer also the correlation times of the

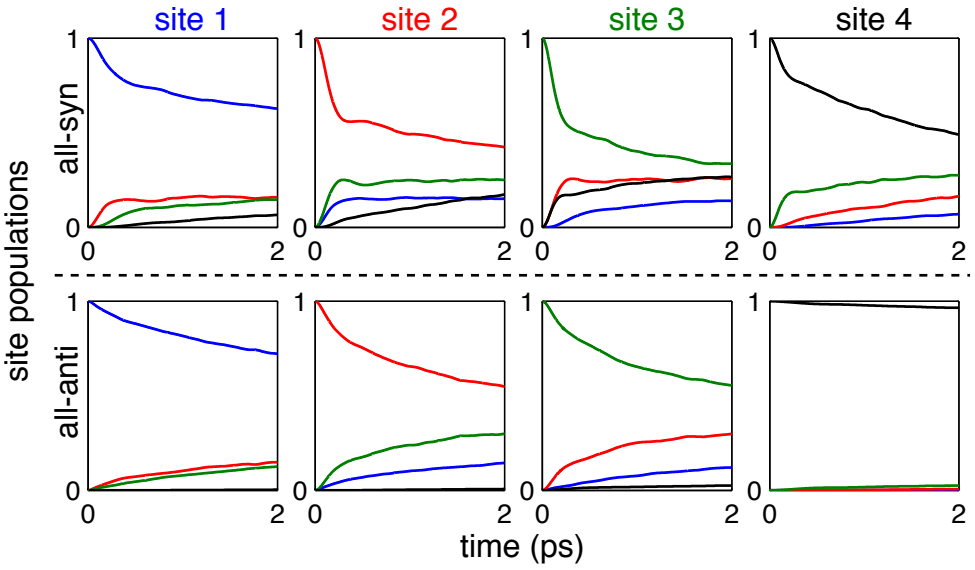

Figure 3.3.7: Population transfer in the site basis for the all-*syn* (top) and all-*anti* (bottom) configuration. At $t = 0$ the sites 1, 2, 3, and 4 (left to right) are excited and their average populations are plotted as a function of time.

site energies are short. The energy of the excitation for the all-*syn*, therefore, changes rapidly to the energy of the equilibrium state before relaxation takes place. The energy gap between this equilibrium state and the accepting mode determines the lifetime, making it largely independent of the pump frequency for the all-*syn* compound. For the all-*anti* molecule the population transfer is slower and the correlation times are longer as compared to the all-*syn* molecule. Even when the all-*anti* compound is excited at low frequencies, indicating strong hydrogen bonding, only the coupling between two sites is strong and the excitation cannot delocalise as quickly as for the all-*syn* compound. For the all-*anti* compound the memory of the initial excited state, therefore, is maintained and the energy gap between this state and the accepting mode determines the lifetime. From our simulations it can thus be concluded that the differences in coupling for both configurations and their differences in correlation times of the site energies may indeed give rise to the observed differences in the pump-dependence of the relaxation time. It should of course be noted that as we do not explicitly consider the accepting modes in our quantum hamiltonian the above considerations, which are in line with those of Ref. [106] rely on the assumption that the accepting modes are either nearby C-H stretching modes or OH-bend Fermi resonances located just below the OH-stretch band [119]. More elaborate simulations beyond the scope of the present chapter, including the accepting modes, would allow to verify this conclusion.

3.4 Conclusions

In this chapter we studied hydrogen bond dynamics in low-dimensional model system. We combined experiments and simulations to obtain and interpret the linear and 2DIR spectra of two diastereomeric polyalcohols. We found qualitative agreement between the measured spectra and simulations for both compounds. The polyalcohols have four hydroxyl groups that depending on the stereochemistry form a quasi-linear hydrogen bonded chain that is stable for tens of picoseconds (all-*syn*) or a system, where hydrogen bonds are broken and formed on a picosecond timescale (all-*anti*). For the all-*syn* tetrol the hydroxyl groups are strongly bonded to each other and the transition dipoles are almost perfectly aligned leading to a strong coupling as compared to the all-*anti* tetrol, where the transition dipoles are oriented more randomly. We showed that these differences in structure and dynamics explain the differences in the measured linear and

2DIR spectra of the two compounds.

For the linear spectra the weaker hydrogen bonding for the all-*anti* tetrol leads to a weaker absorption cross-section and a more intense peak at high frequency, corresponding to the non hydrogen bonded hydroxyl groups, as compared to the all-*syn* tetrol. The broadband peak which is associated to hydroxyl stretches that are hydrogen bonded is shifted to higher frequencies indicating that the hydrogen bonding is weaker in the all-*anti* molecule.

The 2DIR spectra of the two compounds show different timescales of the broadening of the bleaching/emission peak. This broadening is faster for the all-*syn* compound, where small fluctuations in the bond length and angles between neighboring hydroxyl groups cause fast fluctuations of the site energies. This causes the correlation function of the site energies to decay faster as compared to the all-*anti* compound, where the hydrogen bonding is weaker, and the dynamics of the local environment causes slower fluctuations of the site energies. In associated liquids, like liquid water, hydrogen bonding is even stronger and leads to an even faster spectral diffusion [95, 96].

Finally, we showed that the vibrational exciton coupling is mediated along the hydrogen-bonded chains, which is applicable in higher dimensional systems as well. The population transfer within the all-*syn* molecule is faster than for the all-*anti* one due to the stronger coupling between the different hydroxyl stretches. This explains the experimental observation that the lifetime of the OH-stretches is independent of the initial pump-frequency for the all-*syn* molecule, while for the all-*anti* molecule such a dependence is measured [106]. For the all-*syn* compound the memory of the pump-frequency is lost before relaxation occurs because of the fast population transfer and short correlation times of the site-energies. For the all-*anti* compound, on the other hand, the correlation times are longer, and the excitation remains in the initially excited state until relaxation occurs. In liquid water, the couplings between hydroxyl stretches are even stronger due to the stronger hydrogen bonding, and are responsible for the fast energy redistribution over the hydrogen bonded network and observed ultrafast relaxation [95].

3.5 Appendix

3.5.1 Theory

We simulate the optical response of the polyalcohols in a chloroform solvent using all-atomistic mixed quantum-classical simulations. We are interested in the OH-stretching region of the spectrum and, therefore, treat the stretching modes of the hydroxyl groups quantum mechanically and all other degrees of freedom classically. The two subsystems will be coupled to each other in a self-consistent way (conserving the total energy) using the fewest switches surface hopping algorithm [52, 72].

Classical subsystem

The system we consider consists of a box containing a single polyalcohol molecule (either all-*syn* or all-*anti*) and the solvent chloroform molecules. The simulations in this chapter contain a box of 500 chloroform molecules and 1 all-*syn* tetrol/all-*anti* tetrol molecule, respectively. A single polyalcohol molecule is sufficient since we are interested in the intramolecular hydrogen bonds and couplings. The concentrations used in the experiments are sufficiently low so that intermolecular bonds between different polyalcohols are negligible [106]. The state of the classical subsystem at a certain time is defined by the positions $\mathbf{R} = (r_1, r_2, ..., r_{3N})$ and velocities $\dot{\mathbf{R}} = (\dot{r}_1, \dot{r}_2, ..., \dot{r}_{3N})$ of all N atoms in our simulation box. The potential energy that a classical degree of freedom feels at a given time will depend on the positions of all other classical particles with respect to its own, as well as the state of the quantum subsystem to which it is coupled. The equation of motion for a single degree of freedom can be written as

$$m\ddot{r}_i = -\frac{dU(\mathbf{R})}{dr_i} - F_i^q(t), \tag{3.5.1}$$

where $U(\mathbf{R})$ is the potential energy resulting from the interaction with other classical particles and F^q is the force depending on the quantum state (quantum feedback), which is calculated using the surface hopping method as was explained in Sec. 2.2.2. The environment interacting with the quantum Hamiltonian is now, however, described in a fullly atomistic way and and the quantum forces are calculated for each atom separately according to Eq. 2.2.12. The interactions between classical particles is defined by a force field and are computed using the

GROMACS 4.5.5 distribution [110]. The OPLS force field is used for the bonded and Lennard-Jones forces [111, 112]. The charges used for the atoms of the polyalcohol molecules and chloroform solvent molecules are derived from similar functional groups of the OPLS force field and are given in the supplementary material. The three chloride atoms of each solvent molecule have an independent Drude particle associated with them to account for polarization effects giving an effective isotropic polarizability of 2.84333 Å^3 for each, to match the experimental value of 8.53 Å^3 [113]. The topology file for the tetrols are generated with the MKTOP program [114]. Bond distances are fixed with the LINCS algorithm [115]. For the calculation of the electrostatic potential the Particle Mesh Ewald method [120] is used with a cutoff radius of 1.5 nm. The classical coordinates are propagated by numerically integrating Eq. 3.5.1 using a leap frog integration scheme as implemented in GROMACS.

Quantum subsystem

We treat the stretching modes of the hydroxyl groups of the polyalcohol quantum mechanically and consider them as coupled three-level systems. The vibrational modes can be described using the Frenkel exciton Hamiltonian

$$\begin{aligned} H_{\mathrm{q}}(\mathbf{R}) &= \sum_i \omega_i(\mathbf{R}) B_i^\dagger B_i + \sum_{i \neq j} J_{ij}(\mathbf{R}) B_i^\dagger B_j - \sum_i \frac{\Delta_i}{2}(\mathbf{R}) B_i^\dagger B_i^\dagger B_i B_i \\ &\quad + \sum_i \vec{\mu}_i(\mathbf{R}) \cdot \vec{E}(t)(B_i^\dagger + B_i). \end{aligned} \tag{3.5.2}$$

Here $B_i^\dagger$ and B_i are the bosonic creation and annihilation operators for an excitation at site i with frequency ω_i. J_{ij} is the coupling between sites i and j, Δ_i is the anharmonicity of the third level, μ_i denotes the transition dipole moment and $\vec{E}$(t) is the electric field from the applied lasers. For simplicity, the laser fields are assumed to be infinitely short (delta function pulses). Note that relaxation back to the ground state is neglected in this Hamiltonian since the excitation can only change manifold if a laser field is applied. The transition frequencies, couplings, and transition dipoles of the OH-stretches depend on the state of the classical subsystem and, therefore, are time-dependent. We use the mapping of Skinner and coworkers [12] which was developed for OH-stretches in water to determine the quantum mechanical quantities of each site for a certain

classical state

$$\omega_i(\vec{E}_i^{\rm oh}) = 3762 + 5060|\vec{E}_i^{\rm oh}| - 86225|\vec{E}_i^{\rm oh}|^2 \quad [{\rm cm}^{-1}] \tag{3.5.3}$$

$$\vec{\mu}_i^{01}(\vec{E}_i^{\rm oh}) = 0.18749(0.7112 + 75.59)\vec{E}_i^{\rm oh} \quad [ea_0]. \tag{3.5.4}$$

Here ω_i is the transition frequency to the first excitation level, μ_i^{01} its transition dipole and $\vec{E}_i^{\rm oh}$ is the electric field at the hydrogen atom, along the hydroxyl stretch in atomic units (e/a_0^2). This electric field is calculated by summing over the electric fields generated by each charged classical particle in our simulation box, except for the oxygen and hydrogen atom that form the stretch considered. For simplicity we neglect the electric field dependence of the anharmonicity and use the vacuum value of 147.5 cm^{-1} [12]. The transition dipole from the first excited state to the double excited state (1-2 transition) is assumed to be $\vec{\mu}_i^{12} = \sqrt{2}\vec{\mu}_i^{01}$, which holds for harmonic oscillators. To calculate the coupling between the hydroxyl stretches at sites i and j, we use the dipole-dipole approximation

$$J_{ij} = \left[\frac{\vec{\mu}_i \cdot \vec{\mu}_j}{|\vec{r}_{ij}|^3} - \frac{(\vec{r}_{ij} \cdot \vec{\mu}_i)(\vec{r}_{ij} \cdot \vec{\mu}_j)}{|\vec{r}_{ij}|^5}\right]. \tag{3.5.5}$$

Here $\vec{r}_{ij}$ is the vector connecting the hydrogen atoms of the hydroxyl stretches i and j. This mapping provides the Hamiltonian of the quantum subsystem for each configuration of the classical system. The time-dependence of the quantum state $\Phi(t)$ is described by the time-dependent Schrödinger equation

$$i\hbar\frac{d\Phi(t)}{dt} = H_{\rm q}(t)\Phi(t). \tag{3.5.6}$$

We propagate the quantum state with a small time step Δt by numerical integration assuming that during this time step the time-dependent Hamiltonian is constant, so that

$$\Phi(t + \Delta t) = e^{-\frac{i}{\hbar}H_q(t)\Delta t}\Phi(t). \tag{3.5.7}$$

The matrix exponent is calculated by diagonalizing the Hamiltonian.

3.6 Charges used in the simulations

The all-*syn* tetrol, all-*anti* tetrol, and deuterated chloroform molecules of the simulations are shown in Fig. 3.6.1. Atoms or groups that have the same charges are labelled identically. The charges for the tetrols are given in Table 3.6.1, and for the chloroform in Table 3.6.2.

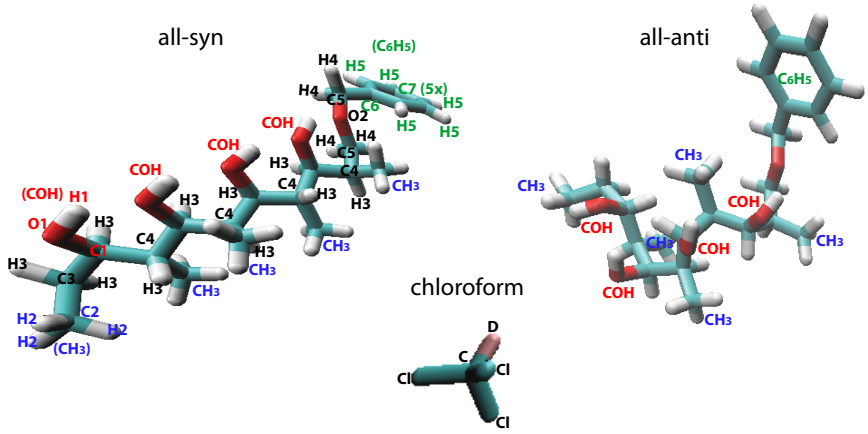

Figure 3.6.1: Schematic overview of the all-*syn* tetrol (left), all-*anti* tetrol (right) and deuterated chloroform (bottom) molecules. Identical atoms that have the same charge have the same label. The charges for the poly-alcohols are given in Table 3.6.1 and for the chloroform in Table 3.6.2. The two poly-alcohol molecules have a different stereochemistry, but their atoms have the same charges in the simulations. The atoms are divided into four groups (COH (red), CH3 (blue), Backbone (black), C6H5 (green)). The three chloride atoms in the deuterated chloroform molecule have a Drude particle associated with them, to include polarization effects.

Atom	Charge
COH-groups	
C1	0.205
O1	-0.590
H1	0.325
CH_3-groups	
C2	-0.180
H2	0.060
Backbone	
C3	-0.120
H3	0.060
C4	-0.060
C5	0.140
H4	0.030
O2	-0.400
C_6H_5-groups	
C6	0.000
C7	-0.115
H5	0.115

Table 3.6.1: Charges for the atoms of the all-*syn* and all-*anti* tetrol in atomic units. The atoms are numbered as in Fig. 3.6.1.

Atom	Charge
C	0.010
D	0.140
Cl	-3.050
Drude Cl	3

Table 3.6.2: Charges for the atoms of the deuterated chloroform solvent molecules in atomic units.

Chapter 4

Atomistic modelling of 2D-spectra for Light Harvesting 2

The Light Harvesting 2 (LH2) complex is a vital part of the photosystem of purple bacteria. It is responsible for the absorption of light and transport of the resulting excitations to the reaction center in a highly efficient manner. In order to understand this highly efficient energy transport a general description of the chromophores and the interaction with their local environment is crucial. Here, we include this interaction in a fully atomistic way using mixed quantum-classical(molecular dynamics) simulations of spectra. In particular, we present the first fully atomistic simulation of non-linear optical spectra for LH2 and use it to study the energy transport within the complex. We show that the frequency distributions of the pigments strongly depend on their positions with respect to the protein scaffold and dynamics of their local environment. Furthermore, we show that although the pigments are closely packed, the transition frequencies of neighboring pigments are essentially uncorrelated. We present the simulated linear absorption spectra for the LH2 complex and provide a detailed explanation of the states responsible for the observed two-band structure. Finally, we discuss the energy transfer within the complex by analysing population transfer calculations and two-dimensional spectra for different waiting times. We conclude that the energy transfer from the B800 ring to the B850 ring is mediated by intermediate states that are delocalised over both rings, allowing for a stepwise downhill energy transport.

This chapter is based on C. P. van der Vegte, J. D. Prajapati, U. Kleinekathöfer, J. Knoester, T. L. C. Jansen J. Phys. Chem. B, **119**, 1302 (2015)

4.1 Introduction

The photosystem of purple bacteria is very efficient in turning sunlight into chemical energy [5]. This energy conversion occurs in the reaction center (RC), where the charge separation takes place. To enhance the absorption cross section of the photosystem, the RC is surrounded by antenna complexes Light Harvesting 1 (LH1) and Light Harvesting 2 (LH2) [3,4]. These antenna systems are responsible for the absorption of light and the transfer of the excitation to the RC. For efficient light harvesting it is crucial that this energy transfer is fast so that the excitation reaches the RC before relaxation occurs. In order to understand this highly efficient energy transport a general description of the pigments and the interaction with their local environment is essential. Here, we present a mixed quantum-classical simulation method for calculating (non-)linear spectra where the interaction between the pigments and their environment is included in a fully atomistic way. We apply the method to study energy transfer within a single LH2 complex and show that the nature of states within the complex allows for a fast downhill energy transfer.

There are many species of LH2 complexes, which structure depend on the growth conditions, amongst other things. From high-resolution studies the structure of three species, that can be crystallised, are known in great detail [121–123]. These complexes are composed of pigments mounted on proteins and it is the electrostatic interactions between the pigments that mediates the energy transfer. The LH2 complexes comprise either eight or nine identical transmembrane protein structures leading to an eight- [123] or nine-fold [122] symmetry, depending on the species of purple bacteria. In Fig. 4.1.1 a schematic picture is shown for the LH2 complex of *Rhodospirillum molischianum* which has an eight-fold symmetry. Each of the transmembrane protein binds three optically active bacteriochlorophyll a (BChla) molecules and one or two carotenoids. In this study we focus on the optical response of the BChla pigments. They form two concentric rings which are often referred to as the B850 ring and B800 ring, due to their absorption bands around 850 nm and 800 nm at room temperature [125].

The study of LH2 complexes greatly intensified both experimentally and theoretically after the high resolution structure was determined for some species [121–123]. Low temperature fluorescence spectroscopy experiments allow to study single LH2 complexes and reveal the dense electronic structure which in ensemble studies is washed away due to disorder [126–131]. Energy transfer within

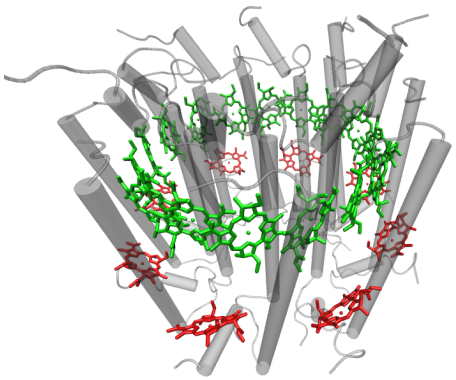

Figure 4.1.1: Schematic overview of the LH2 complex of *Rhodospirillum molischianum*. The BChla chromophores form two concentric rings mounted on the protein scaffold. The B850 ring colored in green contains twice as many chromophores as the B800 ring shown in red. The figure was rendered using VMD [124].

the complex has been studied using two-dimensional electronic spectroscopy (2DES) experiments [2, 132] on ensembles of LH2 complexes [27, 133, 134]. In such experiments three ultrafast laser pulses are applied to the system with respective time delays t_1 and t_2, during which the system is in a coherence and population, respectively. A radiated signal is measured at a time t_3 after the third laser pulse, using a reference pulse. By Fourier transforming over the time delays t_1 and t_3 a correlation spectrum as a function of ω_1 and ω_3, respectively, is obtained for a chosen waiting time t_2. Such 2D-correlation spectra are sensitive to both population transfer and structural dynamics that occur during the waiting time [2, 135]. The energy transfer between two states, for example, is comprised in the 2D-spectra through the growth of a cross peak at the location where ω_1 is equal to the energy of the initial state and ω_3 equal to the energy of the state to which the energy is transferred. By studying the growth of such cross peaks, as a function of the waiting time, detailed information on the energy transfer within the system is obtained. The 2D-spectra are complicated to understand, however,

due the complex nature of the excited states and overlapping peaks. In the 2D-spectra of antenna complexes like the Fenna-Matthews-Olson (FMO) complex and LH2, for example, oscillations that remain for hundreds of femtoseconds have been observed [23, 27, 136, 137]. It has been argued that the oscillations originate from quantum coherences between excitonic states, protected from dephasing by the protein environment, and that the coherent transport between these states is responsible for the efficient energy transfer [23, 27, 138]. Although coherent transport may indeed be responsible for the observed oscillations, it has also been proposed that these oscillations arise from underdamped vibrational modes of the environment [28, 29]. To interpret the 2D-spectra and disentangle between such effects, theoretical models and simulations that include a detailed description of the pigments and the interaction with their local environment are crucially needed. So far, theoretical models and simulations have been used to calculate the absorption spectra [139–141], fluorescence spectra [127, 142], population transfer [140, 141, 143–150] and more recently 2D-spectra for zero waiting times [151] for LH2. The interaction between the chromophores and their environment in these models is often included in a simplified stochastic way, where the used parameters are fitted to experimental data.

In this study we describe the interaction between the pigments and their environment in a fully atomistic way using classical molecular dynamics simulations. The pigment protein complex is embedded in a lipid bilayer membrane surrounded by water. The electronic excitations of the BChla pigments are described quantum mechanically and the parameters for the transition frequencies, transition dipoles and couplings are determined by the positions of all classical atoms in the simulation box. Previously, similar mixed quantum-classical simulations of linear spectra and spectral densities have been performed for light harvesting complexes using semi-empirical electronic structure calculations to determine the transition frequencies [36, 41–44]. Such quantum-chemical calculations are, however, computationally demanding and, therefore, extremely expensive for calculations of 2D-spectra [36]. Within this study we use the much cheaper charge density coupling method [10, 11, 139, 152] to determine the transition frequencies. We calculate the linear spectra, energy transfer in the LH2 complex, and present the first 2D-spectra for LH2, simulated using a fully atomistic description of the environment. Within our simulations the quantum and classical subsystems are coupled to each other in a self-consistent way using the surface hopping method [52, 72, 153]. This method accounts for the Stokes shift

and leads to a Boltzmann distribution within the quantum system in equilibrium, which is crucial when dealing with electronic systems where the energy separation between states is comparable to, or larger than k_BT [52, 72, 153]. Semi-empirical electronic structure calculations usually assume a ground state trajectory for the classical system and are unable to describe these effects. The method presented can readily be applied to other light harvesting systems like LH1, photosystem II and FMO.

The remainder of this chapter is outlined as follows. In the Method section we briefly describe the simulation setup and the method for calculating the (non-)linear spectra using the surface hopping method. In the Results section we present the distribution functions of the transition frequencies, transition dipoles and couplings within the system. In addition, we show that the protein induced correlations between transition frequencies of neighboring pigments are insignificant for LH2 and cannot be used to explain the beating signals observed in the 2D-spectra. Furthermore, we present the simulated linear spectra and analyze the nature of the states that are responsible for the absorption in the B800 and B850 bands. Finally, we show our results for the energy transfer and 2D-spectra calculations on LH2. We demonstrate that energy transfer can rapidly occur from the B800 band to the B850 band due to the highly delocalized nature of the electronic states.

4.2 Method

We calculate the (non-)linear optical response of the LH2 complex using fully atomistic mixed quantum-classical molecular dynamics simulations. The quantum and classical subsystem are coupled to each other in a self-consistent way using the surface hopping method [52, 72, 153] as was described in Sec. 2.2. The molecular dynamics simulation box consists of 114011 atoms and is identical to the one used and described in Ref. [41]. The simulation box contains a single *Rs. molishianum* LH2 complex arranged according to the crystal structure [123]. The pigment-protein complex is embedded in a *1-palmitoyl-2-oleoyl-sn-glycero-3-phosphocholine* (POPC) lipid bilayer surrounded by about 30 $\AA$ of water molecules on both sides. We are interested in the spectral region of the Q_y transition of the BChla pigments and, therefore, treat their electronic excitation quantum mechanically and all other degrees of freedom classically. The excited states of the carotenoids are not included in the quantum subsystem

since their transitions are much higher in energy than the Q_y transitions [141] of the BChla pigments and, therefore, do not play a role in the energy transport between the B800 and B850 ring. Due to the Coulomb interactions the presence of the carotenoids, however, does influence the directions and magnitudes of the transition dipoles of the BChla pigments and, therefore, the couplings between them [141, 154].

The twenty-four BChla chromophores are considered as coupled two-level quantum systems and are described by the Frenkel exciton Hamiltonian (Eq. 2.2.2). The transition frequencies, transition dipoles and excitonic couplings depend on the positions of all the atoms in the simulation box (chromophores themselves and their environment). We use the charge density coupling method [10,11,139,152] to calculate the transition frequencies of the chromophores, which is a first order perturbation theory in the intermolecular Coulomb interaction. The transition frequency of a chromophore i in this approach is given by

$$\omega_i = \omega_0 + \frac{1}{\epsilon} \sum_{k=1}^{N_i} \sum_{l=1}^{N_{env}} \frac{\Delta q_{ik}^{eg} q_l}{|\vec{r}_{ik} - \vec{r}_l|}. \tag{4.2.1}$$

Here ω_0 is the transition frequency of the chromophore in the absence of an environment and is equal for all the twenty-four chemically identical BChla pigments. It's value is chosen to be 10900 cm^{-1} to match the overall position of the spectra compared to experimental data. The second term describes the influence of the environment on the pigment's transition frequency. This term is the difference between the Coulomb interaction energy with the environment, when the pigment is in the ground- and the excited state. Δq_{ik}^{eg} denotes the charge difference of the chromophores kth atom between the excited- and ground state. We use the values reported in Ref. [10] calculated at the TDDFT/B3LYP/6-31G* level of theory. The partial charges of the chromophores in the ground state in our simulation are, however, determined by the force field [155] and are different from the ones calculated in Ref. [10]. For each atom, k, of the chromophore, i, the difference in Coulomb interaction energy is calculated by summing over all the contributions of the N_{env} charged atoms in the simulation box. Screening effects of the local environment on the transition frequencies can be included via the effective dielectric constant ϵ [152,156]. We use the transition charge electrostatic potential (TrEsp) method [10,157] to calculate the transition dipoles of the chromophores and the excitonic couplings between them for a configuration of the simulation box. In this method the transition densities of the chromophores

are represented by partial transition charges located at the atoms that form the chromophore and are provided by Ref. [10] as well. The transition dipole of a chromophore i is given by

$$\vec{\mu_i} = \sum_{k=1}^{N_i} q_{ik}(1,0)\vec{r}_{ik}, \tag{4.2.2}$$

where the sum is over all atomic partial transition charges $q_{ik}(1,0)$ of the pigment with coordinates $\vec{r}_{ik}$. In the TrEsp method the excitonic coupling between two chromophores i and j is obtained by the electrostatic interaction between their transition charges

$$J_{ij} = \frac{1}{\epsilon}\sum_{k=1}^{N_i}\sum_{l=1}^{N_j}\frac{q_{ik}(1,0)q_{jk}(1,0)}{|\vec{r}_{ik} - \vec{r}_{jl}|}. \tag{4.2.3}$$

The absolute values of the transition charges are typically rescaled to match an observable [10]. Previously, the transition charges were rescaled with a factor in the range 0.63-0.75 to match the vacuum transition dipole moment of 6.1 Debye of the BChla chromophores [10]. A rescaling factor of 0.81 has also been used to match the expected excitonic couplings between nearest neighbor pigments in the B850 ring of around 250-300 cm^{-1} [139]. Here we rescale the couplings by a factor of 0.7 to reproduce the energy splitting between the two bands observed in the linear spectrum. Polarisation effects on the couplings between pigments can be included via the dielectric constant ϵ, which is system dependent. Several distance dependent functions have been proposed as well as functions, which depend on the relative orientation of the chromophores [158]. Hsu *et al.* [159] showed that the couplings between two chromophores when embedded in a medium with a dielectric constant of $\epsilon = 2$ can differ between 80 and 110 % of the coupling between them in a vacuum, depending on their relative orientation. The coupling strengths directly influence the excitonic splittings, determining the peak positions to which we matched the transition charges already. Therefore, we use a constant value for the dielectric constant of $\epsilon = 1$ like was done in Refs. [10,139].

In the Frenkel exciton Hamiltonian the pigments are described as coupled two-level systems, neglecting the intra-molecular vibrations as in a previous study they were found to give a negligible contribution to the spectral density of BChla [160]. These vibrational modes can be included using the Holstein Hamiltonian for the coupling to the dominant modes, like was done in Ref. [30], or by

including them in the spectral density using semi-empirical electronic structure calculations [36, 41]. This, however, significantly increases the computational cost for calculating the non-linear spectra.

The state of the classical subsystem is defined by the positions and velocities of all the 114011 atoms in the simulation box. The potential energy surface a classical atom feels is determined by the positions of all the other atoms in the simulation box and the state of the quantum system. The forces between atoms are computed using the Gromacs 4.5.5 distribution [110] and are determined by the force field. The CHARMM27 force field [161, 162] is employed for the lipids, proteins and water molecules (TIP3P potential [163]) and the parameters used for the BChla pigments and lycopenes can be found in Ref. [155]. The electrostatic potential is calculated with the Particle Mesh Ewald method and the bond distances are fixed using the LINCS algorithm [115]. The v-rescale thermostat [164] with a temperature of 310 K was used. When the BChla pigments are in an excited state (population), the surface hopping method as described in Refs. [72, 153] is used to include the change in potential energy of the classical degrees of freedom, due to the excitation.

The time-dependence of the state of the quantum subsystem is described by the time-dependent Schrödinger equation and the equation of motion of the classical degrees of freedom are Newtonian like. The equations of motion for the quantum and classical subsystem are coupled since the classical degrees of freedom influence the Hamiltonian and, vice versa, the quantum state influences the forces on the classical atoms. The classical and quantum subsystem are, therefore, numerically integrated in an in turn fashion as is depicted in Fig. 2.2.2. We propagate the quantum subsystem using a scheme based on the Trotter formula [60], using a time step of 1 fs, assuming that the Hamiltonian is constant during this time step (classical degrees of freedom do not move much). The propagated quantum state is then used to calculate the forces on the classical degrees of freedom which are then propagated a single time step using the Velocity Verlet method [110, 165], after which the quantum state is propagated again. The spectra are obtained by summing over the different Liouville pathways contributing to the linear response and third-order response, for the linear spectra and 2D-spectra, respectively, and Fourier transforming. For the third-order response there are six pathways contributing to the signal (Fig. 2.2.3), which are the rephasing and non-rephasing parts of the groundstate bleach (GB), stimulated emission (SE) and excited state absorption (EA) diagrams [7, 53]. The state of

the quantum subsystem is different for the different pathways and, therefore, the diagrams have different classical trajectories along propagation. The quantum system during the waiting time, for example, is in the groundstate for the GB diagram whereas in a coherence between two single excited states for the SE and EA diagrams, leading to different quantum feedback forces on the classical subsystem. More details on the propagation of the mixed quantum-classical system and the calculation of the linear and 2D-spectra using the surface hopping method can be found in Refs. [72, 153]. The spectra are averaged over multiple starting configurations of the simulation box which are extracted from a ground state molecular dynamics trajectory, separated by 1 ps. We average the (non-)linear spectra over the orientational coefficients for an isotropic sample to include the polarization dependence of the laser pulses in the laboratory frame on the optical response [7,166]. Moreover, the third-order response functions are multiplied with a windowing function of the form

$$\mathcal{R}(t_1, t_2, t_3) = \mathcal{R}(t_1, t_2, t_3) 0.5^{(t_1+t_3)^2/T^2}, \tag{4.2.4}$$

to smoothen the 2D-spectra. A value of $T = 0.3$ ps is used.

4.3 Results

4.3.1 Site Energies, Couplings and Correlations

In Fig. 4.3.1 the site energy distributions of the chromophores and the averages of the most important couplings are shown for a trajectory of 2.25 ns for which the Hamiltonian was calculated at every time step of 1 fs. We fitted these distribution functions to a Gaussian function and the parameters for the fit are given in Table 4.3.1. The pigments forming the B850 ring (labelled BChla α and

BChla	$\bar{\omega}$ (cm^{-1})	σ (cm^{-1})
α	12050	135
β	11970	135
γ	12370	265

Table 4.3.1: Fit parameters for Gaussian functions perfectly matching the chromophores site energy distributions in Fig. 4.3.1.

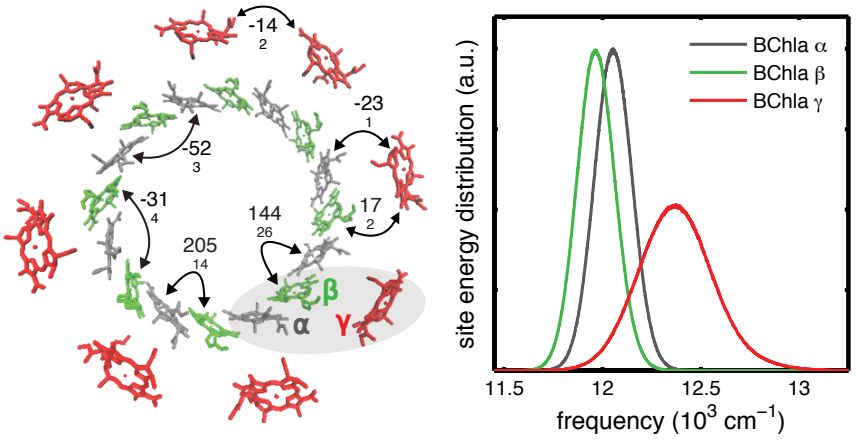

Figure 4.3.1: Left: Schematic overview of the LH2 complex. The chromophores of a single trimer unit are labelled as α, β and γ. The average coupling constants of the strongest interactions between the chromophores are given (large font) and their standard deviations (small font) in wave numbers. The couplings are averaged over a 2.25 ns trajectory and over identical pairs due to the eight fold symmetry of the system. Right: Site energy distributions for the BChla chromophores (α, β and γ) of the LH2 for the same trajectory. The distributions have been averaged over by symmetry identical chromophores.

BChla β) and the B800 pigments (labelled BChla γ) have different average transition frequencies. These differences in frequency shifts arise from the different electrostatic interaction with the local environment of the chromophores. The transition energies of the BChla α and BChla β chromophores forming the B850 ring are on average splitted by 80 cm^{-1}, which is due to their different positions with respect to the protein scaffold. The size of their fluctuations is identical however. The B800 pigments on average have a higher transition frequency of 360 cm^{-1} than the B850 chromophores. This splitting mainly results due to their different binding pockets, which for the B800 pigments are hydrophilic whereas hydrophobic for the B850 pigments [123, 139]. The distribution of the $B800$ pigments is about twice as broad which is attributed to the more polar environment

surrounding the B800 ring [41].

The site energy distributions calculated by Olbrich *et al.* [41] using semi-empirical electronic structure calculations with an identical simulation box result in a much smaller splitting between the B800 and B850 pigments of about 40 cm^{-1} only. For the calculation of the linear spectra, Olbrich *et al.* shifted the B800 pigment frequencies by an additional 355 cm^{-1}, however, to match the observed splitting between the two bands. In Ref. [139] the charge density coupling method was applied to a static LH2 setup using the structural data in the Protein Data Bank (1NKZ [167]), where the lipids and solution are absent. This yielded a splitting between the site energies of the B800 and B850 pigments in the range 234-334 cm^{-1}, depending on the protonation state, which is similar to the 360 cm^{-1} obtained by us. On the other hand, the method of Ref. [139] gave a splitting between the BChla α and β pigments in the range 360-372 cm^{-1}, which is much larger than the 80 cm^{-1} obtained here. This discrepancy might result from the electrostatic interaction of the pigments with the lipids that surround the protein scaffold and BChla rings, which are included in the present study but are absent in the PDB file. However, in the fitting/modelling of circular dichroism spectra a splitting between the BChla α and β pigments of about 300 cm^{-1} has previously been assumed [168,169], which is larger than the splitting we obtain based on the structural information.

The chromophores in the B850 ring are closely packed and, therefore, are strongly coupled. The B850 pigments form a dimerized aggregate, where the nearest neighbor distance between BChla α and BChla β pigments within a single dimer unit is smaller than the distance between chromophores of adjacent dimer units. Due to this distance differences and the relative orientation of the transition dipoles, the nearest average neighbor coupling between pigments within such a dimer unit (215 cm^{-1}) is stronger than the average coupling between nearest neighbor pigments of adjacent dimers (150 cm^{-1}). The average couplings between nearest B800 pigments are much weaker (14 cm^{-1}) due to their larger separation. The strongest couplings between the B800 and B850 ring are 17 and -23 cm^{-1} between the B800 pigments and nearest BChla α / BChla β pigments, respectively. These couplings are weak due to the separation between the pigments as well as the relative orientation between the B800 pigments and the B850 pigments. From spectroscopic studies the strongest couplings within the B850 ring are estimated to be around 250-300 cm^{-1} which is slightly higher than the couplings we obtain. The strength of the obtained couplings within the

used coupling map are proportional to the square of the rescaling factor used for the transition charges, which we optimized to obtain the right peak-peak separation in the linear spectra. The width of the distributions of the couplings are small as indicated by the standard deviations in Fig. 4.3.1. The fluctuations of the couplings arise due to the slight variation of the distances between chromophores. Furthermore, the transition dipoles of the chromophores vary in direction and strength due to the movement of individual units that form the chromophores, with respect to each other. The distributions of the transition dipole strengths of the chromophores are shown in Fig. 4.3.2.

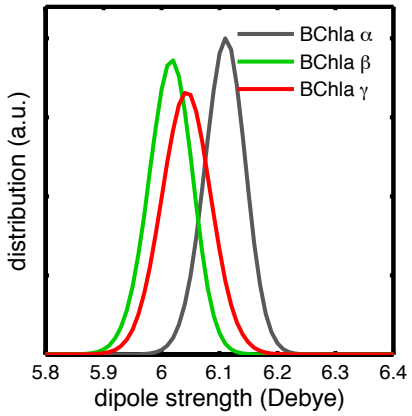

Figure 4.3.2: Distributions of the transition dipole strengths of the BChla α, β and γ pigments for a trajectory of 2.25 ns.

For LH2 beating signals have been observed in the 2D-spectra which have been interpreted as long-lived electronic coherences [27]. The chromophores in the LH2 complex are closely packed and share a similar environment which might cause a strong correlation between the fluctuations of their transition frequencies. Such a correlation can enhance energy transfer and has been used to explain the long lived coherences observed in photosynthetic systems [23, 40]. To see whether the site energy fluctuations are correlated for LH2, and thereby preserve electronic coherences, we calculate the spatial cross correlation functions

between the site energies of the pigments defined as

$$C_{ij} = \frac{1}{\sqrt{\sigma_i^2 \sigma_j^2}} \langle (\omega_i - \bar{\omega}_i)(\omega_j - \bar{\omega}_j) \rangle. \tag{4.3.1}$$

Here $\langle .. \rangle$ denotes the average over the trajectory, $\bar{\omega}_i$ the average transition frequency of chromophore i, and σ_i the standard deviation of the fluctuations. In Fig. 4.3.3 the cross correlation coefficients are shown for all pairs of the 24 pigments. On the diagonal the correlation is by definition equal to unity. We find a small correlation between the site energies of nearest neighbor BChla α and BChla β pigments within the dimer units in the B850 ring. The correlation coefficient averaged over the eight by symmetry identical pairs (within the dimer units) is 0.17 with a standard deviation of 0.07. Other correlations coefficients are even smaller and negligible compared to the remaining noise. We, therefore, conclude that cross correlations are insignificant for the LH2 complex. This agrees with to what was previously reported by Olbrich *et al.* [41], although there, a much shorter trajectory of 12 ps was used. For this short trajectory it

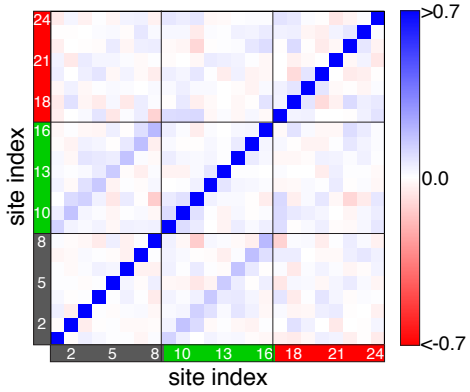

Figure 4.3.3: Spatial cross correlation functions between site frequencies of the 24 pigments averaged over a trajectory of 2.25 ns. The site indexes 1-8, 9-16, and 17-24 indicate the BChla α, β and γ pigments, respectively.

is hard to distinguish the correlation coefficients from the noise, which is evident from the different correlation coefficients found in Ref. [41] for the by symmetry identical pairs.

4.3.2 Linear Spectra and Eigenstate Analysis

In Fig. 4.3.4 the simulated linear spectrum is shown together with the measured spectrum [125]. The average energies of the eigenstates are indicated by the bars whose heights corresponds to the absorption cross section of the states. The coherence time t_1 is included in the range of 0 till 0.5 ps to obtain the first-order response functions. The response functions are, furthermore, averaged over 1500 starting configurations of the simulation box. The simulated absorption spectrum reproduces the observed two-peak structure and the splitting between the two bands indeed matches the experimental data. The low energy band

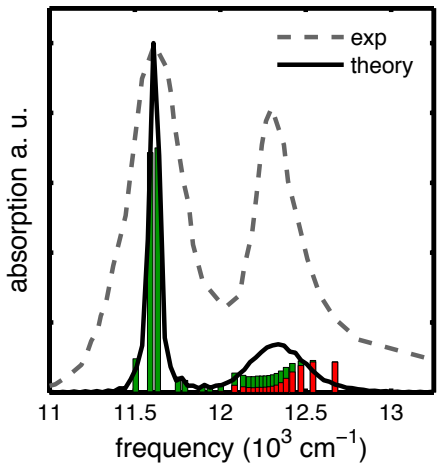

Figure 4.3.4: Observed (dashed line) and calculated (solid line) absorption spectra for LH2. The calculated spectra is sampled over 1500 different starting configurations, extracted from a ground state trajectory of 1.5 ns. The bars indicate the average energy of the eigenstates and the height indicates their average transition dipole strengths squared. The green and red colors of the bars show the participation of inner and outer ring chromophores to the eigenstate, respectively.

results from the absorption of multiple states but the main contribution comes from two nearly degenerate superradiant states also known as the $k = \pm 1$ states [126]. The lowest energy $k = 0$ eigenstate has a significant transition dipole moment and recently has been observed in single molecule fluorescence spectra [170]. According to our simulations it is redshifted from the $k \pm 1$ states by about 110 cm^{-1}. For a circular structure without disorder the transition dipole moment of the $k = 0$ is expected to be small, since it only results from the out of plane components of the transition dipoles of the pigments. Due to the disorder in the system, however, the $k = 0$ state gains significant oscillator strength from nearby states [127]. The states within the low energy band are all completely localized on the B850 ring and, therefore, also referred to as the B850 states. The lower energy part of the high energy band results from the absorption of multiple states with rather weak transition dipole moments. These states are delocalized over both the B850 and B800 ring (B850* states). The high energy absorption within the high energy band results from the absorption of states mainly localized on the B800 ring (B800 states). A measure for the spatial delocalization of these excitonic eigenstates is the coherence length. Several definitions exist for the coherence length [171, 172] and we use the following [173, 174]

$$L_\rho = \frac{(\sum_{ij}^{N} |\rho_{ij}|)^2}{N \sum_{ij}^{N} |\rho_{ij}|^2}, \tag{4.3.2}$$

where ρ is the density matrix corresponding to an eigenstate in the site basis, and N is the number of chromophores. For a perfectly coherent state all elements of the density matrix have an absolute value equal to 1/N leading to a coherence length of $L_\rho = N$. When a state is localised on a single pigment, however, only the single diagonal element of the density matrix corresponding to that site has nonzero value of 1, leading to a coherence length of $L_\rho = 1/N$. We plotted the coherence length obtained for the 24 eigenstates in the first excitation manifold in Fig. 4.3.5, averaged over a groundstate trajectory of 2.25 ns. The states in the low energy band are highly delocalized over about half the inner ring. In Refs. [147,172] similar coherence lengths where obtained in model studies of LH2. Such a strong delocalization of the states in a way enhances the energy transfer in the system, since these states make the complex robust against the trapping of an excitation. The B850* states are slightly delocalised over a couple of B800 and B850 pigments. The high frequency B800 states are essentially localized at single outer ring chromophores.

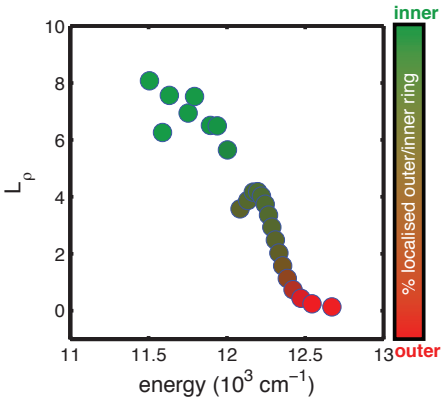

Figure 4.3.5: Coherence length for the eigenstates in the first excited state manifold as a function of their energy. The coherence lengths are averaged over a trajectory of 2.25 ns for which the hamiltonian was calculated at every timestep of 1 fs. The colors indicate how much the eigenstate is localized on the inner ring (green color) and outer ring (red color) averaged over the whole trajectory.

The simulated result for the absorption spectrum has a low energy band that is much narrower than the one observed in the experiment. The experimental spectra are measured for an ensemble of LH2 complexes whereas in the simulations only a single LH2 complex is considered. Within the 2.25 ns trajectory we are able to catch the fast nuclear fluctuations, but not the slow structural changes of the complex (static disorder). Furthermore, the C8 symmetry structure of the LH2 complex within our simulation is based on x-ray crystallography experiments where the LH2 complexes are extremely densely packed. This C8 symmetry leads to nearly degenerate $k = \pm 1$ states, regardless of diagonal disorder. From low-temperature fluorescence spectroscopy measurements on single LH2 complexes, a large splitting between the two superradiant states is, however, observed [126]. This splitting can only be explained by a structural deformation (disorder in the couplings) of the protein complex, like a two-fold symmetrical elliptical structure [126, 142, 175]. The structure of the LH2 complexes, thus, depends on the environment surrounding the LH2 complexes (density of the samples) and it cannot be excluded that the structure of LH2 in purple bacteria

differs from the one in crystals.

In order to theoretically describe/fit different experimental observables for LH2, static disorder in the transition frequencies [142, 176, 177] and in the couplings [126, 127, 168, 177–179] have been commonly added. The B850 band is narrow in our simulations due to exchange narrowing and, therefore, is rather insensitive to diagonal disorder. The band, however, is sensitive to correlated off-diagonal disorder. Here we decide to maintain the circular structure, based on the x-ray data, and include static off-diagonal disorder in the following *ad hoc* way. Instead of using a constant rescaling factor of 0.7 for the transition charges for calculating the couplings (Eq. 3), the rescaling factor for a single sample is determined by drawing a random number from a normal distribution with a mean of 0.7 and a standard deviation of 0.15. The C8 symmetry of the complex is maintained in this way since all couplings within a single sample are rescaled with the same factor. We, therefore, effectively sample over LH2 complexes with different radii, like was done in Ref. [179]. Within the simulation there are 5 POPC lipids surrounded by the protein scaffold. One could imagine that one more or less POPC lipid could slightly change the radius of the pigment-protein complex which changes the distance between the pigments and thereby the couplings.

The simulated linear spectrum including the off-diagonal disorder is shown in Fig. 4.3.6. The B850 band has become much broader than before, and matches the experimental data much better. A sample with a larger rescaling factor gives rise to a narrow B850 band at a lower energy than a sample with a smaller rescaling factor. It is the average of all the separate contributions of the different samples that leads to the broadening of the B850 band. The B800 band is hardly affected by the rescaling due to the localized nature of the excitations. Although the inclusion of static off-diagonal disorder gives rise to a significant improvement of the linear spectrum, the widths of the bands and their relative intensities still do not perfectly match the experiment. The simulations strongly depend on the mappings used for the transition frequencies, couplings, and transition dipoles. Moreover, the force field used to describe the atomistic environment determines the positions of the atoms in the simulation box and, therefore, all the above quantities. Optimisations of the mappings and force fields will lead to improved simulated spectra. Here we used the approximate charge density coupling method to determine the transition frequencies, which is computationally cheap compared to semi-empirical structure calculations. This allows for

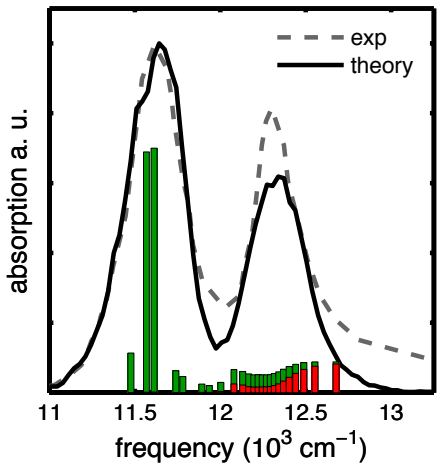

Figure 4.3.6: Observed (dashed line) and calculated (solid line) absorption spectra for LH2. The calculated spectrum is sampled over 1500 starting configurations including static off-diagonal disorder for the couplings. The bars indicate the average energy of the eigenstates and the height indicates their average absorption intensity. The green and red colors of the bars show how much on average the state is localised on the inner and outer ring, respectively.

rather long trajectories needed for the calculation of 2D-spectra. Furthermore, the utilisation of such a mapping allows for the computation of the derivatives of the excited state potential, which are needed to determine the influence of the quantum state on the environment.

4.3.3 2D-spectra and Energy Transfer

In Fig. 4.3.7 the simulated all-parallel polarization two-dimensional spectra are shown for a waiting time of $t_2 = 0$ and $t_2 = 250$ fs. The simulations included the static off-diagonal disorder and the coherence times t_1 and t_3 were varied from 0 till 0.2 ps. The zero waiting time 2D-spectra shows two diagonal peaks corresponding to the B850 and B800 bands. The B850 band has much more intensity than the B800 band. It was shown above that the B850 band mainly results from the absorption of two superradiant states with strong transition dipole mo-

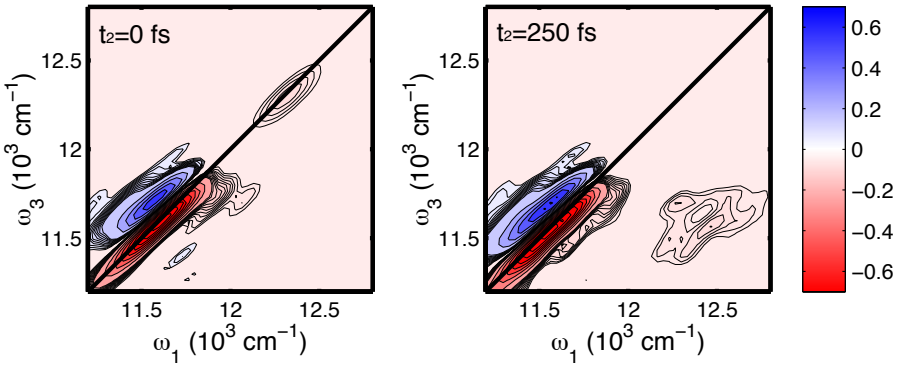

Figure 4.3.7: Simulated two-dimensional spectra of the LH2 complex for a waiting time of 0 fs and 250 fs for an all-parallel polarization setup. The spectra for $t_2 = 0$ fs and $t_2 = 250$ fs have been sampled over 1500 and 150 initial configurations of the simulation box, respectively.

ments whereas the B800 band results from the absorption of many states with rather weak transition dipoles. Since the 2D-spectra depend on the transition dipole to the fourth power, the B850 band is much more pronounced than the B800 band. The negative valued peaks along the diagonal in the 2D-spectra result from the stimulated emission and ground state bleach contributions. At the low energy band there is a high intensity positive peak above the diagonal resulting from the excited state absorption. The splitting between these two peaks is about 150 cm^{-1} and the excited state absorption peak has 64% of the intensity of the ground state bleach/stimulated emission peak. A similar peak structure has been observed in 2D-spectra of J-aggregates and this feature is a typical indication of a strong delocalization of the states [34, 180]. For the B800 band such a positive peak is not visible in the 2D-spectra since the molecules are weakly coupled leading to states that are localized on a few molecules, so that the excited state absorption contributions are cancelled by the stimulated emission and ground state bleach signals. The 2D-spectra measured for short waiting times in Ref. [133] for an LH2 complex of the species *Rhodobacter sphaeroides* (nine-fold symmetry) show qualitatively similar peak structures; however, a di-

rect comparison is not suitable because of the different species and, furthermore, the experimental pulse shape, which was not included in the simulations.

The 2D-spectrum for a waiting time of 250 fs in Fig. 4.3.7 shows the growth of a substantial cross peak below the diagonal indicating energy transfer from the B800 band to the B850 band. The diagonal B800 peak is no longer visible due to this relaxation and the weak transition dipole moments in the B800 band. The measured 2D-spectra by Fidler et al. [133] show the growth of such a cross-peak as well on a hundreds of femtosecond timescales. Furthermore, the low energy band in the measured spectra for non-zero waiting times exhibits a Stokes shift of about 110 cm^{-1} [133]. This Stokes shift can arise from the strong interaction between the quantum excitation and the bath, which can cause a dynamic localization of the excitation [134, 181–183]. Such a Stokes shift and exciton localization is, however, not observed in our simulations where the reorganization of the environment due to the excitation is included using the surface hopping method [52, 72, 153]. Since the states within the B850 band are delocalized over multiple chromophores, the additional forces are spread out over a large area and the reorganization of the environment, therefore, is small. Based on this observation, we think that the experimental Stokes shift results from intraband relaxation within the B850 band instead. According to fluorescence experiments on LH2 the energy splitting between the two superradiant states within the B850 band is about 110 cm^{-1} [126], which is similar to the observed Stokes shift. Although relaxation of the excitation is included in our simulations, such a splitting between the $k \pm 1$ states is absent due to the inherent C8 symmetry of the LH2 complex crystal structure, as was described above. Furthermore, the simulations presented here neglect the intra-molecular vibrations of the pigments, which can affect the excited state dynamics and can cause a peak shifted from the diagonal in the 2D-spectra as well. Recently, the influence of such vibronic couplings on the electronic coherences measured in the 2D-spectra have been studied extensively [28, 30], although it has been demonstrated that the contribution of intra-molecular vibrations to the spectral density are negligible for BChla [160]. Their inclusion in our fully atomistic simulations, interesting as it may be, at this moment is computationally too costly.

To study the energy transfer from the high-energy band to the low-energy band in a more elaborate way we calculate the population transfer diagrams depicted in Fig. 4.3.8. The twenty-four eigenstates in the first excitation manifold are labelled 1-24 (from low to high energies) and are divided into three groups.

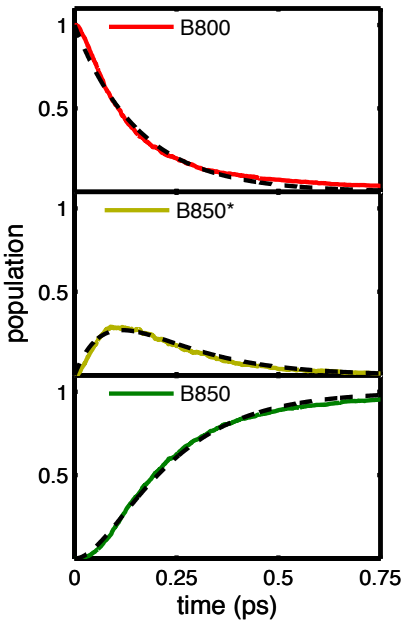

Figure 4.3.8: Average population of the B850 (bottom), B850* (middle) and B800 (top) states as a function of time after initial excitation of the highest energy eigenstate in the first excitation manifold calculated using the surface hopping method. The data is averaged over 1500 starting configurations of the simulation box. The dashed lines indicate the fits of the data to a kinetic model.

The eight eigenstates lowest in energy form the B850 band and are labeled as the B850 states. The eigenstates 9-16 absorb in the low energy part of the B800 band, but are strongly localized on the inner (B850) ring and, therefore, are labelled as the B850* states. The eight eigenstates highest in energy are labelled as the B800 states. Initially the highest energy eigenstate (24) was excited and the probability for finding the excitation in each subset of eigenstates is shown as a function of time in Fig. 4.3.8. It is clear that the excitation first relaxes within the B800 band from the B800 states to the lower energy B850* states. The excitation is then already partially localized on the inner ring and from there can transfer to the B850 band. The presence of the intermediate B850* states

thus allows for a stepwise downhill energy transfer from the B800 band to the B850 band. In Refs. [148, 149] Redfield theory was applied to an LH2 complex at a temperature of 77 K and a similar relaxation pathway was found albeit with slower relaxation times due to the lower temperature [184].

In order to extract the timescales for the intra-band B800→B850* and the inter-band B850*→B850 energy transfer we fitted the population transfer data to the following simple kinetic model:

$$\begin{aligned} \frac{dN_{800}(t)}{dt} &= -\lambda_1 N_{800}(t) \\ \frac{dN_{850^*(t)}}{dt} &= -\lambda_2 N_{850^*}(t) + \lambda_1 N_{800}(t) \\ \frac{dN_{850(t)}}{dt} &= \lambda_2 N_{850^*}(t), \end{aligned} \tag{4.3.3}$$

excluding direct relaxation from the B800 states to the B850 states. The dashed lines in Fig. 4.3.8 show the results of the kinetic model fit which almost perfectly correspond to the original data. The obtained timescales for the relaxation constants are $\lambda_1 = 6.35$ 1/ps and $\lambda_2 = 11.18$ 1/ps. Within our simulations the relaxation process from the B800 band to the B850 band is completed after 0.75 ps. This corresponds to the observed inter-band relaxation timescale of 0.7 ps observed in transient absorption experiments on the LH2 complex of *Rhodobacter sphaeroides* [184, 185]. From the growth of the B800→B850 cross peak in the 2D-spectra of the LH2 complex of *Rhodobacter sphaeroides* a timescale of 0.7 ps was determined as well. Furthermore the 2D-spectra where reported to be indistinguishable for waiting times from 1 ps onward, indicating the system has completely relaxed in the first excitation manifold within 1 ps, which is similar to our observations.

4.4 Conclusion

In this chapter, we calculated (non-)linear spectra of LH2 using mixed quantum-classical simulations and studied energy transport within the complex using the surface hopping method. The simulation method includes the interaction of the chromophores and their environment in a fully atomistic way using molecular dynamics simulations and, therefore, provides detailed information on the influence of the surroundings on the transition frequencies, transition dipoles and energy

transport in the system. For a groundstate molecular dynamics trajectory we showed that the chromophores positions and binding pockets strongly influence their average transition frequencies and the size of the fluctuations. Although the chromophores are closely packed, we showed that the site energies of neighboring pigments are practically uncorrelated and, therefore, conclude that such correlations cannot be used to explain the long-lived beating signals observed in the 2D-spectra [27].

We simulated the linear absorption spectra for the LH2 complex and were able to reproduce the two band structure. Additional off-diagonal disorder by averaging over LH2 complexes with different radii was added to broaden the B850 band, resulting in a good match in the peak distance and peak width. We showed that this low-energy band results from the absorption of states that are highly delocalized over multiple B850 pigments. Due to the strong coupling in the B850 ring, the inner ring pigments, however, also contribute to the high energy band. These B850* states have non-zero transition dipole moments and are delocalized over multiple B850 and B800 pigments. Furthermore, we showed that the high-energy part of the B800 band mainly results from the absorption of single B800 pigments.

Finally, we presented the first fully atomistic mixed quantum-classical simulations of 2D-spectra for the LH2 complex. The simulations show qualitative agreement with experimental data on LH2 complexes of the species *Rhodospirillum acidophila* with a nine-fold symmetry [133]. The substantial growth of a cross peak on a timescale of hundreds of femtoseconds below the diagonal indicates rapid energy transfer from the B800 band to the B850 band. We showed that the nature of the states in the complex allows for a stepwise downhill energy transfer. Upon excitation of the B800 states, first an intra-band relaxation occurs to the B850* states, after which the excitation can transfer to the low-energy band.

Bibliography

[1] R. E. Fenna and B. W. Matthews, "Chlorophyll Arrangement in a Bacteriochlorophyll Protein from Chlorobium Limicola," *Nature*, vol. 258, p. 573, 1975.

[2] T. Brixner, J. Stenger, H. M. Vaswani, M. Cho, R. E. Blankenship, and G. R. Fleming, "Two-Dimensional Spectroscopy of Electronic Couplings in Photosynthesis," *Nature*, vol. 434, p. 625, 2005.

[3] K. Miller, "Three-Dimensional Structure of a Photosynthetic Membrane," *Nature*, vol. 300, pp. 53–55, 1982.

[4] X. Hu, T. Ritz, A. Damjanović, F. Autenrieth, and K. Schulten, "Photosynthetic Apparatus of Purple Bacteria," *Q. Rev. Biophys.*, vol. 35, pp. 1–62, 2002.

[5] H. v. Amerongen, L. Valkunas, and R. v. Grondelle, *Photosynthetic Excitons*. World Scientific, 2000.

[6] P. Hamm, M. H. Lim, and R. M. Hochstrasser, "Structure of the Amide I Band of Peptides Measured by Femtosecond Nonlinear-Infrared Spectroscopy," *J. Phys. Chem. B*, vol. 102, p. 6123, 1998.

[7] P. Hamm and M. T. Zanni, *Concepts and Methods of 2D Infrared Spectroscopy*. Cambridge: Cambridge University Press, 2011.

[8] J. D. Hybl, A. W. Albrecht, S. M. Gallagher Faeder, and D. M. Jonas, "Two-Dimensional Electronic Spectroscopy," *Chem. Phys. Lett.*, vol. 297, no. 307-313, 1998.

[9] S. T. Roberts, J. J. Loparo, and A. Tokmakoff, "Characterization of Spectral Diffusion from Two-Diemnsional Line Shapes," *J. Chem. Phys.*, vol. 125, p. 084502, 2006.

[10] M. E. Madjet, A. Abdurahman, and T. Renger, "Intermolecular Coulomb Couplings from Ab Initio Electrostatic Potentials: Application to Optical Transitions of Strongly Coupled Pigments in Photosynthetic Antennae and Reaction Centers," *J. Phys. Chem. B*, vol. 110, pp. 17268–17281, 2006.

[11] T. Renger, M. E. Madjet, M. Schmidt am Busch, J. Adolphs, and F. Müh, "Structure-Based Modeling of Energy Transfer in Photosynthesis," *Photosynth. Res.*, vol. 116, pp. 367–388, 2013.

[12] B. M. Auer and J. L. Skinner, "IR and Raman Spectra of Liquid Water: Theory and Interpretation," *J. Chem. Phys.*, vol. 128, p. 224511, 2008.

[13] J. Stark, "Beobachtungen über Den Effekt Des Elektrischen Feldes Auf Spektrallinien I. Quereffekt," *Ann. d. Physik*, vol. 43, p. 965, 1914.

[14] K. Lazonder, M. S. Pshenichnikov, and D. A. Wiersma, "Easy Interpretation of Optical Two-Dimensional Correlation Spectra," *Optics Lett.*, vol. 31, no. 22, pp. 3354–3356, 2006.

[15] J. B. Asbury, T. Steinel, C. Stromberg, K. J. Gaffney, I. R. Piletic, and M. D. Fayer, "Hydrogen Bond Breaking Probed with Multidimensional Stimulated Vibrational Echo Correlation Spectroscopy," *J. Chem. Phys.*, vol. 119, p. 12981, 2003.

[16] S. Woutersen, Y. Mu, G. Stock, and P. Hamm, "Hydrogen-Bond Lifetime Measured by Time-Resolved 2D-IR Spectroscopy: N-Methylacetamide in Methanol," *Chem. Phys.*, vol. 266, p. 137, 2001.

[17] Y. S. Kim and R. M. Hochstrasser, "Chemical Exchange 2D IR of Hydrogen-Bond Making and Breaking," *P. Nat. Acad. Sci.*, vol. 102, p. 11185, 2005.

[18] T. L. C. Jansen and J. Knoester, "Calculation of Two-Dimensional Infrared Spectra of Ultrafast Chemical Exchange with Numerical Langevin Simulations," *J. Chem. Phys.*, vol. 127, p. 234502, 2007.

[19] E. H. G. Backus, P. H. Nguyen, V. Botan, R. Pfister, A. Moretto, M. Crisma, C. Toniolo, G. Stock, and P. Hamm, "Energy Transport in Peptide Helices: A Comparison Between High- and Low-Energy Excitations," *J. Phys. Chem. B*, vol. 112, p. 9091, 2008.

[20] S. Woutersen and P. Hamm, "Time-Resolved Two-Dimensional Vibrational Spectroscopy of a Short Alpha-Helix in Water," *J. Chem. Phys.*, vol. 115, p. 7737, 2001.

[21] T. L. C. Jansen and J. Knoester, "Two-Dimensional Infrared Population Transfer Spectroscopy for Enhancing Structural Markers of Proteins," *Biophys. J.*, vol. 94, pp. 1818–1825, 2008.

[22] J. T. King, C. R. Baiz, and K. J. Kubarych, "Solvent-Dependent Spectral Diffusion in Hydrogen Bonded "Vibrational Aggregate"," *J. Phys. Chem. A*, vol. 114, pp. 10590–10604, 2010.

[23] G. S. Engel, T. R. Calhoun, E. L. Read, T. K. Ahn, T. Mancal, Y. C. Cheng, R. E. Blankenship, and G. R. Fleming, "Evidence for Wavelike Energy Transfer Through Quantum Coherence in Photosynthetic Systems," *Nature*, vol. 446, p. 782, 2007.

[24] G. D. Scholes, G. R. Fleming, A. Olaya-Castro, and R. van Grondelle, "Lessons from Nature About Solar Light Harvesting," *Nature Chem.*, vol. 3, pp. 763–774, 2011.

[25] A. Goj and E. R. Bittner, "Mixed Quantum Classical Simulations of Excitons in Peptide Helices," *J. Chem. Phys.*, vol. 134, p. 205103, 2011.

[26] J. Lessing, S. Roy, M. Reppert, M. D. Baer, D. Marx, T. l. C. Jansen, J. Knoester, and A. Tokmakoff, "Identifying Residual Structure in Intrinsically Disordered Systems: A 2D IR Spectroscopic Study of the GVGXPGVG Peptide.," *J. Am. Chem. Soc.*, vol. 134, pp. 5032–5035, 2012.

[27] E. Harel and G. S. Engel, "Quantum Coherence Reveals Complex Dynamics in Bacterial Light-Harvesting Complex 2 (LH2)," *P. Nat. Acad. Sci.*, vol. 109, pp. 706–711, 2012.

[28] N. Christensson, H. F. Kauffmann, T. Pullerits, and T. Mančal, "Origin of Long-Lived Coherences in Light-Harvesting Complexes," *J. Phys. Chem. B*, vol. 116, pp. 7449–7454, 2012.

[29] A. W. Chin, J. Prior, R. Rosenbach, F. Caycedo-Soler, S. F. Huelga, and M. B. Plenio, "The Role of Non-Equilibrium Vibrational Structures in Electronic Coherence and Re-Coherence in Pigment-Protein Complexes," *Nature Phys.*, vol. 9, pp. 113–118, 2013.

[30] A. Halpin, P. J. M. Johnson, R. Tempelaar, R. S. Murphy, J. Knoester, T. L. C. Jansen, and R. J. D. Miller, "Two-Dimensional Spectroscopy of a Molecular Dimer Unveils the Effects of Vibronic Coupling on Exciton Coherences," *Nature Chem.*, vol. 6, pp. 196–201, 2014.

[31] A. G. Redfield, "the Theory of Relaxation Processes," *Adv. Magn. Reson.*, vol. 1, p. 1, 1965.

[32] P. Kjellberg, B. Brüggeman, and T. Pullerits, "Two-Dimensional Electronic Spectroscopy of an Excitonically Coupled Dimer," *Phys. Rev. B*, vol. 74, p. 024303, 2006.

[33] Q. Shi, L. Chen, G. Nan, R. Xu, and Y. Yan, "Electron Transfer Dynamics: Zusman Equation Versus Exact Theory," *J. Chem. Phys.*, vol. 130, p. 164518, 2009.

[34] A. G. Dijkstra, T. L. C. Jansen, and J. Knoester, "Localization and Coherent Dynamics of Excitons in the Two-Dimensional Optical Spectrum of Molecular J-Aggregates ," *J. Chem. Phys.*, vol. 128, p. 164511, 2008.

[35] Y. Tanimura and R. Kubo, "Time Evolution of a Quantum System in Contact with a Nearly Gaussian-Markoffian Noise Bath," *J. Phys. Soc. Jp.*, vol. 58, p. 101, 1988.

[36] C. Olbrich, T. L. C. Jansen, J. Liebers, M. Aghtar, J. Strümpfer, K. Schulten, J. Knoester, and U. Kleinekathöfer, "from Atomistic Modeling to Excitation Transfer and Two-Dimensional Spectra of the FMO Light-Harvesting Complex," *J. Phys. Chem. B*, vol. 115, pp. 8609–8621, 2011.

[37] C. J. Fecko, J. D. Eaves, J. J. Loparo, A. Tokmakoff, and P. L. Geissler, "Ultrafast Hydrogen-Bond Dynamics in the Infrared Spectroscopy of Water," *Science*, vol. 301, p. 1698, 2003.

[38] T. L. C. Jansen, D. Cringus, and M. S. Pshenichnikov, "Dissimilar Dynamics of Coupled Water Vibrations," *J. Phys. Chem. A*, vol. 113, p. 6260, 2009.

[39] S. Roy, M. S. Pshenichnikov, and T. L. C. Jansen, "Analysis of 2D CS Spectra for Systems with Non-Gaussian Dynamics," *J. Phys. Chem. B*, vol. 115, pp. 5431–5440, 2011.

[40] H. Lee, Y. C. Cheng, and G. R. Fleming, "Coherence Dynamics in Photosynthesis: Protein Protection of Excitinic Coherence," *Science*, vol. 316, pp. 1462–1465, 2007.

[41] C. Olbrich and U. Kleinekathöfer, "Time-Dependent Atomistic View on the Electronic Relaxation in Light-Harvesting System II," *J. Phys. Chem. B*, vol. 114, pp. 12427–12437, 2010.

[42] Y. Jing, R. Zheng, H. X. Li, and Q. Shi, "Theoretical Study of the Electronic-Vibrational Coupling in the Q_y States of the Photosynthetic Reaction Center in Purple Bacteria," *J. Phys. Chem. B*, vol. 116, pp. 1164–1171, 2011.

[43] L. Zhang, D. A. Silva, H. Zhang, A. Yue, Y. Yan, and X. Huang, "Dynamic Protein Conformations Preferentially Drive Energy Transfer Along the Active Chain of the Photosystem II Reaction Centre," *Nat. Comm.*, vol. 5, p. 4170, 2014.

[44] S. Valleau, A. Eisfeld, and A. Aspuru-Guzik, "On the Alternatives for Bath Correlators and Spectral Densities from Mixed Quantum-Classical Simulations," *J. Chem. Phys.*, vol. 137, p. 224103, 2012.

[45] T. L. C. Jansen and J. Knoester, "Nonadiabatic Effects in the Two-Dimensional Infrared Spectra of Peptides: Alanine Dipeptide," *J. Phys. Chem. B*, vol. 110, p. 22910, 2006.

[46] T. L. C. Jansen and J. Knoester, "Waiting Time Dynamics in Two-Dimensional Infrared Spectroscopy," *Acc. Chem. Res.*, vol. 42, no. 9, pp. 1405–1411, 2009.

[47] H. Torii, "Effects of Intermolecular Vibrational Coupling and Liquid Dynamics on the Polarized Raman and Two-Dimensional Infrared Spectral Profiles of Liquid N,N-Dimethylformamide Analysed with a Time-Domain Computational Method," *J. Phys. Chem. A*, vol. 110, p. 4822, 2006.

[48] J. R. Schmidt, S. A. Corcelli, and J. L. Skinner, "Pronounced Non-Condon Effects in the Ultrafast Infrared Spectroscopy of Water," *J. Chem. Phys.*, vol. 123, p. 044513, 2005.

[49] V. May and O. Kühn, *Charge and Energy Transfer Dynamics in Molecular Systems*. Berlin: Wiley-VCH, 2000.

[50] G. D. Billing, *the Quantum Classical Theory*. New York: Oxford University Press, 2003.

[51] J. C. Tully, "Molecular Dynamics with Electronic Transitions," *J. Chem. Phys.*, vol. 93, pp. 1061–1071, 1990.

[52] S. Hammes-Schiffer and J. C. Tully, "Proton Transfer in Solution: Molecular Dynamics with Quantum Transitions," *J. Chem. Phys.*, vol. 101, p. 4657, 1994.

[53] S. Mukamel, *Principles of Nonlinear Optical Spectroscopy*. New York: Oxford University Press, 1995.

[54] P. L. McRobbie, G. Hanna, Q. Shi, and E. Geva, "Signatures of Nonequilibrium Solvation Dynamics on Multidimensional Spectra," *Acc. Chem. Res.*, vol. 42, pp. 1299–1309, 2009.

[55] A. Ghosh, J. Qiu, W. F. DeGrado, and R. M. Hochstrasser, "Tidal Surge in the M2 Proton Channel Sensed by 2D IR Spectroscopy," *P. Nat. Acad. Sci.*, vol. 108, pp. 6115–6120, 2011.

[56] O. F. Mohammed, D. Pines, J. Dreyer, E. Pines, and E. T. J. Nibbering, "Sequential Proton Transfer Through Water Bridges in Acid-Base Reactions," *Science*, vol. 310, p. 83, 2005.

[57] B. J. Siwick, M. J. Cox, and H. J. Bakker, "Long-Range Proton Transfer in Aqueous Acid-Base Reactions," *J. Phys. Chem. B*, vol. 112, p. 378, 2008.

[58] J. B. Asbury, T. Steinel, and M. D. Fayer, "Hydrogen Bond Networks: Structure and Evolution After Hydrogen Bond Breaking," *J. Phys. Chem. B*, vol. 108, no. 21, pp. 6544–6554, 2004.

[59] T. Yagasaki and S. Saito, "Ultrafast Intermolecular Dynamics of Liquid Water: A Theoretical Study on Two-Dimensional Infrared Spectroscopy," *J. Chem. Phys.*, vol. 128, p. 154521, 2008.

[60] C. Liang and T. L. C. Jansen, "An Efficient N^3-Scaling Propagation Scheme for Simulating Two-Dimensional Infrared and Visible Spectra," *J. Chem. Theory Comput.*, 2012.

[61] Q. Shi and E. Geva, "A Comparison Between Different Semiclassical Approximations for Optical Response Functions in Nonpolar Liquid Solution. II. the Signature of Excited State Dynamics on Two-Dimensional Spectra," *J. Chem. Phys.*, vol. 129, p. 124505, 2008.

[62] P. L. McRobbie and E. Geva, "A Benchmark Study of Different Methods for Calculating One- and Two-Dimensional Optical Spectra," *J. Phys. Chem. A*, vol. 113, p. 10425, 2009.

[63] G. Hanna and E. Geva, "Multidimensional Spectra Via the Mixed Quantum-Classical Liouville Method: Signatures of Nonequilibrium Dynamics," *J. Phys. Chem. B*, vol. 113, p. 9278, 2009.

[64] K. Kwac and E. Geva, "Mixed Quantum-Classical Molecular Dynamics Study of the Hydroxyl Stretch in Methanol/Carbon- Tetrachloride Mixtures II: Excited State Hydrogen Bonding Structure and Dynamics, Infrared Emission Spectrum, and Excited State Lifetime," *J. Phys. Chem. B*, vol. 116, p. 2856, 2012.

[65] A. Ishizaki and Y. Tanimura, "Dynamics of a Multimode System Coupled to Multiple Heat Baths Probed by Two-Dimensional Infrared Spectroscopy," *J. Phys. Chem. A*, vol. 111, p. 9269, 2007.

[66] C. Kreisbeck, T. Kramer, M. Rodriguez, and B. Hein, "High-Performance Solution of Hierarchical Equations of Motion for Studying Energy Transfer in Light-Harvesting Complexes," *J. Chem. Theory Comput.*, vol. 7, pp. 2166–2174, 2011.

[67] L. Chen, R. Zheng, Q. Shi, and Y. Yan, "Two-Dimensional Electronic Spectra from the Hierarchical Equations of Motion Method: Application to Model Dimers," *J. Chem. Phys.*, vol. 132, 2010.

[68] B. Palmieri, D. Abramavicius, and S. Mukamel, "Lindblad Equations for Strongly Coupled Populations and Coherences in Photosyntetic Complexes," *J. Chem. Phys.*, vol. 130, p. 204512, 2009.

[69] A. Bastida, C. Cruz, J. Zuniga, A. Requena, and D. Miguel, "A Modified Ehrenfest Method That Achieves Boltzmann Quantum State Populations," *Chem. Phys. Lett.*, vol. 417, pp. 53–57, 2006.

[70] P. V. Parandekar and J. C. Tully, "Detailed Balance in Ehrenfest Mixed Quantum-Classical Dynamics," *J. Chem. Theo. Comp.*, vol. 2, pp. 229–235, 2006.

[71] P. Ehrenfest, "Bemerkung über Die Angenäherte-Gültigkeit Der Klassischen Mechanik Innerhalb Der Quantenmechanik," *Z. Phys.*, vol. 45, pp. 455–457, 1927.

[72] R. Tempelaar, C. P. v. d. Vegte, J. Knoester, and T. L. C. Jansen, "Surface Hopping Modeling of Two-Dimensional Spectra," *J. Chem. Phys.*, vol. 138, p. 164106, 2013.

[73] A. S. Petit and J. E. Subotnik, "How to Calculate Linear Absoprtion Spectra with Lifetime Broadening Using Fewest Switches Surface Hopping Trajectories: A Simple Generalization of Ground-State Kubo Theory," *J. Chem. Phys.*, vol. 141, p. 014107, 2014.

[74] M. Khalil, N. Demirdoven, and A. Tokmakoff, "Coherent 2D IR Spectroscopy: Molecular Structure and Dynamics in Solution," *J. Phys. Chem. A*, vol. 107, no. 27, pp. 5258–5279, 2003.

[75] A. Ishizaki and G. R. Fleming, "Unified Treatment of Quantum Coherent and Incoherent Hopping Dynamics in Electronic Energy Transfer: Reduced Hierarchy Equation Approach," *J. Chem. Phys.*, vol. 130, no. 23, p. 234111, 2009.

[76] J.-J. Ding, J. Xu, J. Hu, R.-X. Xu, and Y. Yan, "Optimized Hierarchical Equations of Motion Theory for Drude Dissipation and Efficient Implementation to Nonlinear Spectroscopies," *J. Chem. Phys.*, vol. 135, p. 164107, 2011.

[77] J. Strümpfer and S. K., "Open Quantum Dynamics Calculations with the Hierarchy Equations of Motion on Parallel Computers," *J. Chem. Theory Comput.*, vol. 8, pp. 2808–2816, 2012.

[78] G. C. Pimentel and C. H. Sederholm, "Correlation of Infrared Stretching Frequencies and Hydrogen Bond Distances in Crystals," *J. Chem. Phys.*, vol. 24, p. 639, 1956.

[79] L. Stryer, J. L. Tymoczko, and J. M. Berg, *Biochemistry.* New York: Freeman, fifth ed., 2002.

[80] N. Agmon, "The Grotthuss Mechanism," *Chem. Phys. Lett.*, vol. 244, pp. 456–462, 1995.

[81] K. J. Tielrooij, R. L. A. Timmer, H. J. Bakker, and M. Bonn, "Structure Dynamics of the Proton in Liquid Water Probed with Terahertz Time-Domain Spectroscopy," *Phys. Rev. Lett.*, vol. 102, p. 198303, 2009.

[82] C. Liang and T. L. C. Jansen, "Proton Transport in a Binary Biomimetic Solution Revealed by Molecular Dynamics Simulation," *J. Chem. Phys.*, vol. 135, p. 114502, 2011.

[83] B. L. d. Groot, T. Frigato, V. Helms, and H. Grobmüller, "The Mechanism of Proton Exclusion in the Aquaporin-1 Water Channel," *J. Mol. Bio.*, vol. 333, pp. 279–293, 2003.

[84] E. Tajkhorshid, P. Nollert, M. Ø. Jensen, L. J. W. Miercke, J. O'Connell, R. M. Stroud, and K. Schulten, "Control of the Selectivity of the Aquaporin Water Channel Family by Global Orientation Tuning," *Science*, vol. 296, p. 525, 2002.

[85] R. Pomes and B. Roux, "Structure and Dynamics of a Proton Wire: A Theoretical Study of H+ Translocation Along the Single-File Water Chain in the Gramicidin a Chanel," *Biophys. J.*, vol. 71, pp. 19–39, 1996.

[86] C. Liang, J. Knoester, and T. L. C. Jansen, "Proton Transport in a Membrane Protein Channel: Two-Dimensional Infrared Spectrum Modeling," *J. Phys. Chem. B*, vol. 116, pp. 6336–6345, 2012.

[87] B. C. H. Steele and A. Heinzel, "Materials for Fuel-Cell Technologies," *Nature*, vol. 414, p. 345, 2001.

[88] S. Woutersen, U. Emmerichs, and H. J. Bakker, "Femtosecond Mid-IR Pump-Probe Spectroscopy of Liquid Water: Evidence for a Two-Component Structure," *Science*, vol. 278, no. 5338, pp. 658–660, 1997.

[89] M. Olschewski, S. Knop, J. Lindner, and P. Vöhringer, "From Single Hydrogen Bonds to Extended Hydrogen-Bond Wires: Low-Dimensional Model Systems for Vibrational Spectroscopy of Associated Liquids," *Angew. Chem. Int. Ed.*, vol. 52, pp. 9634–9654, 2013.

[90] A. A. Bakulin, D. Cringus, P. A. Pieniazek, J. L. Skinner, T. L. C. Jansen, and M. S. Pshenichnikov, "Dynamics of Water Confined in Reversed Micelles: Multidimensional Vibrational Spectroscopy Study," *J. Phys. Chem. B*, vol. 117, p. 15545, 2013.

[91] K. Kwac, H. Lee, and M. Cho, "Non-Gaussian Statistics of Amide I Mode Frequency Fluctuations of N-Methylamide in Methanol Solution: Linear and Nonlinear Vibrational Spectra," *J. Chem. Phys.*, vol. 120, p. 1477, 2004.

[92] J. B. Asbury, T. Steinel, K. Kwac, S. A. Corcelli, C. P. Lawrence, J. L. Skinner, and M. D. Fayer, "Dynamics of Water Probed with Vibrational Echo Correlation Spectroscopy," *J. Chem. Phys.*, vol. 121, p. 12431, 2004.

[93] B. M. Auer, R. Kumar, J. R. Schmidt, and J. L. Skinner, "Hydrogen Bonding and Raman, IR, and 2D-IR Spectroscopy of Dilute HOD in Liquid D_2O," *P. Nat. Acad. Sci.*, vol. 104, p. 14215, 2007.

[94] T. L. C. Jansen, B. M. Auer, M. Yang, and J. L. Skinner, "Two-Dimensional Infrared Spectroscopy and Ultrafast Anisotropy Decay of Water," *J. Chem. Phys.*, vol. 132, p. 224503, 2010.

[95] M. L. Cowan, B. D. Bruner, N. Huse, J. R. Dwyer, B. Chugh, E. T. J. Nibbering, T. Elsaesser, and R. J. D. Miller, "Ultrafast Memory Loss and Energy Redistribution in the Hydrogen Bond Network of Liquid H_2O," *Nature*, vol. 434, p. 199, 2005.

[96] A. Paarmann, T. Hayashi, S. Mukamel, and R. J. D. Miller, "Nonlinear Response of Vibrational Excitons: Simulating the 2DIR Spectrum of Liquid Water," *J. Chem. Phys.*, vol. 130, p. 204110, 2009.

[97] R. A. Nicodemus, K. Ramasesha, S. T. Roberts, and A. Tokmakoff, "Hydrogen Bond Rearrangements in Water Probed with Temperature-Dependent 2DIR," *J. Phys. Chem. Lett.*, vol. 1, pp. 1068–1072, 2010.

[98] K. B. Møller, R. Rey, and J. T. Hynes, "Hydrogen Bond Dynamics in Water and Ultrafast Infrared Spectroscopy: A Theoretical Study," *J. Phys. Chem. A*, vol. 108, p. 1275, 2004.

[99] S. Woutersen and H. J. Bakker, "Resonant Intermolecular Transfer of Vibrational Energy in Liquid Water," *Nature*, vol. 402, p. 507, 1999.

[100] M. L. Cowan, B. D. Bruner, N. Huse, D. J. R., B. Chugh, E. T. J. Nibbering, T. Elsaesser, and R. J. D. Miller, "Ultrafast Memory Loss and Energy Redistribution in the Hydrogen Bond Network of Liquid H_2O," *Nat.*, vol. 434, 2005.

[101] D. Kraemer, M. L. Cowan, A. Paarmann, N. Huse, E. T. J. Nibbering, T. Elsaesser, and R. J. D. Miller, "Temperature Dependence of the Two-Dimensional Infrared Spectrum of Liquid H_2O," *P. Nat. Acad. Sci.*, vol. 105, p. 437, 2008.

[102] S. Yeremenko, M. S. Pshenichnikov, and D. A. Wiersma, "Hydrogen-Bond Dynamics in Water Explored by Heterodyne-Detected Photon Echo," *Chem. Phys. Lett.*, vol. 369, p. 107, 2003.

[103] T. L. C. Jansen, T. Hayashi, W. Zhuang, and S. Mukamel, "Stochastic Liouville Equations for Hydrogen-Bonding Fluctuations and Their Signatures in Two-Dimensional Vibrational Spectroscopy of Water," *J. Chem. Phys.*, vol. 123, p. 114504, 2005.

[104] J. B. Asbury, T. Steinel, C. Stromberg, S. A. Corcelli, C. P. Lawrence, J. L. Skinner, and M. D. Fayer, "Water Dynamics: Vibrational Echo Correlation Spectroscopy and Comparison to Molecular Dynamics Simulations," *J. Phys. Chem. A*, vol. 108, no. 7, pp. 1107–1119, 2004. Article.

[105] J. R. Schmidt, S. T. Roberts, J. J. Loparo, A. Tokmakoff, M. D. Fayer, and J. L. Skinner, "Are Water Simulation Models Consistent with Steady-State and Ultrafast Vibrational Spectroscopy Experiments?," *Chem. Phys.*, vol. 341, pp. 143–157, 2007.

[106] S. Knop, T. L. C. Jansen, J. Lindner, and P. Vöhringer, "On the Nature of OH-Stretching Vibrations in Hydrogen-Bonded Chanis: Pump Frequency Dependent Vibrational Lifetime," *Phys. Chem. Chem. Phys*, vol. 13, pp. 4641–4650, 2011.

[107] J. Seehusen, D. Schwazer, J. Lindner, and P. Vöhringer, "Equilibrium and Mid-Infrared Driven Vibrational Dynamics of Artificial Hydrogen-Bonded Networks," *Phys. Chem. Chem. Phys.*, vol. 11, pp. 8484–8495, 2009.

[108] K. Kwac and E. Geva, "A Mixed Quantum-Classical Molecular Dynamics Study of Anti-Tetrol and Syn-Tetrol Dissolved in Liquid Chloroform II: Infrared Emission Spectra, Vibrational Excited-State Lifetimes, and Nonequilibrium Hydrogen-Bond Dynamics," *J. Phys. Chem. B*, vol. 117, pp. 14457–14467, 2013.

[109] I. Paterson and J. P. Scott, "Laboratory emulation of polyketide biosynthesis: An iterative, aldol-based, synthetic entry to polyketide libraries using (r)- and (s)-$_1$-(benzyloxy)-$_2$-methylpentan-$_3$-one, and conformational aspects of extended polypropionates," *J. Chem. Soc. Perkin Trans.*, vol. 1, pp. 1003–1014, 1999.

[110] D. v. d. Spoel, E. Lindahl, A. R. Hess, R. v. Buuren, E. Apol, P. J. Meulenhoff, D. P. Tieleman, A. L. T. M. Sijbers, K. A. Feenstra, R. v. Drunen, and H. J. C. Berendsen, "Gromacs User Manual Version 4.5.6," 2010.

[111] W. L. Jorgensen, J. M. Briggs, and M. L. Contreras, "Relative Partition Coefficients for Organic Solutes from Fluid Simulations," *J. Phys. Chem.*, vol. 94, p. 1683, 1990.

[112] W. L. Jorgensen and J. Tirado-Rives, "The OPLS Potential Functions for Proteins. Energy Minimizations for Crystals of Cyclic Peptides and Crambin," *J. Am. Chem. Soc.*, vol. 110, p. 1657, 1988.

[113] P. T. v. Duijnen and M. Swart, "Molecular and Atomic Polarizabilities: Thole's Model Revisited," *J. Phys. Chem. A*, vol. 102, p. 2399, 1998.

[114] A. A. S. T. Ribeiro, B. A. C. Horta, and R. B. de Alencastro, "MKTOP: A Program for Automatic Construction of Molecular Topologies," *J. Braz. Chem. Soc.*, vol. 19, pp. 1433–1435, 2008.

[115] B. Hess, H. Bekker, H. J. C. Berendsen, and J. G. E. M. Fraaije, "LINCS: A Linear Constraint Solver for Molecular Simulations," *J. Comp. Chem.*, vol. 18, p. 1463, 1997.

[116] S. A. Corcelli, C. P. Lawrence, and J. L. Skinner, "Combined Electronic Structure/molecular Dynamics Approach for Ultrafast Infrared Spectroscopy of Dilute HOD in Liquid H_2O and D_2O," *J. Chem. Phys.*, vol. 120, p. 8107, 2004.

[117] H. Fidder, J. Knoester, and D. A. Wiersma, "Optical-Properties of Disordered Molecular Aggregates - a Numerical Study," *J. Chem. Phys.*, vol. 95, pp. 7880–7890, 1991.

[118] D. J. Thouless, "Electrons in Disordered Systems and the Theory of Localization," *Phys. Rep.*, vol. 13, p. 93, 1974.

[119] J. Lindner, P. Vöhringer, M. S. Pshenichnikov, D. Cringus, D. A. Wiersma, and M. Mostovoy, "Vibrational Relaxation of Pure Water," *Chem. Phys. Lett.*, vol. 421, p. 329, 2006.

[120] U. Essmann, L. Perera, M. L. Berkowitz, T. Darden, H. Lee, and L. G. Pedersen, "A Smooth Particle Mesh Ewald Method," *J. Chem. Phys.*, vol. 103, no. 19, pp. 8577–8593, 1995.

[121] G. McDermott, S. M. Prince, A. Freer, A. M. Hawthornthwaite-Lawless, M. Z. Papiz, R. J. Cogdell, and N. W. Isaacs, "Crystal Structure of an Integral Membrane Light-Harvesting Complex from Photosynthetic Bacteria," *Nature*, vol. 374, pp. 517–521, 1995.

[122] R. J. Cogdell, N. W. Isaacs, A. A. Freer, T. D. Howard, A. T. Gardiner, S. M. Prince, and M. Z. Papiz, "The Structural Basis of Light-Harvesting in Purple Bacteria," *FEBS Lett.*, vol. 555, pp. 35–39, 2003.

[123] J. Koepke, X. Hu, C. Muenke, K. Schulten, and H. Michel, "The Crystal Structure of the Light-Harvesting Complex II (B800-850) from Rhodospirillum Molischianum," *Structure*, vol. 4, pp. 581–597, 1996.

[124] W. Humphrey, A. Dalke, and K. Schulten, "VMD - Visual Molecular Dynamics," *J. Mol. Graphics*, vol. 14, pp. 33–38, 1996.

[125] J.-P. Zhang, R. Fujii, P. Qian, T. Inaba, T. Mizoguchi, and Y. Koyama, "Mechanism of the Carotenoid-To-Bacteriochlorophyll Energy Transfer Via the S1 State in the LH2 Complexes from Purple Bacteria," *J. Phys. Chem. B*, vol. 104, pp. 3683–3691, 2000.

[126] A. M. van Oijen, M. Ketelaars, J. Köhler, T. J. Aartsma, and J. Schmidt, "Unraveling the Electronic Structure of Individual Photosynthetic Pigment-Protein Complexes," *Science*, vol. 285, pp. 400–402, 1999.

[127] M. Ketelaars, A. M. van Oijen, M. Matsushita, J. Köhler, J. Schmidt, and T. J. Aartsma, "Spectroscopy on the B850 Band of Individual Light-Harvesting 2 Complexes of Rhodopseudomonas Acidophila I. Experiments and Monte Carlo Simulations," *Biophys. J.*, vol. 80, pp. 1591–1603, 2001.

[128] S. Oellerich and J. Köhler, "Low-Temperature Single-Molecule Spectroscopy on Photosynthetic Pigment-Protein Complexes from Purple Bacteria," *Photosynth. Res.*, vol. 101, pp. 171–179, 2009.

[129] R. J. Cogdell and J. Köhler, "Use of Single-Molecule Spectroscopy to Tackle Fundamental Problems in BioChemistry: Using Studies on Purple Bacterial Antenna Complexes As an Example," *Biochem. J.*, vol. 422, pp. 193–205, 2009.

[130] R. Kunz, K. Timpmann, J. Southall, R. Cogdell, A. Freiberg, and J. Köhler, "Exciton Self Trapping in Photosynthetic Pigment-Protein Complexes Studied by Single-Molecule Spectroscopy," *J. Phys. Chem. B*, vol. 116, pp. 11017–11023, 2012.

[131] R. Kunz, K. Timpmann, J. Southall, R. Cogdell, A. Freiberg, and J. Köhler, "Fluctuations in the Electron-Phonon Coupling of a Single Chromoprotein," *Angew. Chem. Int. Ed.*, vol. 52, pp. 8726–8730, 2013.

[132] J. D. Hybl, A. W. Albrecht, S. M. Gallagher Faeder, and D. M. Jonas, "Two-Dimensional Electronic Spectroscopy," *Chem. Phys. Lett.*, vol. 297, pp. 307–313, 1998.

[133] A. F. Fidler, V. P. Singh, P. D. Long, and P. D. Dahlberg, "Probing Energy Transfer Events in the Light Harvesting Complex 2 (LH2) of Rhodobacter Sphaeroides with Two-Dimensional Spectroscopy," *J. Chem. Phys.*, vol. 139, p. 155101, 2013.

[134] A. F. Filder, V. P. Singh, P. D. Long, P. D. Dahlberg, and G. S. Engel, "Dynamic Localization of Electronic Excitation in Photosynthetic Complexes Revealed with Chiral Two-Dimensional Spectroscopy," *Nat. Comm.*, vol. 5, p. 3286, 2014.

[135] M. Cho, *Two-Dimensional Optical Spectroscopy*. Boca Raton: CRC Press, 2009.

[136] E. Collini, C. Y. Wong, K. E. Wilk, P. M. G. Curmi, P. Brumer, and G. D. Scholes, "Coherently Wired Light-Harvesting in Photosynthetic Marine Algae at Ambiant Temperature," *Nature*, vol. 463, p. 644, 2010.

[137] G. Panitchayangkoon, D. Hayes, K. A. Fransted, J. R. Caram, E. Harel, J. Z. Wen, R. E. Blankenship, and G. S. Engel, "Long-Lived Quantum Coherence in Photosynthetic Complexes at Physiological Temperature," *P. Nat. Acad. Sci.*, vol. 107, pp. 12766–12770, 2010.

[138] R. Hildner, D. Brinks, J. B. Nieder, R. J. Cogdell, and N. F. van Hulst, "Quantum Coherent Energy Transfer over Varying Pathways in Single Light-Harvesting Complexes," *Science*, vol. 340, pp. 1448–1451, 2013.

[139] O. Rancova, J. Sulskus, and D. Abramavicius, "Insight into the Structure of Photosynthetic LH2 Aggregate from Spectroscopy Simulations," *J. Phys. Chem. B*, vol. 116, pp. 7803–7814, 2012.

[140] L. Cleary and J. Cao, "Optimal Thermal Bath for Robust Excitation Energy Transfer in Disordered Light-Harvesting Complex 2 of Purple Bacteria," *New J. Phys.*, vol. 15, p. 125030, 2013.

[141] G. D. Scholes and G. R. Fleming, "On the Mechanism of Light Harvesting in Photosynthetic Purple Bacteria: B800 to B850 Energy Transfer," *J. Phys. Chem. B*, vol. 104, pp. 1854–1868, 2000.

[142] V. I. Novoderezhkin, R. D., and R. van Grondelle, "Dynamics of the Emission Spectrum of a Single LH2 Complex: Interplay of Slow and Fast Nuclear Motions," *Biophysical J.*, vol. 90, pp. 2890–2902, 2006.

[143] S. Jang, M. D. Newton, and R. J. Silbey, "Multichromophoric Förster Resonance Energy Transfer from B800 to B850 in the Light Harvesting

Complex 2: Evidence for Subtle Energetic Optimization by Purple Bacteria," *J. Phys. Chem. B.*, vol. 111, pp. 6807–6814, 2007.

[144] S. Jang, M. D. Newton, and R. J. Silbey, "Multichromophoric Förster Resonance Energy Transfer," *Phys. Rev. Lett.*, vol. 92, p. 218301, 2004.

[145] H. Sumi, "Theory on Rates of Excitation-Energy Transfer Between Molecular Aggregates Through Distributed Transition Dipoles with Application to the Antenna System in Bacterial Photosynthesis," *J. Phys. Chem. B.*, vol. 103, pp. 252–260, 1999.

[146] B. Bruggemann and V. May, "Exciton Exciton Annihilation Dynamics in Chromophore Complexes. II Intensity Dependent Transient Absorption of the LH2 Antenna System," *J. Chem. Phys.*, vol. 120, no. 2325-2336, 2004.

[147] J. Strümpfer and K. Schulten, "Light Harvesting Complex II B850 Excitation Dynamics," *J. Chem. Phys.*, vol. 131, p. 225101, 2009.

[148] R. van Grondelle and V. I. Novoderezhkin, "Energy Transfer in Photosynthesis: Experimental Insights and Quantitative Models," *Phys. Chem. Chem. Phys*, vol. 8, p. 793, 2006.

[149] V. Novoderezhkin, M. Wendling, and R. van Grondelle, "Intra- and Interband Transfers in the B800-B850 Antenna of *Rhodospirillum Molischianum*: Redfield Theory Modeling of Polarized Pump-Probe Kinetics," *J. Phys. Chem. B*, vol. 107, pp. 11534–11548, 2003.

[150] L. Cleary, H. Chen, C. Chuang, R. J. Silbey, and J. Cao, "Optimal Fold Symmetry of LH2 Rings on a Photosynthetic Membrane," *P. Nat. Acad. Sci.*, vol. 110, pp. 8537–8542, 2013.

[151] O. Rancova and D. Abramavicius, "On the Static and Dynamic Disorder in Bacterial Light-Harvesting Complex LH2: 2DES Simulation Study," *J. Phys. B*, p. DOI: 10.1021/jp5043156, 2014.

[152] J. Adolphs, F. Müh, M. E. Madjet, and T. Renger, "Calculation of Pigment Transition Energies in the FMO Protein," *Photosynth. Res.*, vol. 95, p. 197, 2008.

[153] C. P. van der Vegte, S. Knop, P. Vöhringer, T. L. C. Jansen, and J. Knoester, "OH-Stretching in Synthetic Hydrogen-Bonded Chains," *J. Phys. Chem. B*, vol. 118, pp. 6256–6264, 2014.

[154] T. Pullerits, S. Hess, J. L. Herek, and V. J. Sundström, "Temperature Dependence of Excitation Transfer in LH2 of Rhodobacter Spaeroides," *J. Phys. Chem. B*, vol. 101, pp. 10560–10567, 1997.

[155] A. Damjanović, I. Kosztin, U. Kleinekathöfer, and K. Schulten, "Excitons in a Photosynthetic Light-Harvesting System: A Combined Molecular Dynamics, Quantum Chemistry and Polaron Model Study," *Phys. Rev. E*, vol. 65, p. 031919, 2002.

[156] M. Steffen, K. Lao, and S. Boxer, "Dielectric Asymmetry in the Photosynthetic Reaction Center," *Science*, vol. 264, pp. 810–816, 1994.

[157] T. Renger, "Theory of Excitation Energy Transfer: From Structure to Function," *Photosynth. Res.*, vol. 102, pp. 471–485, 2009.

[158] T. Renger and F. Müh, "Theory of Excitonic Couplings in Dielectric Media : Foundation of Poisson-TrEsp Method and Application to Photosystem I Trimers," *Photosynth. Res.*, vol. 111, pp. 47–52, 2012.

[159] C. P. Hsu, G. R. Fleming, M. Head-Gordon, and T. Head-Gorden, "Excitation Energy Transfer in Condensed Media," *J. Chem. Phys.*, vol. 114, pp. 3065–3072, 2011.

[160] C. Olbrich, J. Strümpfer, K. Schulten, and U. Kleinekathöfer, "Theory and Simulation of the Environmental Effects on FMO Electronic Transitionsnvironmental Effects on FMO Electronic Transitions," *J. Phys. Chem. Lett.*, vol. 2, pp. 1771–1774, 2011.

[161] A. D. MacKerell, D. Bashford, M. Bellott, R. L. Dunbrack, J. D. Evanseck, M. J. Field, S. Fischer, J. Gao, H. Guo, S. Ha, D. Joseph-McCarthy, L. Kuchnir, K. Kuczera, F. T. K. Lau, C. Mattos, S. Michnick, T. Ngo, D. T. Nguyen, B. Prodhom, W. E. Teiher, B. Roux, M. Schlenkrich, J. C. Smith, R. Stote, J. Straub, M. Watanabe, J. Wiórkiewicz-Kuczera, D. Yin, and M. Karplus, "All-Atom Empirical Potential for Molecular Modeling and Dynamics Studies of Proteins," *J. Phys. Chem. B*, vol. 102, pp. 3586–3616, 1998.

[162] N. Foloppe and A. D. MacKerell, "All-Atom Empirical Force Field for Nucleic Acids: I. Parameter Optimization Based on Small Molecule and Condensed Phase Macromolecular Target Data," *J. Comput. Chem.*, vol. 21, pp. 86–104, 200.

[163] W. L. Jorgensen, J. Chandrasekhar, J. D. Madura, R. W. Impey, and M. L. Klein, "Comparison of Simple Potential Functions for Simulating Liquid Water," *J. Chem. Phys.*, vol. 79, p. 926, 1983.

[164] G. Bussi, D. Donadio, and M. Parrinello, "Canonical Sampling Through Velocity Rescaling," *J. Chem. Phys.*, vol. 126, p. 014101, 2007.

[165] W. C. Swope, H. C. Andersen, P. H. Berens, and K. R. Wilson, "A Computer Simulation Method for the Calculation of Equilibrium Constants for the Formation of Physical Clusters of Molecules: Application to Small Water Clusters," *J. Chem. Phys.*, vol. 76, p. 637, 1982.

[166] R. M. Hochstrasser, "Two-Dimensional IR-Spectroscopy: Polarization Anisotropy Effects," *Chem. Phys.*, vol. 266, no. 2-3, pp. 273–284, 2001.

[167] M. Z. Papiz, S. M. Prince, T. Howard, R. J. Cogdell, and N. W. Isaacs, "The Structure and Thermal Motion of the B800-850 LH2 Complex from Rps.acidophila at 2.0a Resolution and 100K: New Structural Features and Functionally Relevant Motions," *J. Mol. Biol.*, vol. 326, pp. 1523–1538, 2003.

[168] M. H. C. Koolhaas, G. van der Zwan, R. N. Frese, and R. van Grondelle, "Red Shift of the Zero Crossing in the CD Spectra of the LH2 Antenna Complex of Rhodopseudomonas Acidophila: A Structure-Based Study," *J. Phys. Chem. B*, vol. 101, pp. 7262–7270, 1997.

[169] V. Lioulia, L. Valkunas, and R. van Grondelle, "Excitons in Chains of Dimers," *J. Phys. Chem. B*, vol. 101, pp. 7343–7349, 1997.

[170] R. Kunz, K. Timpmann, J. Southall, R. J. Cogdell, A. Freiberg, and J. Köhler, "Single-Molecule Spectroscopy Unmasks the Lowest Exciton State of B850 Assembly in LH2 from Rps. Acidophila," *Biophys. J.*, vol. 106, pp. 2008–2016, 2014.

[171] M. Dahlbom, T. Pullerits, S. Mukamel, and V. Sundström, "Exciton Delocalization in the B850 Light-Harvesting Complex: Comparison of Different Measures," *J. Phys. Chem. B*, vol. 105, pp. 5515–5524, 2001.

[172] J. M. Moix, Z. Yang, and J. Cao, "Equilibrium-Reduced Density Matrix Formulations: Influence of Noice, Disorder, and Temperature on Localization in Excitonic Systems," *Phys. Rev. B*, vol. 85, p. 115412, 2012.

[173] W. M. Zhang, T. Meier, V. Chernyak, and S. Mukamel, "Exciton-Migration and Three-Pulse Femtosecond Optical Spectroscopy of Photosynthetic Antenna Complexes," *J. Chem. Phys.*, vol. 108, pp. 7763–7774, 1998.

[174] T. Meier, V. Chernyak, and S. Mukamel, "Femtosecond Photon Echoes in Molecular Aggregates," *J. Chem. Phys.*, vol. 107, pp. 8759–8774, 1997.

[175] M. Mostovoy and J. Knoester, "Statistics of Optical Spectra from Single-Ring Aggregates and Its Application to LH2," *J. Phys. Chem. B*, vol. 104, pp. 12355–12364, 2000.

[176] M. H. C. Koolhaas, R. N. Frese, G. J. S. Fowler, T. S. Bibby, S. Georgakopoulou, G. van der Zwan, C. N. Hunter, and R. van Grondelle, "Identification of the Upper Exciton Component of the B850 Bacteriochlorophylls of the LH2 Antenna Complex, Using a B800-Free Mutant of Rhodobacter Sphaeroides," *Biochem.*, vol. 37, pp. 4693–4698, 1998.

[177] S. Georgakopoulou, R. N. Frese, E. Johnson, C. Koolhaas, R. J. Cogdell, R. van Grondelle, and G. van der Zwan, "Absorption and CD Spectroscopy and Modeling of Various LH2 Complexes from Purple Bacteria," *Biophys. J.*, vol. 82, pp. 2184–2197, 2002.

[178] M. Matsushita, M. Ketelaars, A. M. van Oijen, J. Köhler, T. J. Aartsma, and J. Schmidt, "Spectrosopy on the B850 Band of Individual Light-Harvesting 2 Complexes of Rhodopsudomonas Acidophila II. Exciton States of an Elliptically Deformed Ring Aggregate," *Biophys. J.*, vol. 80, pp. 1604–1614, 2001.

[179] P. Heřman, D. Zapletal, and P. Kabrhel, *Simulation of Emission Spectra for LH2 Ring: Fluctuations in Radial Positions of Molecules.* Saint Petersburg State Polytechnic University, 2014.

[180] L. D. Bakalis and J. Knoester, "Pump-Probe Spectroscopy and the Exciton Delocalization Length in Molecular Aggregates," *J. Phys. Chem. B*, vol. 103, no. 31, pp. 6620–6628, 1999.

[181] A. Freiberg, M. Rätsep, K. Timpmann, G. Trinkunas, and N. W. Woodbury, "Self-Trapped Excitons in LH2 Antenna Complexes Between 5K and Ambiant Temperature," *J. Phys. Chem. B*, vol. 107, pp. 11510–11519, 2003.

[182] M. Pajusalu, M. Rätsep, G. Trinkunas, and A. Freiberg, "Davydov Splitting of Excitons in Cyclic Bacteriochlorophyll a Nanoaggregates of Bacterial Light-Harvesting Complexes Between 4.5 and 263 K," *ChemPhysChem*, vol. 12, pp. 634–644, 2011.

[183] A. Gelzinis, D. Abramavicius, and L. Valkunas, "Non-Markovian Effects in Time-Resolved Fluorescense Spectrum of Molecular Aggregates: Tracing Polaron Transformation," *Phys. Rev. B*, vol. 84, p. 245430, 2011.

[184] S. Hess, F. Feldchtein, A. Babin, I. Nurgaleev, T. Pullerits, A. Sergeev, and V. Sundstrom, "Femtosecond Energy Transfer Within the LH2 Peripheral Antenna of the Photosynthetic Purple Bacteria *Rhodobacter Spaeroides* and *Rhodopseudomonas Palustris LL*," *Chem. Phys. Lett.*, vol. 216, pp. 247–257, 1993.

[185] A. P. Schreve, J. K. Trautman, H. A. Frank, T. G. Owens, and A. C. Albrecht, "Femtosecond Energy-Transfer Processes in the B800-850 Light-Harvesting Complex of Rhodobacter Sphaeroides 2.4.1," *Biochem. Biophys. Acta.*, vol. 1058, p. 280, 1991.

Samenvatting

Het bestuderen van dynamische processen zoals structuurveranderingen van bijvoorbeeld vloeistoffen of proteïnen en energietransport in een zonnecel of fotosynthetisch systeem is zeer uitdagend. Voor een goed microscopisch begrip is het namelijk nodig zulke processen te volgen op een sub-picoseconde (één miljoenste van één miljoenste seconde) tijdschaal. Door gebruik te maken van geavanceerde moderne lasertechnieken is het mogelijk dynamica op deze extreem korte tijdschalen te ontrafelen. Zulke experimenten zijn echter lastig te interpreteren en een vergelijking met theoretische berekeningen is daarom onmisbaar. In dit proefschrift ontwikkelen we zulke theoretische middelen en passen deze toe op verschillende systemen.

Een goed voorbeeld van een dynamische proces dat intens bestudeerd wordt is energietransport in fotosynthetische systemen. In fotosynthetische systemen van bijvoorbeeld planten en bacteriën wordt er zonlicht omgezet in chemische energie. Bij dit proces wordt er eerst een lichtdeeltje, genaamd een foton, geabsorbeerd door de pigmenten. De absorptie van het foton zorgt ervoor dat het pigment zich in een hogere (aangeslagen) energietoestand bevindt. Deze energie wordt daarnaar getransporteerd naar één van de zogeheten reactiecentra. Hier wordt de energie gebruikt voor de productie van koolhydraten die bruikbaar zijn als bouwstenen voor andere organische verbindingen of als brandstof voor biologische processen in het fotosynthetische systeem. Door miljoenen jaren lange evolutie zijn de fotosynthetische systemen in de natuur ontzettend efficiënt. Een voorbeeld bij uitstek zijn de systemen van groene en paarse zwavel bacteriën die zelfs op plekken waar weinig licht beschikbaar is, zoals diep in de zee, weten te overleven. Het fotosynthetische systeem van paarse bacteriën is schematisch afgebeeld in Figuur 1. In deze bacteriën is het energietransport naar de reactiecentra ontzettend efficient. Namelijk, meer dan 90% van de geabsorbeerde

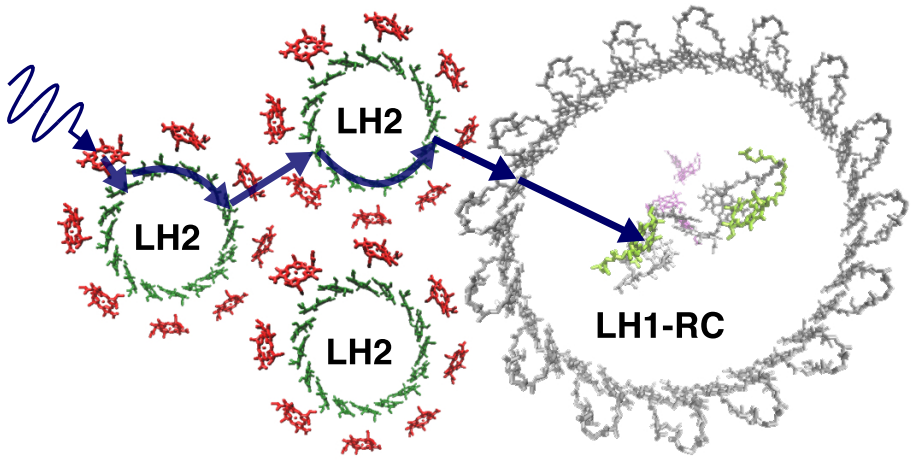

Figuur 1: Schematisch overzicht van het fotosynthetische systeem van paarse bacteriën. Licht wordt geabsorbeerd door een pigment in het *Light Harvesting 2* (LH2) complex waarnaar de resulterende excitatie getransporteerd wordt door het fotosynthetische systeem totdat het een *Light Harvesting 1 - Reactiecentrum* (LH1-RC) complex bereikt. Hier wordt de energie gebruikt voor de productie van koolhydraten.

fotonen bereikt één van de reactiecentra. Het begrijpen van zulke efficiënte biologische systemen zou kunnen leiden tot de verdere ontwikkeling van zonnecellen en energietransport systemen.

Experimenteel gezien kan de absorptie bestudeerd worden door te meten hoe sterk het systeem de verschillende frequenties (kleuren) van het licht absorbeert. De gemeten absorptiespectra hangen af van de structuur die de pigmenten vormen alsmede van de interactie met hun lokale omgeving. Als pigmenten dicht bij elkaar zitten treedt er een wisselwerking (koppeling) tussen hen op die verantwoordelijk is voor het energie transport van het ene pigment naar het andere. De sterkte van de wisselwerking hangt onder andere af van de afstand tussen de pigmenten, hun relatieve oriëntatie en van hun omgeving. De optische eigenschappen van gekoppelde pigmenten zijn zeer verschillend van die van individuele pigmenten. In het geval van paarse bacteriën, bijvoorbeeld, vormen de pig-

menten ringvormige structuren, die ook wel aggregaten worden genoemd (Figuur 1). Door de wisselwerking tussen de pigmenten kan het absorptiespectrum van het aggregaat verschoven zijn naar een lagere frequentie (J-aggregaat) of hogere frequentie (H-aggregaat) ten opzichte van dat van de individuele pigmenten. In het geval van het Light Harvesting systeem 2 (Figuur 1), bijvoorbeeld, is het spectrum door de wisselwerking tussen de pigmenten verschoven naar een lagere frequentie en zijn de pieken in het spectrum smaller. Deze specifieke optische eigenschappen komen tot stand doordat de wisselwerking leidt tot zogeheten gedelokaliseerde toestanden. Dit is kwantummechanisch effect en betekent dat de aangeslagen toestand, die resulteert van de absorptie van het licht, collectief gedeeld wordt door meerdere pigmenten. Het is dus niet één enkel pigment dat het foton absorbeert maar meerdere pigmenten samen. De absorptie spectra worden ook sterk beïnvloed door de interactie van de pigmenten met hun directe omgeving, bestaande uit bijvoorbeeld proteïnen, membranen en water. De aanwezigheid van de omgeving beïnvloedt namelijk de frequentie waarbij de pigmenten absorberen. In LH2 bijvoorbeeld, zijn de pigmenten in de binnenste ring chemisch hetzelfde als de chromoforen in de buitenring, maar hun absorptiefrequenties zijn zeer verschillend door hun verschillende omgevingen. Ondanks de invloed van de structuur en wisselwerking op de absorptiespectra is het niet mogelijk structuurveranderingen en energietransport te volgen met deze techniek. Het is namelijk lastig onderscheidt te maken tussen effecten die komen door de wisselwerking tussen de pigmenten en die resulteren van de interactie met de omgeving, omdat beiden de absorptiefrequenties beïnvloeden. Daarnaast worden de absorptiespectra vaak gemeten op monsters met miljoenen moleculen, zodat het spectrum een gemiddelde weerspiegelt van al deze moleculen. Dit maakt het moeilijk te begrijpen wat er zich lokaal afspeelt.

Twee-dimensionale spectroscopie is een techniek die dynamische processen zoals energietransport en structuurveranderingen wel kan volgen met een subpicoseconde (10^{-12} seconde) tijdsresolutie. Bij deze experimenten wordt het systeem met meerder korte laserpulsen beschoten waarbij de tijd tussen de pulsen gevarïeerd wordt. In principe werken zulke experimenten als volgt: Eerst wordt het systeem beschoten met licht dat geabsorbeerd wordt. Na een wachttijd die gevarieerd kan worden en korter kan zijn dan een enkele picoseconde wordt er met een andere lichtpuls gemeten wat er met de energie, die eerder geabsorbeerd werd, gebeurd is. Door de wachttijd te variëren kunnen dynamische processen zoals structuurveranderingen en energietransport nauwkeurig gevolgd worden.

Een veel bestudeerd voorbeeld van een systeem waarbij gekeken wordt naar veranderingen van structuur is water. In water vormen verschillende watermoleculen waterstofbindingen met elkaar en deze waterstofbindingen breken en vormen zich op een extreem korte tijdschaal. Een goed begrip van zulke dynamica is belangrijk, omdat water in veel experimenten gebruikt wordt als oplosmiddel. Daarnaast speelt water in het menselijk lichaam een essentiële rol bij het vouwen van proteïnen in complexe drie-dimensionale structuren. Deze vouwprocessen zijn niet goed begrepen en bepalen de uiteindelijke functie van de proteïnen. Met gebruik van infrarood licht kan de dynamica van water bestudeerd worden. Met infrarood licht kan namelijk een OH-binding van een water molecuul (H_2O) in trilling worden gebracht. De frequentie van deze trilling, en daarmee de frequentie van het geabsorbeerde licht, hangt sterk af van de omgeving van de OH-binding en dus of zij een waterstofbinding vormt met een zuurstofatoom van een ander watermolecuul of niet. Als tijdens de wachttijd een waterstofbinding breekt of gevormd wordt, zal de frequentie van het licht dat gemeten wordt anders zijn dan de frequentie die initieel geabsorbeerd werd. Door deze verschillen in frequenties te meten als functie van de wachttijd kan het veranderen van de structuur en het breken en vormen van waterstofbindingen dus gevolgd worden.

Bij deze experimenten is het belangrijk te beseffen dat de dynamica tijdens de wachttijd anders kan zijn dan de dynamica die zou plaats hebben gevonden als het systeem niet eerst met licht was beschoten. Namelijk, doordat de OH-binding aan het trillen is gebracht kan het zijn dat de omgeving zich reorganiseert. Deze reorganisatie van de omgeving kan wederom leiden tot een verandering in de frequentie van de OH-trilling en wordt een Stokes shift genoemd.

De wisselwerking en het energietransport tussen pigmenten kan op een vergelijkbare manier worden bestudeerd als structuurveranderingen. Dit is succesvol toegepast op onder andere de fotosystemen van groene en paarse bacteriën. In het geval van fotosynthetische systemen wordt zichtbaar licht gebruikt dat door de pigmenten wordt geabsorbeerd. De pigmenten absorberen bij verschillende frequenties door hun verschillen in omgeving. Als er tijdens de wachttijd energietransport plaatsvindt van het ene pigment naar het andere, zal de frequentie waarbij initieel geabsorbeerd is anders zijn dan die gemeten wordt. Door de wachttijd te variëren en te scannen over de frequenties waarbij het systeem absorbeert en waarbij de aangeslagen toestand gemeten wordt, kan er nauwkeurig bepaald worden hoe het energietransport binnen het systeem plaatsvindt en

welke pigmenten een wisselwerking met elkaar hebben. Omdat de sterkte van de wisselwerking tussen pigmenten afhangt van de afstand tussen de pigmenten en hun relatieve oriëntatie, bevatten twee-dimensionale spectra ook informatie over de structuur van het systeem. Dit wordt onder andere gebruikt voor de bepaling van proteïnestructuren.

De gemeten twee-dimensionale spectra zijn vaak lastig te interpreteren, omdat het niet duidelijk is welke pigmenten bij welke frequenties horen. Daarnaast is het lastig om onderscheid te maken tussen effecten die voortkomen uit de wisselwerking tussen de pigmenten en die uit de interactie tussen de pigmenten en hun omgeving. Daarom zijn theoretische berekeningen en modellen nodig die een algemene beschrijving bevatten van de wisselwerking tussen de pigmenten en de interactie met hun omgeving. In dit proefschrift worden zulke theoretische middelen voor het berekenen van twee-dimensionale spectra ontwikkeld die zowel op vibrationele systemen (infrarood licht) als elektronische systemen (zichtbaar licht) toegepast kunnen worden. Binnen deze modellen beschrijven we de pigmenten met gebruik van de kwantummechanica, wat belangrijk is om de absorptie en het energietransport goed te modelleren. De pigmenten worden omringd door duizenden moleculen in de omgeving die allemaal een invloed hebben op de absorptiefrequenties en wisselwerking tussen pigmenten. Het is niet haalbaar al deze vrijheidsgraden kwantummechanisch te beschrijven en daarom worden deze klassiek behandeld. Omdat de systeemomgeving en de pigmenten elkaar beïnvloeden, is het belangrijk het kwantum en klassieke systeem aan elkaar te koppelen. Vaak wordt de invloed van de excitatie van het kwantumsysteem op de omgeving, die belangrijk is voor de Stokes shift, genegeerd in theoretische modellen, omdat het onduidelijk is hoe deze mee te nemen. In hoofdstuk 2 ontwikkelen we twee methoden (Ehrenfest en surface hopping) voor het berekenen van twee-dimensionale spectra waarbij deze interactie meegenomen wordt. We testen de methoden op modelsystemen waarvoor het exacte antwoord bekend is. We laten zien dat we door de invloed van de excitatie van de pigmenten op de omgeving mee te nemen, de Stokes shift kunnen beschrijven en dat deze interactie essentieel is voor een correcte beschrijving van het energietransport. Met name de surface hopping methode benadert het exacte resultaat uitstekend.

In hoofdstuk 3 passen we de ontwikkelde surface hopping methode toe voor het bestuderen van de dynamica van waterstofbindingen. We bekijken twee synthetische moleculen waarin OH-groepen één-dimensionale waterstof gebonden ketens vormen en interpreteren de experimentele spectra waarbij gekeken

wordt naar de OH-trillingen. We bekijken het *all-syn* molecuul waar waterstofbindingen sterk zijn en nauwelijks breken en het *all-anti* molecuul waar waterstofbindingen zwak zijn en frequent breken en vormen. Door de verschillen in de spectra voor beide moleculen te begrijpen kan de invloed van de sterkte van waterstofbindingen op de spectra bepaald worden. De synthetische moleculen worden in het experiment omringd door een chloroformoplossing. We beschrijven deze omgeving met gebruik van moleculaire dynamica simulaties waarbij ieder atoom apart beschreven wordt en zo de invloed van de omgeving op de absorptiefrequenties van de OH-trillingen zeer nauwkeurig bepaald kan worden. In de absorptiespectra is voor de *all-syn* vooral één piek te zien die correspondeert met de frequentie van waterstofgebonden OH-trillingen. Bij het *all-anti* molecuul zijn er twee pieken; één die correspondeert met de waterstofgebonden OH-trillingen en één met die van de vrije OH-trillingen. Uit de twee-dimensionale spectra leiden we af dat een sterke waterstofbinding leidt tot het sneller fluctueren van de absorptiefrequenties van de OH-trillingen dan voor een zwakke waterstofbinding. Daarnaast zorgt een sterke waterstofbinding voor een sterke wisselwerking tussen de verschillende OH-trillingen, wat er toe leidt dat de energie snel verspreid raakt over het molecuul voor het *all-syn* molecuul. Voor de *all-anti* variant is het energietransport langzamer door de zwakke wisselwerking ten gevolge van de zwakke waterstofbinding. Dit verklaart de experimenteel waargenomen afhankelijkheid van de initiële absorptiefrequentie op de vibrationele levensduur van de excitatie.

In hoofdstuk 4 gebruiken we de surface hopping methode voor het bestuderen van energietransport in het LH2 complex dat een belangrijk element is van het fotosynthetische systeem van paarse bacteriën (Figuur 1). De omgeving van de pigmenten bestaande uit proteïnen, een membraan en water wordt hier wederom volledig atomistisch beschreven met behulp van moleculaire dynamica en de simulaties bevatten in totaal meer dan 114.000 atomen. Hierdoor is het mogelijk nauwkeurig de invloed van de omgeving op de absorptiefrequenties van de pigmenten te bepalen. Het absorptiespectrum van LH2 bestaat uit twee pieken en we onthullen de elektronische structuur die hiervoor verantwoordelijk is. De lage-energie piek in het absorptiespectrum komt voornamelijk van de absorptie van pigmenten in de binnenring terwijl zowel pigmenten in de binnenring als de buitenring bijdragen aan de hoge-energie piek. Het energietransport binnen het LH2 complex van de buitenring (hoge energie) naar de binnenring (lage energie) vindt plaats in een indrukwekkende 0.7 pico-seconde. Dit transport kan zo snel

plaatsvinden door een kwantummechanisch effect. Er bevinden zich namelijk energietoestanden die gedelokaliseerd zijn over pigmenten in zowel de binnen- als buitenring. Dit zorgt ervoor dat de energie stap voor stap van pigmenten in de buitenring naar die in de binnenring wordt getransporteerd.

Samenvattend hebben wij nieuwe methoden ontwikkeld voor het berekenen van twee-dimensionale spectra, waarmee structuurveranderingen en energietransport in complexe systemen bestudeerd kunnen worden. De interactie tussen de pigmenten en omgeving kan beschreven worden op een volledig atomistische manier, wat veel informatie verschaft over de invloed van de omgeving op de pigmenten en vice versa. In de toekomst kan de methode mogelijke toegepast worden voor het beschrijven van structuurveranderingen van proteïnen, moleculaire motoren en energietransport in fotosynthetische complexen en zonnecellen.

Acknowledgments

Firstly, I would like to acknowledge my promotor Jasper Knoester. Jasper, it has been my privilege to work with you for the past four years. In spite of your busy schedule, you always provided me with feedback and new insights during our enjoyable Friday morning meetings. Moreover, I am grateful for your numerous corrections to our papers and this thesis.

This thesis would not have been the same without the help of my co-promotor and daily supervisor Thomas la Cour Jansen. Thomas, I enjoyed our collaboration very much. Your door was always open for discussions on scientific matters and conversations on a more personal level. Your critical look and never ending novel ideas continuously contributed to the research.

I am also grateful to the members of the assessment committee, Jürgen Köhler, Sander Woutersen and Siewert-Jan Marrink for their valuable time spend on reading this thesis.

My stay during the past four years has been a joyful experience due the pleasant environment at the corridor and interactions with my colleagues. Thanks especially to my excellent office mates Roel Tempelaar, Wout Merbis and Arunesh Roy. The ever lasting humour in our office always brightened my days. I also joyfully remember the many interactions with Roel and Jasper Compaijen on a professional level as well as on a personal level. Thank you guys for introducing me to coffee! Without it, my thesis would not have been the same. I am also grateful to the other members of the Theory of Condensed Matter group including Erik Bloemsma, Andrea Scaramucci, Anna Stradomska-Szymczak, Frank Haverkort, Victor Malyshev, Dennis Visser, Andrey Leonov, Chungwen Liang, Roel Tempelaar, Ana Cunha, Anna Bondarenko, Maxim Mostovoy, Jasper Compaijen, Santanu Roy, Sergey Artyukhin, Bas Vlaming, Alessio Pozzi, Olexander Shvets, Bintoro Nugroho, Marwa Farag, Maria Azhar and Bernhard Hoenders. I enjoyed our scientific discussions, lunches, dinners and other activities.

The past four years also have been an enriching period on a personal level. In the beginning of my PhD studies I met my wonderful girlfriend. Mengying, Nǐ shì wǒ yīshēng de zhì ài. Your love and support makes me extremely happy. I joyfully look back at our numerous trips back and forth to China and the Netherlands, and am very grateful that you moved to the Netherlands for me. I also thank my parents. Your everlasting love and support have encouraged me in many different ways. For the same reasons I am grateful to my two older brothers. Chiel and Marc, I could not imagine anyone else being my paranymphs.